



**University of Naples  
Federico II**

*Department of Civil, Architectural and Environmental Engineering*

Ph.D. Programme in Civil Systems Engineering

XXXIV Cycle

Naples, Italy

# **Experimental and Numerical Investigation to couple a Piano Key Weir with a Fish Pass**

**Guadalupe Torre Gómez**

**Supervisors**

Prof. Eng. Maurizio Giugni

Dr. Eng. Francesco Pugliese

**Ph.D. Programme  
Coordinator**

Prof. Eng. Andrea Papola

**2022**







---

## ABSTRACT

---

Climate Change has led to a higher risk of flooding events and droughts directly affecting the environment and the society. These changes have brought to develop Piano Key Weirs (PKWs), which are characterized by a higher discharge efficiency. The location of PKWs in rivers allows increasing the water level for numerous purposes, such as hydropower exploitation or irrigation, while controlling the upstream water level during flooding events, which ultimately helps to avoid the overtopping of the banks. Nevertheless, the installation of hydraulic structures, such as PKWs, on rivers results in altered habitats, modified flow conditions, loss of river continuity and connectivity and especially severe damaging impacts on the aquatic environment. One of the effective solutions to overcome some of these problems is installing fish passes. The aim of this Ph.D. research is studying the viability of combining a PKW with a fishway, proposing a new structure which joins the beneficial effects of the PKW discharge efficiency with the possibility of creating a passage for fishes, aiming at overcoming the barrier created by the PKW structure on the river.

Aiming to better understand the discharge efficiency of the two most efficient PKW types, type A and type B, an experimental and numerical assessment was performed to evaluate the discharge efficiency of three PKW geometries: a symmetric type A,  $PKW_A$ , with  $W_i/W_o=1.5$ , the same model rotated  $180^\circ$ , resulting in a type A  $W_i/W_o=0.67$ ,  $PKW_{A\_reverse}$ , and a type B model,  $PKW_B$ , with the main geometric features than  $PKW_A$  ( $L, P, W_i, W_o, Bb, Bh$ ). The  $PKW_A$  and the  $PKW_{A\_reverse}$  were experimentally and numerically tested while the  $PKW_B$  was only studied

---

numerically. The comparison between numerical and experimental results proved the effectiveness of using numerical testing. The obtained results showed that the  $PKW_A$  discharge coefficient is up to  $\sim 34\%$  higher than the  $PKW_{A\_reverse}$ , resulting in an increase of the upstream head on the  $PKW_{A\_reverse}$  up to  $\sim 32\%$ , remarking the relevance of the  $W_i/W_o$  ratio in the discharge efficiency of PKWs. Conversely, the tested  $PKW_B$  resulted more efficient for lower head ( $H/P \lesssim 0.35$ ) than the  $PKW_A$ , however, when increasing the upstream head, the  $PKW_A$  model proved to be more efficient. This change in efficiency is herein explained because of the hydraulic behaviour of the inlet and outlet key of both geometries. Results proved that the discharge coefficient is strongly dependant on the specific geometry, hence, it is not possible to generalize about the efficiency of the different PKW types.

Furthermore, a Denil fish pass was selected to be implemented in the outlet key of the tested  $PKW_B$ , which was modified to foster the fish pass. A numerical assessment of the combined structure was performed aiming to verify the advisable flow conditions for fish passage and to evaluate the loss in efficiency of the  $PKW_{B-FP}$  in comparison with the  $PKW_B$ . After following the geometry design recommendations from the FAO (Food and Agriculture Organization of the United Nations, 2002) for the fish pass, numerical results showed that the velocity field obtained in the middle of the fish pass and in the baffles exceeded the maximum advisable velocity of  $2 \text{ m s}^{-1}$ . In terms of discharge efficiency, the  $PKW_{B-FP}$  discharge coefficient is up to  $\sim 42.4\%$  smaller than the  $PKW_B$ , resulting in an increase of the upstream head up to  $\sim 51.8\%$ .

This assessment proved the possibility of effectively combine a fish pass with a PKW, resulting in a new structure that works as a fish pass at regular conditions and as a PKW at flood conditions. The two main advantage of installing this structure in rivers are: (1) to restore continuity for fish movements and (2) either to increase the upstream water level in rivers, while maintaining inundation risks comparable to the previous ones or to decrease upstream inundation risk if the weir crest level is maintained constant.

**Keywords:** Piano Key Weir, Denil Fish Pass, discharge efficiency, CFD model, hydraulic behaviour.

## **ACKNOWLEDGMENTS**

---

This Ph.D. course has brought me so much personal and intellectual growth, and this experience wouldn't have been the same without the guidance and assistance of many people.

First of all, I would like to thank my Tutor, Prof. Maurizio Giugni, for trusting me since the very first moment of this adventure. His knowledge and support have been fundamental during these years. Likewise, I would like to express my gratitude towards the PhD Coordinator, Prof. Andrea Papola for his availability and unquestionable help.

I direct special thanks to Prof. Sébastien Erpicum, from University of Liège, who supported me with his great expertise and kindness.

This experience wouldn't have been the same without the friendship of my colleagues from the DICEA department. In particular, to my dear friends Maria Cristina Morani, Roberta Ferraiuolo, Andrea D'Aniello, Diana Fiorillo, Gerardo Caroppi, Giuseppe Ascione and Andrea del Gaudio. Furthermore, my gratitude goes towards Mimmo and Tonino, who helped me built the laboratory setup at the DICEA.

I can't also forget the support from my professors and colleagues from the University of Oviedo, who have shared my journey for so many years. Special thanks to Prof. Eduardo Álvarez, who have also helped me with his fruitful comments and suggestions regarding my PhD thesis, and Prof. Joaquín Fernández. Both believed in me years ago and invited me to be part of their research team. Likewise, I express my most sincere gratitude to all my friends from university, in special to Aitor

---

Fernández Jiménez, who have been a professional inspiration and a true friend to me.

The PhD experience is another important chapter in life that I have the pleasure to share with my closest friends Vanessa, Beatriz, María and Verónica. Special greetings to my dearest friend Aida, who is like a sister to me, who have supported me every single day of this journey. I have no words to describe how much you mean to me and how thankful I am for having you in my life.

I would also like to deeply thank my family, my aunts Pilar, Luisa and Nieves and my grandmother Pilar, who have been fundamental in my life. To my brother, my sister-in-law, and my incredible niece Olaia, who I hope can achieve anything she wonders in life.

Nonetheless, I wouldn't have been able to success without the incredible and unconditional support of Dr. Francesco Pugliese. You have been my mentor, my inspiration, my friend and my family during these 3+ years. You are the best gift of this experience, and I will be eternally grateful for everything you have done for me.

And finally, this PhD thesis is dedicated to my rock, my role model and my strength. Thank you Mom for helping me to be the woman that I am today. I will always try to make you proud.

## TABLE OF CONTENTS

ABSTRACT.....	I
ACKNOWLEDGMENTS .....	IV
TABLE OF CONTENTS .....	VI
LIST OF FIGURES .....	IX
LIST OF TABLES.....	XIII
LIST OF SYMBOLS .....	XVI
LIST OF ABBREVIATIONS.....	XIX
Chapter 1: Introduction.....	1
1.1 Problem Statement.....	3
1.2 Research Objectives.....	5
1.3 Outline of the Thesis.....	6
References.....	8
Chapter 2:Piano Key Weir (PKW) Research.....	11
2.1 Weirs and spillways.....	11
2.1.1 Sharp-crest weirs .....	11
2.1.2 Side weirs.....	12
2.1.3 Labyrinth weirs .....	13
2.2 Piano Key Weirs .....	14
2.2.1 PKW geometry.....	15
2.2.2 PKW optimal design.....	20
2.2.3 Analytical equations to predict discharge coefficients of PKWs.....	22
2.2.3.1 Leite Ribeiro et al. equation .....	23
2.2.3.2 Kabiri-Samani and Javaheri equation .....	25
2.2.3.3 Machiels et al. equation.....	25
2.2.3.4 Hu et al. equation.....	27
2.2.3.5 Guo et al. equation.....	29
2.2.4 PKW velocity, surface profile and nappe behaviour .....	29
2.2.5 PKW in rivers .....	30
2.2.6 Scale effects in PKW physical models .....	31
2.2.7 PKW numerical modelling.....	33
References.....	35
Chapter 3: Fish Passes.....	41

---

3.1	Hydraulic requirements for fish passes .....	43
3.1.1	Fish pass entrance and attraction flow .....	43
3.1.2	Discharge and current conditions in the fish pass .....	44
3.1.3	Fish pass exit conditions .....	45
3.1.4	Optimal location of the fish pass on the river.....	45
3.2	Technical fish passes .....	46
3.2.1	Pool passes.....	46
3.2.2	Vertical Slot Pass .....	47
3.2.3	Denil pass .....	48
3.2.3.1	Denil pass overview .....	48
3.2.3.2	Denil pass geometric characteristics .....	50
3.2.3.3	Discharge through a Denil pass.....	52
	References.....	55
	Chapter 4: Experimental Investigations of type A PKWs .....	58
4.1	Laboratory set-up.....	60
4.2	Uncertainty Analysis of Experimental Measurements.....	65
4.3	Experimental Characterization of the Discharge Coefficient .....	67
4.4	Experimental Characterization of the Velocity Field in the Inlet Key.....	68
	References.....	69
	Chapter 5: CFD Modelling of type A and type B PKWs .....	70
5.1	3D Model .....	72
5.2	Boundary Conditions and Simulation Properties of the CFD Model for the PKWs.....	73
5.3	Mesh Generation of the PKW .....	74
	References.....	77
	Chapter 6: Experimental and Numerical Results and Discussion.....	78
6.1	Experimental results .....	78
6.2	CFD Simulation Results of $PKW_A$ , $PKW_{A\_reverse}$ and $PKW_B$ with ANSYS® Fluent™ Code.....	82
6.2.1	Comparison between $PKW_A$ and $PKW_{A\_reverse}$ and CFD model validation .....	82
6.2.2	Comparison between $PKW_A$ and $PKW_B$ models .....	90
6.2.3	Comparison between numerical results and Machiels et al. (2014) and Hu et al. (2018) equations.....	93
6.3	Discussion on the Discharge Coefficient of $PKW_A$ and $PKW_B$ .....	100

---

References.....	109
Chapter 7: Implementation of a Fish Pass in a type B PKW.....	110
7.1 Denil Fish Pass Design .....	111
7.2 Fish Pass – PKW structure .....	112
7.3 Velocity assessment of $PKW_{B-FP}$ working as a fish pass.....	116
7.4 Discharge efficiency assessment of $PKW_{B-FP}$ working as a weir .....	118
7.4.1 Upstream, downstream and lateral crests analysis .....	120
References.....	127
Chapter 8: Synthesis and Conclusions.....	129
8.1 On the Discharge Efficiency of type A and type B PKWs .....	129
8.1.1 Conclusions .....	129
8.1.2 Research Novelty and Contributions.....	131
8.2 On the Implementation of a Denil Fish Pass in a type B PKW.....	133
8.2.1 Conclusions .....	133
8.2.2 Research Novelty and Contributions.....	135
8.3 Future Improvements of the Research .....	135

## LIST OF FIGURES

Fig. 1.1. PKW type A and type B .....	4
Fig. 1.2. Type A and type B PKW inlet and outlet key comparison.....	4
Fig. 1.3 Flowchart of the strategy of research.....	6
Fig. 2.1 Flow over a sharp-crested weir .....	12
Fig. 2.2 Flow over a side weir.....	12
Fig. 2.3 Labyrinth weir at the Ruby Reservoir (USA) (source: www.johnson-wilson.com) .....	13
Fig. 2.4 PKW at the Malarce Dam (source: Frederic Laugier, EDF).....	14
Fig. 2.5 Fundamental parameters on an entire PKW - 3D view, plan view and cross section (source: Pralong et al. (2011)).....	16
Fig. 2.6 type A, type B, type C and type D PKWs.....	17
Fig. 2.7 Papaya PKW at the Black Esk reservoir (source: www.moore-concrete.com) .....	20
Fig. 3.1 Fish pass entrance and exit (Food and Agriculture Organization of the United Nations, 2002).....	44
Fig. 3.2. Fish locations at hydropower plants (Food and Agriculture Organization of the United Nations, 2002) .....	46
Fig. 3.3 Conventional pool type fish pass (Food and Agriculture Organization of the United Nations, 2002).....	47
Fig. 3.4 Vertical Slot fish pass (sources: Food and Agriculture Organization of the United Nations and upcommons.upc.edu) .....	48
Fig. 3.5 Denil fish pass (sources: Food and Agriculture Organization of the United Nations and wetlandinfo.des.qld.gov.au).....	49
Fig. 3.6 Arced-type baffle for a Denil pass (Wang <i>et al.</i> , 2012; Yu, Wang and Xie, 2012).....	51
Fig. 3.7 Baffle of a Denil pass (Food and Agriculture Organization of the United Nations, 2002).....	51

---

Fig. 3.8 Longitudinal section of a Denil pass passes (Food and Agriculture Organization of the United Nations, 2002).....	53
Fig. 3.9 CFD models of Plymesser (Plymesser, 2014).....	54
Fig. 3.10 CFD models of Mahmoudian et al. (Mahmoudian, Baharvand and Lashkar-Ara, 2019).....	54
Fig. 4.1 Isometric view of the PKW <sub>A</sub> and PKW <sub>A_reverse</sub> .....	59
Fig. 4.2 Cross section, plain view and lateral view of the tested type A model .....	59
Fig. 4.3 Cross section (top) and Plain view (bottom) schemes of the laboratory setup .....	61
Fig. 4.4 Top left) Water supply elements; top right) channel; bottom) running test on the PKW <sub>A_reverse</sub> .....	62
Fig. 4.5 Point Gauge .....	63
Fig. 4.6 Diaphragm flow meter .....	64
Fig. 4.7 Functioning principle of an ADV (source: Nortek Manuals, 2018).....	65
Fig. 4.8 Nortek Vectrino (source: Nortek Manuals, 2018) .....	65
Fig. 4.9 Velocity measuring points at the PKW <sub>A</sub> .....	68
Fig. 5.1 Isometric view of the PKW <sub>B</sub> .....	70
Fig. 5.2 Isometric view of the volumes implemented in the ANSYS® DesignModeler™ tool for the PKW <sub>B</sub> model.....	72
Fig. 5.3 Lateral and plain view of the volumes implemented in the ANSYS® DesignModeler™ tool for the PKW <sub>B</sub> model. ....	72
Fig. 5.4 Implemented Boundary Conditions and Interfaces .....	73
Fig. 5.5 Specific volumes implemented in the ANSYS® model.....	75
Fig. 5.6 Mesh $h_1$ implemented in the ANSYS® Meshing™ .....	76
Fig. 5.7 Zoom of the mesh $h_1$ in the surrounding area of the PKW implemented in the ANSYS® Meshing™. ....	77
Fig. 6.1 Experimental rating curves $C_{PKW}$ (H/P) for PKW <sub>A</sub> and PKW <sub>A_reverse</sub> .....	79
Fig. 6.2 Velocity in the X-direction for lower flowrates at Section A for the PKW <sub>A</sub> 80	
Fig. 6.3 Velocity in the X-direction for lower flowrates at Section B for the PKW <sub>A</sub> 80	
Fig. 6.4 Velocity in the X-direction for higher flowrates at Section A for the PKW <sub>A</sub> 81	

---

---

Fig. 6.5 Velocity in the X-direction for higher flowrates at Section B for the PKW <sub>A</sub>	81
Fig. 6.6 Experimental and Numerical rating curves $C_{PKW}$ (H/P) for PKW <sub>A</sub> and PKW <sub>A_reverse</sub> .....	82
Fig. 6.7 Numerical rating curves $C_{PKW}$ (H/P) for PKW <sub>A</sub> and PKW <sub>A_reverse</sub> .....	84
Fig. 6.8 Analytical equations for the discharge coefficient $C_{PKW}$ (H/P) curves for PKW <sub>A</sub> .....	85
Fig. 6.9 Analytical equations for the discharge coefficient $C_{PKW}$ (H/P) curves for PKW <sub>A_reverse</sub> .....	85
Fig. 6.10 Comparison of velocities in the X-direction for lower flowrates at Section A for the PKW <sub>A</sub> .....	87
Fig. 6.11 Comparison of velocities in the X-direction for higher flowrates at Section A for the PKW <sub>A</sub> .....	88
Fig. 6.12 Comparison of velocities in the X-direction for lower flowrates at Section B for the PKW <sub>A</sub> .....	88
Fig. 6.13 Comparison of velocities in the X-direction for higher flowrates at Section B for the PKW <sub>A</sub> .....	89
Fig. 6.14 Numerical rating curves $C_{PKW}$ (H/P) for PKW <sub>A</sub> and PKW <sub>B</sub> .....	91
Fig. 6.15 Analytical equations for the discharge coefficient $C_{PKW}$ (H/P) curves for PKW <sub>B</sub> .....	92
Fig. 6.16 Comparison of the PKW <sub>A</sub> total specific discharge between numerical results and those obtained by Machiels et al. (2014) and Hu et al. (2018) .....	94
Fig. 6.17 Comparison of the PKW <sub>A</sub> specific discharge over the upstream crest between numerical results and those obtained by Machiels et al. (2014) and Hu et al. (2018) .....	95
Fig. 6.18 Comparison of the PKW <sub>A</sub> specific discharge over the downstream crest between numerical results and those obtained by Machiels et al. (2014) and Hu et al. (2018) .....	95

---

---

Fig. 6.19 Comparison of the PKW <sub>A</sub> specific discharge over the lateral crest between numerical results and those obtained by Machiels et al. (2014) and Hu et al. (2018) .....	96
Fig. 6.20 Comparison of the PKW <sub>B</sub> total specific discharge between numerical results and those obtained by Machiels et al. (2014) and Hu et al. (2018).....	97
Fig. 6.21 Comparison of the PKW <sub>B</sub> specific discharge over the UC between numerical results and those obtained by Machiels et al. (2014) and Hu et al. (2018).....	98
Fig. 6.22 Comparison of the PKW <sub>B</sub> specific discharge over the DC between numerical results and those obtained by Machiels et al. (2014) and Hu et al. (2018).....	99
Fig. 6.23 Comparison of the PKW <sub>B</sub> specific discharge over the LC between numerical results and those obtained by Machiels et al. (2014) and Hu et al. (2018).....	99
Fig. 6.24 Discharge over the upstream (UC), downstream (DC) and lateral crests (LC) of the PKW <sub>A</sub> and PKW <sub>B</sub> .....	101
Fig. 6.25 Discharge ratio of the upstream (UC), downstream (DC) and lateral crests (LC) of the PKW <sub>A</sub> and PKW <sub>B</sub> .....	101
Fig. 6.26 Energy vs Discharge curves of the PKW <sub>A</sub> and PKW <sub>B</sub> from the upstream crest .....	102
Fig. 6.27 Energy vs Discharge curves of the PKW <sub>A</sub> and PKW <sub>B</sub> from the downstream crest.....	102
Fig. 6.28 Energy vs Discharge curves of the PKW <sub>A</sub> and PKW <sub>B</sub> from the lateral crests .....	103
Fig. 6.29 Head over the upstream, downstream and lateral crests of the PKW <sub>A</sub> and PKW <sub>B</sub> .....	104
Fig. 6.30 Discharge Coefficient of the upstream, downstream and lateral crests of the PKW <sub>A</sub> and PKW <sub>B</sub> .....	105
Fig. 6.31 Velocity distribution in the main flow direction on the inlet key for the PKW <sub>A</sub> and PKW <sub>B</sub> .....	106
Fig. 6.32 Water volume fraction on the inlet key for the PKW <sub>A</sub> and PKW <sub>B</sub> .....	107
Fig. 6.33 Outlet key location for PKW <sub>A</sub> and PKW <sub>B</sub> .....	108
Fig. 6.34 Water volume fraction on the outlet key for the PKW <sub>A</sub> and PKW <sub>B</sub> .....	108

---

---

Fig. 7.1 Implemented Boundary Conditions and Interfaces.....	112
Fig. 7.2 Relation of $h^*=f(h_0)$ (Food and Agriculture Organization of the United Nations, 2002).....	113
Fig. 7.3 Isometric views of the combined PKW and fish pass structure, $PKW_{B-FP}$ .....	114
Fig. 7.4 Cross, lateral and plain view of the $PKW_{B-FP}$ .....	115
Fig. 7.5 Cross, lateral and plain view of the $PKW_{B-FP}$ at real scale. ....	116
Fig. 7.6 Water velocity distribution in real scale in the middle of the fish pass of the $PKW_{B-FP}$ . ....	117
Fig. 7.7 Baffle location at the $PKW_{B-FP}$ .....	117
Fig. 7.8 Velocity distribution at the baffles 1, 5, 10 and 15 of the $PKW_{B-FP}$ .....	118
Fig. 7.9 Numerical rating curves $C_{PKW}(H/P)$ for $PKW_B$ and $PKW_{B-FP}$ .....	119
Fig. 7.10 Scheme of the total height and height of the upstream crest of the $PKW_{B-FP}$ .....	120
Fig. 7.11 Discharge over the upstream (UC), downstream (DC) and lateral crests (LC) of the $PKW_B$ and $PKW_{B-FP}$ .....	121
Fig. 7.12 Discharge comparison between the results obtained from Odeh's equation (Odeh, 2003) and from the CFD model for the upstream crest.....	122
Fig. 7.13 Energy vs Discharge curves of the $PKW_B$ and $PKW_{B-FP}$ from the upstream crest.....	123
Fig. 7.14 Head over the upstream, downstream and lateral crests of the $PKW_B$ and $PKW_{B-FP}$ .....	124
Fig. 7.15 Discharge Coefficient of the upstream, downstream and lateral crests of the $PKW_B$ and $PKW_{B-FP}$ .....	125
Fig. 7.16 Water volume fraction on the outlet key for the $PKW_B$ and $PKW_{B-FP}$ .....	126

## LIST OF TABLES

Tab. 2.1 Fundamental parameters on an entire PKW.....	16
Tab. 3.1 Guide values for channel widths and slopes in Denil passes (Food and Agriculture Organization of the United Nations, 2002).....	50

---

---

Tab. 3.2 Guide values for baffles dimensions in Denil passes (Food and Agriculture Organization of the United Nations, 2002).....	52
Tab. 4.1 Geometry parameters for $PKW_A$ and $PKW_{A\_reverse}$ .....	60
Tab. 4.2 Dimensionless ratios for $PKW_A$ and $PKW_{A\_reverse}$ .....	60
Tab. 5.1 Geometric parameters and dimensionless ratios of the $PKW_B$ tested model. .....	71
Tab. 5.2 Mesh resolutions tested for the Mesh Convergence Method.....	76
Tab. 6.1 Flowrates and dimensionless H/P ratios tested for $PKW_A$ and $PKW_{A\_reverse}$ .....	78
Tab. 6.2 Relative scatters between the numerical and experimental results for the discharge coefficient of the $PKW_A$ and the $PKW_{A\_reverse}$ .....	83
Tab. 6.3 Minimum and maximum relative errors between author's equations and numerical results for the $PKW_A$ and $PKW_{A\_reverse}$ .....	86
Tab. 6.4 Minimum, maximum and average relative errors of velocity experimental and numerical results for the $PKW_A$ at sections A and B .....	89
Tab. 6.5 Upstream head and discharge coefficient comparison between the $PKW_A$ and the $PKW_B$ . .....	91
Tab. 6.6 Minimum and maximum relative errors between author's equations and numerical results.....	92
Tab. 6.7 Relative errors and MAPE of the $PKW_A$ specific discharges between numerical results and those obtained by Machiels et al. (2014).....	96
Tab. 6.8 Relative errors and MAPE of the $PKW_A$ specific discharges between numerical results and those obtained Hu et al. (2018).....	97
Tab. 6.9 Relative errors of the $PKW_B$ specific discharges between numerical results and those obtained by Machiels et al. (2014).....	100
Tab. 6.10 Relative errors of the $PKW_B$ specific discharges between numerical results and those obtained Hu et al. (2018).....	100
Tab. 7.1 Baffles dimensions of the fish pass.....	112
Tab. 7.2 Dimensions of the combined structure $PKW_{B-FP}$ . .....	114
Tab. 7.3 Dimensions of the combined structure $PKW_{B-FP}$ . .....	115

---

Tab. 7.4 Water level, upstream velocity, head and discharge coefficient comparison between the  $PKW_B$  and the  $PKW_{B-FP}$ ..... 120

Tab. 8.1 Range of dimensionless parameters ratios tested on literature..... 132

---

**LIST OF SYMBOLS**

▪ $a$	[-]	Leite Ribeiro et al. (2012) Correlation Parameter
▪ $a^*$	[-]	Hu et al. (2018) Correlation Parameter
▪ $b$	[-]	Width of a Denil pass baffle
▪ $b_a$	[m]	Clear width of a Denil pass baffle
▪ $b_{LR}$	[-]	Leite Ribeiro et al. (2012) Correlation Parameter
▪ $c_1$	[m]	Distance from the bottom to invert of V-section of a Denil pass baffle
▪ $c_2$	[m]	Distance from the bottom to the end of the triangular section of a Denil pass baffle
▪ $e$	[-]	Machiels et al. (2014) Correlation Parameter
▪ $e^*$	[-]	Hu et al. (2018) Correlation Parameter
▪ $e_r$	[-]	Relative Error
▪ $g$	[ms <sup>-2</sup> ]	Acceleration of Gravity
▪ $h$	[m]	Water depth
▪ $h_a$	[m]	Height of a baffle in a Denil pass
▪ $h_E$	[m]	Water depth in channel upstream of Denil pass measured from channel floor
▪ $h_u$	[m]	water depth in upstream reservoir above V-notch of uppermost baffle
▪ $h^*$	[m]	Upstream water depth from the V-notch in a Denil pass
▪ $l$	[m]	Fish pass channel length
▪ $p$	[-]	Leite Ribeiro et al. (2012) Correlation Parameter
▪ $q$	[m <sup>3</sup> s <sup>-1</sup> m <sup>-1</sup> ]	Flowrate for unit length
▪ $r$	[-]	Leite Ribeiro et al. (2012) enhanced discharge ratio
▪ $s$	[m]	Space between baffles on a Denil pass
▪ $s^*$	[m]	Standard Deviation
▪ $t$	[s]	Time
▪ $t_{95}$	[s]	The 95th Percentile of the Two-Tailed t-Student Distribution
▪ $v$	[ms <sup>-1</sup> ]	Velocity
▪ $\bar{v}$	[ms <sup>-1</sup> ]	Average Velocity
▪ $w$	[-]	Leite Ribeiro et al. (2012) Correlation Parameter
▪ $x_i$	[-]	Individual Measurements
▪ $\bar{x}$	[-]	Sample Mean Value
▪ $B$	[-]	Fixed or Bias Error
▪ $B$	[m]	Total Lateral Length
▪ $B_b$	[m]	Length of the PKW base
▪ $B_i$	[m]	Overhang length of the inlet key
▪ $B_o$	[m]	Overhang length of the outlet key
▪ $C$	[ms <sup>-1</sup> ]	Speed of Sound in Fluid
▪ $C_D$	[-]	Discharge Coefficient
▪ $C_{PKW}$	[-]	Discharge Coefficient of PKW
▪ $C_S$	[-]	Discharge Coefficient of Submerged Flow

---

---

▪ $E$	[m]	Energy of water
▪ $F$	[-]	Froude Number
▪ $F_{source}$	[Hz]	Transmitted Frequency
▪ $H$	[m]	Water Head
▪ $H_{crest}$	[m]	Water Head Over A Single Crest
▪ $I$	[-]	Physical Slope
▪ $K$	[m <sup>1/3</sup> s <sup>-1</sup> ]	Gauckler-Strickler Coefficient
▪ $K_d$	[-]	Hu et al. (2018) Correlation Parameter
▪ $K_i$	[-]	Hu et al. (2018) Correlation Parameter
▪ $K_s$	[-]	Hu et al. (2018) Correlation Parameter
▪ $K_u$	[-]	Hu et al. (2018) Correlation Parameter
▪ $K_W$	[-]	Hu et al. (2018) Correlation Parameter
▪ $K_{Wi}$	[-]	Machiels et al. (2014) Correlation Parameter
▪ $K_{Wo}$	[-]	Machiels et al. (2014) Correlation Parameter
▪ $L$	[m]	Total Developed Length
▪ $L_u$	[m]	Unit Length
▪ $N_u$	[-]	Number of PKW Units
▪ $N^*$	[-]	Number of Measurements
▪ $P$	[m]	PKW Height
▪ $P_d$	[m]	Height of the Base of a PKW
▪ $P_e$	[m]	Machiels et al. (2014) Mean Lateral Crest Height
▪ $P_e^*$	[m]	Hu et al. (2018) Mean Lateral Crest Height
▪ $P_i$	[m]	Inlet Key Height
▪ $P_o$	[m]	Outlet Key Height
▪ $P_p$	[m]	Parapet Wall Height
▪ $Q$	[m <sup>3</sup> s <sup>-1</sup> ]	Flow Rate
▪ $R$	[m]	Radius of a rounded crest
▪ $R_e$	[-]	Random Error or Precision Error
▪ $S_{cr}$	[-]	Critical Slope
▪ $S_i$	[m]	Inlet Key Slope
▪ $S_o$	[m]	Outlet Key Slope
▪ $T_s$	[m]	Wall Thickness
▪ $T_p$	[m]	Parapet Wall Thickness
▪ $U$	[-]	Uncertainty
▪ $V$	[ms <sup>-1</sup> ]	Current Velocity
▪ $W$	[m]	Width
▪ $W_i$	[m]	Inlet Key Width
▪ $W_o$	[m]	Outlet Key Width
▪ $W_u$	[m]	Unit Width
▪ $\alpha$	[-]	Machiels et al. (2014) Correlation Parameter
▪ $\beta$	[-]	Machiels et al. (2014) Correlation Parameter
▪ $\gamma^*$	[-]	Machiels et al. (2014) Correlation Parameter
▪ $\delta$	[-]	Leite Ribeiro et al. (2012) Correlation Parameter
▪ $\delta_I$	[-]	Machiels et al. (2014) Correlation Parameter

---

- $\delta_2$  [-] Machiels et al. (2014) Correlation Parameter
- $\zeta$  [-] Leite Ribeiro et al. (2012) Reduction Factor
- $\lambda$  [-] Scale Factor
- $\Delta$  [-] Relative difference between two parameters
- $\Delta h_{diaph}$  [m] Differential of Values Measured at the Pitot Tubes using a Diaphragm Flow Meter
- $\Delta\varphi$  [-] Phase Difference

## **LIST OF SUBSCRIPTS**

- $d$  [-] Downstream
- $i$  [-] Inlet
- $o$  [-] Outlet
- $u$  [-] Unit
- $up$  [-] Upstream
- $x$  [-] Streamwise Direction
- $DC$  [-] Downstream Crest
- $LC$  [-] Lateral Crest
- $UC$  [-] Upstream Crest

## **LIST OF ABBREVIATIONS**

- ADV Acoustic Doppler Velocimeter
- ATPKW Arced Trapezoidal Piano Key Weir
- CFD Computational Fluid Dynamics
- DC Downstream Crest
- FAO Food and Agriculture Organization of the United Nations
- GCI Grid Convergence Index
- LES Large Eddy Simulation
- LC Lateral Crest
- LSW Linear Side Weir
- MAPE Mean Average Percentage Error
- PKSW Piano Key Side Weir
- PKW Piano Key Weir
- RLSW Rectangular Labyrinth Side Weir
- RLW Rectangular Labyrinth Weir
- RNG Re-Normalize Group
- SNR Sound-to-Noise Ratio
- TPKW Trapezoidal Piano Key Weir
- UC Upstream Crest



---

## Chapter 1

### Introduction

---

Within the hydrologic cycle, the global values of the evaporation and precipitation balance each other out, however, the characteristics of both phenomena are significantly different. Evaporation is a continuous slow process while precipitation is a highly discontinuous, fast and localized event (Trenberth, 2011). Furthermore, Climate Change has influenced the global hydroclimatic response (Tebaldi *et al.*, 2006; Pendergrass and Hartmann, 2014), leading to an increase in global temperatures, an increase in frequency and intensity of wet extremes in Northern Europe, America and Australia and an increase in dry spell length along with a reduction of wet days in Southern Europe, India, Asia, Africa and America (Giorgi *et al.*, 2011; Sillmann *et al.*, 2013; Giorgi, Coppola and Raffaele, 2014). These conditions lead to a higher risk of flooding events and droughts directly affecting the environment and the society. In fact, these extreme weather events affect the functioning of health care, as well as changes in demand for services due to the impact of extreme weather events on human health (Curtis *et al.*, 2017). Likewise, the mean expected annual damages in Europe caused by these events is ~€1.6 billion per year, increasing to almost ~€5.5 billion per year with an increase of 3 °C of global warming. Taking also into consideration the expected annual output losses, which include undirected effects, the amount of ~€0.3 billion a year should be added for the current situation and around ~€1.2 billion a year

with 3 °C of global warming (Koks *et al.*, 2019). Worldwide, an increase of 1.5 °C of global warming would cost of ~€9.05 trillion per year (Jevrejeva *et al.*, 2018).

Due to the severity of this issue, these changes have been and should be considered to properly design safety hydraulic infrastructures, especially when achieving a higher discharge capacity. One of the most common hydraulic control structures is the weir, with a discharge capacity directly proportional to the width of the weir for a given water head and its crest shape. Considering a sharp-crest rectangular weir for a given space, there is the possibility to increase the crest, thus the discharge capacity, by folding the weir in plain view generating a non-linear weir.

The idea of folded crested weirs brought to develop labyrinth weirs in the thirties of last Century with an arrangement that is grounded on vertical walls, located frontally to the flow direction. Murphy (Murphy, 1909) appeared to be the first who highlighted the advantages of labyrinth weirs, while the first hydraulic study on them was conducted by the Bruno Gentilini (1907-1998) at the Politecnico di Milano (Gentilini, 1941). Afterwards, Piano Key Weir (PKW) arose from the effort of reducing the base of a labyrinth weir (Lempérière and Ouamane, 2003; Ouamane and Lempérière, 2006). The PKW planform is defined by a rectangular shape, but unlike the labyrinth weir, the apexes are inclined by turns in upstream and in downstream direction. This layout results in a weir with a smaller footprint, which makes the PKW more suitable to place on top of the dams, able to also increase storage volume, and improving the discharge capacity in comparison with other spillway types. From the economic, constructability and operative viewpoints, PKWs are also cost-competitive and ever more economical in some cases compared to labyrinth weir and spillway gates, showing lower operational and maintenance costs (Paxson, Tullis and Hertel, 2013).

Non-linear weirs are often applied to upgrade existing dams, by increasing their storage volume or improving their discharge capacity. Additionally, there are several beneficial effects from installing these structures on rivers and channels; for instance, raising the water level increases the power capacity in hydroelectric

plants (Eichenberger, 2014). Within this context, non-linear weirs allow discharging more water in comparison with linear weirs while controlling the upstream water level during flooding events, which ultimately helps to avoid the overtopping of the banks. Nonetheless, for decades, humans have modified water bodies by building many structures, resulting in altered habitats, modified flows, loss of river continuity and connectivity and especially severe damaging impacts on the aquatic environment (Nilsson and Berggren, 2000; Nilsson *et al.*, 2005; Moore, Arrigoni and Wilcox, 2012). Fish movements play an essential role for human population, such as food consumption, as well as for ecosystems welfare, so the anthropogenic barrier strongly affect populations and the persistence of some species (Lucas and Baras, 2001; Radinger and Wolter, 2014).

In Europe, the most common pressures on surface water bodies are hydromorphological, therefore, efforts must be done to ensure the maintenance of fish habitats. Within this context, the European Environment Agency (European Environment Agency, 2018) established policies to the restoration of surface water bodies. One of the main problems of installing hydraulic structures in rivers is their detrimental impact on fish migration. An effective solution to improve this situation is installing fish passes, which are structures designed to facilitate a safe fish movement to overtake an obstacle, improving the river connectivity (Schilt, 2007; Calles and Greenberg, 2009).

## **1.1 Problem Statement**

The location of PKWs in rivers allows increasing the water level for numerous purposes, such as hydropower exploitation, while their higher discharge efficiency, helps to prevent floods caused by overtopping of the banks. Nevertheless, the installation of weirs on rivers would endanger fish movements and related ecosystems. Hence, following the European Environment Agency established policies to ensure the restoration of fish habitats, the combination of a PKW with a fish pass would allow fish to overcome the barrier created by the PKW structure itself.

Regardless, the PKW geometry is particularly complex due to the significant number of geometric parameters involved and the discharge efficiency is strongly dependent on its geometry. Different types of PKW were defined according to their overhangs: type A has symmetric overhangs, type B has a single upstream overhang, type C has a single downstream overhang and type D does not have overhangs (Ercicum *et al.*, 2017). Considering a type A and a type B, with same dimensionless ratios in terms of height, developed length and inlet and outlet key widths, the type B is characterized by a smaller outlet key slope in comparison with type A (Figures 1.1 and 1.2), which turns the type B more suitable to be combined with a fish pass.

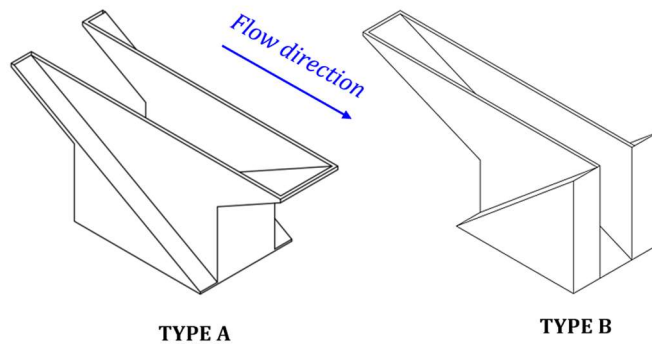


**Fig. 1.1. PKW type A and type B**

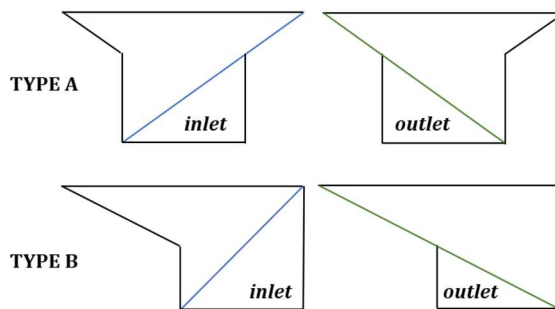


**Fig. 1.2. Type A and type B PKW inlet and outlet key comparison**

Nonetheless, the length of the overhangs influences the inlet and outlet key cross sections and slopes, altering the velocity field along the keys, thus affecting the discharge capacity (Machiels, 2012). Several authors have studied the

beforementioned PKW types, however, reaching different conclusions. Namely, Noui and Ouamane (Noui and Ouamane, 2011) and Cicero and Delisle (Cicero and Delisle, 2013) observed that type B was more efficient than type A whereas Machiels et al. (Machiels, 2012) found out that the type B configuration is the most efficient for low heads, however, this efficiency decreases for higher heads and the gain becomes negligible compared to the type A.

## 1.2 Research Objectives

The objectives for this Ph.D. research are to compare the discharge efficiency between type A and type B PKWs and to study the viability of combining a type B PKW with a fishway proposing a new structure which joins the beneficial effects of the PKW discharge efficiency with the possibility to create a passage for fishes, aiming at overcoming the barrier created by the PKW structure on the river.

In greater detail, the main goals aim at:

- Assessing the hydraulic behaviour of type A and type B PKWs, which includes:
  - Designing a type A PKW geometry based on the optimal dimensionless ratios found in literature and a type B with the same dimensionless parameters ratios, in exception of  $B_i/B_o=0$ .
  - Performing experimental investigations of the type A model, in the designed configuration, with  $W_i/W_o=1.5$  and rotated  $180^\circ$ , resulting in a PKW with  $W_i/W_o=0.67$ .
  - Developing a Computational Fluid Dynamics (CFD) code to characterize the hydraulic behaviour of the designed PKWs, validated using the data from the experimental setup and the literature equations for the estimation of the discharge coefficient.
- Assessing the effectiveness as a fish pass and the discharge efficiency of the combined PKW-fish pass structure, which involves:
  - Defining the biological and hydraulic range of the fish pass, thus, the fish pass geometric features.

- Implementing the designed fish pass in the outlet key of the tested type B PKW.
- Evaluating the velocity field, water level and discharge of the combined structure for a wide range of upstream head, through the implementation of the structure in the calibrated CFD model.

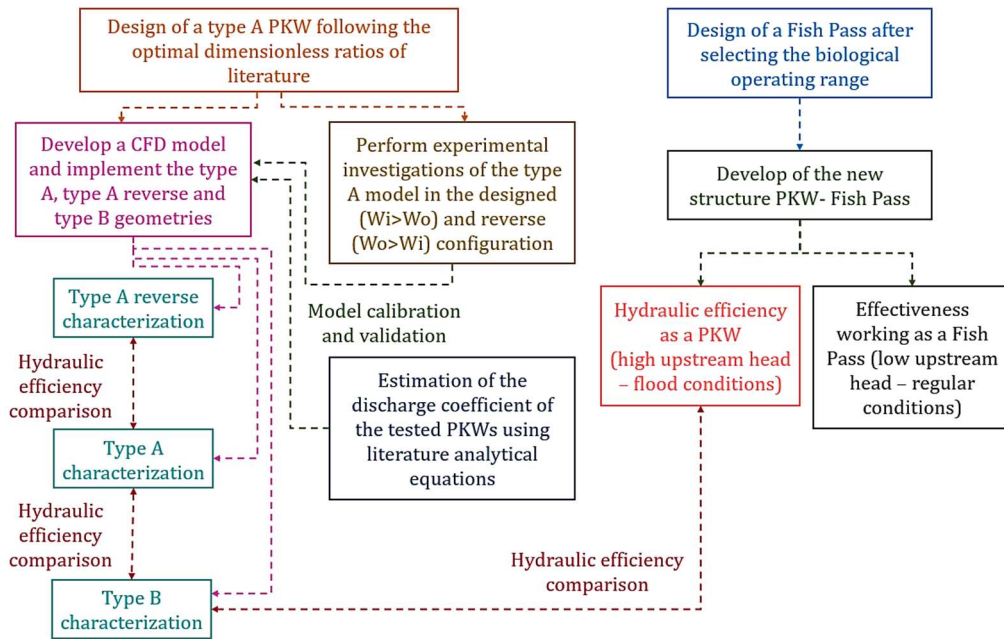


Fig. 1.3 Flowchart of the strategy of research

### 1.3 Outline of the Thesis

The thesis presents the following structure:

- **Chapter 1**, which contains a brief introduction of the treated topic, and the research objectives and procedures.
- **Chapter 2**, in which a wide review of the engineering literature related to the PKW research is presented, drawing particularly the attention to the geometric features, discharge efficiency and hydraulic behaviour of PKWs.
- **Chapter 3**, in which an overview of the environmental issues related to aquatic ecosystems and a literature review related to Fish Passes are presented.

- **Chapter 4**, in which the applied procedure and results of an experimental analysis on two type A PKW geometries are reported and discussed. The laboratory experiences are illustrated and the criteria to assess the discharge coefficient efficiency and the velocity field are introduced.
- **Chapter 5**, where the procedure for in Computational Fluid Dynamics (CFD) modelling is introduced by implementing three PKW geometries: the two type A tested experimentally and a type B PKW.
- **Chapter 6**, in which numerical and experimental results are presented, making evidence of the model ability to reproduce the hydraulic behaviour of PKWs to both estimate the discharge coefficient and evaluate the fluid dynamics field, including water level, velocity distribution and discharge.
- **Chapter 7**, where the combined structure of the PKW – Fish Pass is introduced, including the definition of the biological and hydraulic range and the evaluation of the velocity field of the structure functioning as a fish pass and the assessment of the discharge coefficient of the structure working as a weir, comparing it with the original tested type B PKW.
- **Chapter 8**, in which a brief synthesis of the content and achieved results is included, stating their contribution to the engineering research. The potential improvements, connected to the considered research, are also specified.

## References

- Calles, O. and Greenberg, L. (2009) “Connectivity is a two-way street-the need for a holistic approach to fish passage problems in regulated rivers,” *River Research and Applications*, 25(10), pp. 1268–1286. doi:10.1002/rra.1228.
- Cicero, G.M. and Delisle, J.R. (2013) “Discharge characteristics of Piano Key weirs under submerged flow,” in *Labyrinth and Piano Key Weirs II – PKW 2013*, pp. 101–109.
- Eichenberger, P. (2014) “The first commercial Piano Key Weir in Switzerland,” in *Labyrinth and Piano Key Weirs II - PKW 2013*, pp. 227–234.
- Erpicum, S. et al. (2017) “Hydraulics of Piano Key Weirs: A review,” in Erpicum, S. et al. (eds) *Labyrinth and Piano Key Weirs III – PKW 2017*, pp. 27–36.
- European Environment Agency (2018) *European waters - assessment of status and pressures 2018*.
- Giorgi, F. et al. (2011) “Higher Hydroclimatic Intensity with Global Warming,” *Journal of Climate*, 24(20), pp. 5309–5324. doi:10.1175/2011JCLI3979.1.
- Giorgi, F., Coppola, E. and Raffaele, F. (2014) “A consistent picture of the hydroclimatic response to global warming from multiple indices: Models and observations,” *Journal of Geophysical Research: Atmospheres*, 119(20), pp. 11,695–11,708. doi:10.1002/2014JD022238.
- Jevrejeva, S. et al. (2018) “Flood damage costs under the sea level rise with warming of 1.5 °C and 2 °C,” *Environmental Research Letters*, 13(7). doi:10.1088/1748-9326/aacc76.
- Koks, E.E. et al. (2019) “The macroeconomic impacts of future river flooding in Europe,” *Environmental Research Letters* [Preprint]. doi:10.1088/1748-9326/ab3306.
- Lempérière, F. and Ouamane, A. (2003) “The Piano Keys weir: A new cost-effective solution for spillways,” *International Journal on Hydropower and Dams* [Preprint].
- Lucas, M.C. and Baras, E. (2001) *Migration of freshwater fishes*. Blackwell Science Ltd.

- Machiels, O. (2012) Experimental study of the hydraulic behaviour of Piano Key Weirs.
- Moore, J.N., Arrigoni, A.S. and Wilcox, A.C. (2012) “Impacts of Dams on Flow Regimes in Three Headwater Subbasins of the Columbia River Basin, United States 1,” *JAWRA Journal of the American Water Resources Association*, 48(5), pp. 925–938. doi:10.1111/j.1752-1688.2012.00660.x.
- Nilsson, C. et al. (2005) “Fragmentation and Flow Regulation of the World’s Large River Systems,” *Science*, 308(5720), pp. 405–408. doi:10.1126/science.1107887.
- Nilsson, C. and Berggren, K. (2000) “Alterations of Riparian Ecosystems Caused by River Regulation,” *BioScience*, 50, pp. 783–792.
- Noui, A. and Ouamane, A. (2011) “Study of optimization of the Piano key weir,” in *Labyrinth and Piano Key Weirs - Proceedings of the International Conference on Labyrinth and Piano Key Weirs, PKW 2011*. doi:10.1201/b12349-27.
- Ouamane, A. and Lempérière, F. (2006) “Design of a new economic shape of weir,” in *Proceedings of the International Symposium on Dams in the Societies of the 21st Century, ICOLD-SPANCOLD - Dams and Reservoirs, Societies and Environment in the 21st Century*. doi:10.1201/b16818-74.
- Paxson, G.S., Tullis, B.P. and Hertel, D.J. (2013) “Comparison of piano keyweirs with labyrinth and gated spillways: Hydraulics, cost, constructability and operations,” in *Labyrinth and Piano Key Weirs II*. doi:10.1201/b15985.
- Pendergrass, A.G. and Hartmann, D.L. (2014) “Changes in the Distribution of Rain Frequency and Intensity in Response to Global Warming\*,” *Journal of Climate*, 27(22), pp. 8372–8383. doi:10.1175/JCLI-D-14-00183.1.
- Radinger, J. and Wolter, C. (2014) “Patterns and predictors of fish dispersal in rivers.,” *Fish and Fisheries*, 15(3), pp. 456–473.
- Schilt, C.R. (2007) “Developing fish passage and protection at hydropower dams,” *Applied Animal Behaviour Science*, 104(3–4), pp. 295–325. doi:10.1016/j.applanim.2006.09.004.

- Sillmann, J. et al. (2013) "Climate extremes indices in the CMIP5 multimodel ensemble: Part 2. Future climate projections," *Journal of Geophysical Research: Atmospheres*, 118(6), pp. 2473–2493. doi:10.1002/jgrd.50188.
- Tebaldi, C. et al. (2006) "Going to the Extremes," *Climatic Change*, 79(3–4), pp. 185–211. doi:10.1007/s10584-006-9051-4.
- Trenberth, K.E. (2011) "Changes in precipitation with climate change," *Climate Research* [Preprint]. doi:10.3354/cr00953.

## Chapter 2

# Piano Key Weir (PKW) Research

---

### 2.1 Weirs and spillways

Weirs or spillways are hydraulic structures that allows water to flow over their crest, enabling the passage of excess water when wet extremes occur, therefore, they are fundamental to provide safety. The discharge capacity is related to the amount of water flow discharges downstream for a given upstream head. Their efficiency is directly correlated to the weir crest length and shape, as shown in the Poleni's equation:

$$Q = \frac{2}{3} C_D W \sqrt{2gH^3} \quad (2.1)$$

where Q is the water flow over passing over the crest [ $\text{m}^3 \text{s}^{-1}$ ],  $C_D$  is the discharge coefficient, related to the weir type [-], W is the width of the weir [m], g is the acceleration of gravity [ $\text{m s}^{-2}$ ] and H the head over the weir [m], which can be calculated as:

$$H = h + v^2/2g \quad (2.2)$$

where h is the water level over the crest [-] and v is the flow velocity [ $\text{m s}^{-1}$ ].

Several weir types have been implemented and studied until the development of Piano Key Weir (PKW). In this chapter, the main weir types that brought to develop the PKW are presented, as a way to improve the understanding of the PKW hydraulic behaviour.

#### 2.1.1 Sharp-crest weirs

A sharp-crested weir consists of a vertical flat plate with a sharp edge at the top placed transversally to the main flow direction. Figure 2.1 shows the longitudinal section of the flow passing over a sharp-crested weir.

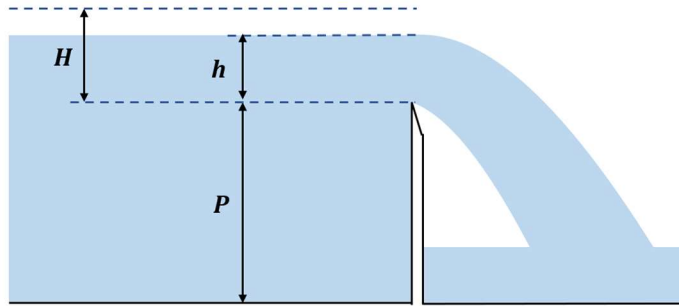


**Fig. 2.1** Flow over a sharp-crested weir

The discharge capacity can be calculated using the Poleni's equation, with a discharge coefficient,  $C_D$ , approximately equal to 0.43 for sharp-crested weirs (Johnson, 2000), however, this coefficient varies depending on the weir thickness and height.

### 2.1.2 Side weirs

A side weir is weir located parallel to the main flow direction (Figure 2.2) instead of transversally. Its discharge capacity is influenced by the variation of flow depth along the weir crest, the flow velocity and the outflow angle, thus, the discharge coefficient is variable and depends on these parameters.

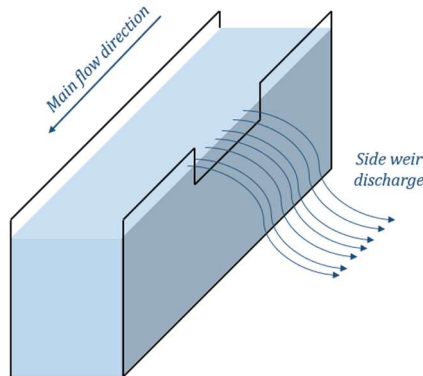


**Fig. 2.2** Flow over a side weir

### 2.1.3 Labyrinth weirs

Considering a sharp-crest rectangular weir for a given space, there is the possibility to increase the crest, thus the discharge capacity, by folding the weir in plain view. This idea of folded crested weirs brought to develop non-linear weirs, such as labyrinth weirs, in the thirties of last Century with an arrangement that is grounded on vertical walls, located frontally to the flow direction (Murphy, 1909; Gentilini, 1941).

The discharge capacity of labyrinth weirs is related to the total lateral crest length, also known as developed length,  $L$ , however, the discharge capacity decreases at increasing the head because of nappe interactions (Tullis *et al.*, 1995).

Regardless, non-linear weirs are often applied to upgrade existing dams, allowing to increase their storage volume and to provide a spillway with higher discharge capacity. Furthermore, there are several beneficial effects from installing these structures on rivers and channels, such as raising the water level which allows navigation to areas that would otherwise be inaccessible and increasing the waterpower in hydroelectric plants, as well (Schleiss, 2011).



**Fig. 2.3 Labyrinth weir at the Ruby Reservoir (USA)** (source: [www.johnson-wilson.com](http://www.johnson-wilson.com))

## 2.2 Piano Key Weirs

After the development of labyrinth weirs, PKWs arose from the effort of reducing the base of a labyrinth weir. The PKW planform has a rectangular shape, but unlike the labyrinth weir, the apexes are inclined by turns in upstream and in downstream direction. This layout results in a weir with a smaller footprint, which makes the PKW more suitable to place on top of the dams, as the spillway structure, increasing the storage volume.

The PKW was first proposed by Lemperiere (Hydrocoop, France) and Ouamane (Biskra University, Algeria) in 2003 with the following targets: (a) can be placed on new or existing dams (b) easy and simple to build in all the countries. They presented two different solutions: the first one with similar upstream and downstream overhangs and a second one with only an upper overhang (Lempérière and Ouamane, 2003; Ouamane and Lempérière, 2006).



**Fig. 2.4 PKW at the Malarce Dam** (source: Frederic Laugier, EDF)

The interest in PKWs emerged after observing the increase of discharge efficiency in comparison with pre-existing weirs. For instance, Blancher et al. (Blancher, Montarros and Laugier, 2011) compared the velocity field, specific discharge and discharge coefficient of the general structure and along the crest for labyrinth and PKW geometries. They concluded that the specific discharge of the

PKW is about 20% higher than the labyrinth weir, mainly due to the discharge efficiency along the lateral crests. Moreover, Paxton et al. (Paxson, Tullis and Hertel, 2013) compared a PKW with labyrinth weirs and gated spillways based on economic, design, operational, and hydraulic considerations. They concluded that PKWs are cost competitive and even more economical in some of the solutions, indeed, PKWs can be a better alternative to gated spillways, given their lower operational and maintenance costs.

Since their first design, several studies have been carried out to both optimize their geometric design trying to understand their hydraulic behaviour and point out their strengths and lacking points. In this section, the main research performed on PKWs is presented, remarking the gaps that this research aims to fill.

### **2.2.1 PKW geometry**

The PKW geometry appears significantly complex due to the significant number of geometric parameters involved. Hence, aiming at making the design of PKWs more approachable, a specific nomenclature was defined by a workshop formed by EDF, LCH, École Polytechnique Fédérale de Lausanne and University of Liège (Pralong, Vermeulen, *et al.*, 2011) to both define a uniform notation and limit the number of parameters to the fundamental properties of this device. The fundamental element of the PKW is a unit, defined as two side walls, an inlet and two half outlet keys and it represents the smallest complete structure inside the PKW. The inlet key is the alveoli opened on the upstream part and is delimited by two side walls and the downstream crest. The outlet key is the alveoli opened on the downstream part and is confined by two side walls and the upstream crest. The main geometric parameters of a unit are the width of the inlet and outlet keys,  $W_i$  and  $W_o$ , the height of the inlet and outlet keys,  $P_i$  and  $P_o$ , the slopes of the inlet and outlet keys,  $S_i$  and  $S_o$ , the upstream and downstream overhangs lengths,  $B_o$  and  $B_i$ , the total PKW length,  $B$ , the length of the base,  $B_b$ , and the crest thickness  $T_s$ . Moreover, the parapet wall is a vertical extension that can be placed over a part or the entire PKW crest. The geometry of the parapet wall is mainly defined by its

height,  $P_p$ , and thickness,  $T_p$ . The inlet and outlet keys heights include the possible parapet wall height. The unit width,  $W_u$ , is calculated as  $W_u = W_i + W_o + 2 \cdot T_s$  and the unit length,  $L_u$ , is calculated as  $L_u = 2 \cdot B + W_u$ . If the PKW is constituted by several units, the total width of the PKW,  $W$ , is calculated as  $W = N_u \cdot W_u$  and the developed length,  $L$ , as  $L = N_u \cdot L_u$ , where  $N_u$  is the number of PKW units. All these parameters are collected in Table 2.1, although additional parameters could be added to integrate new features in the design.

Inlet Height	$P_i$	Inlet Width	$W_i$
Outlet Height	$P_o$	Outlet Width	$W_o$
Height of the base	$P_b$	Unit Width	$W_u$
Crest height	$P$	Unit Length	$L_u$
Total Lateral Length	$B$	Total developed length	$L$
Outlet Length	$B_o$	Total width of the PKW	$W$
Inlet Length	$B_i$	Wall thickness	$T_s$
Length of the base	$B_b$	Inlet Slope	$S_i$
Number of units	$N_u$	Outlet Slope	$S_o$
Parapet wall height	$P_p$	Parapet wall thickness	$T_p$

**Tab. 2.1 Fundamental parameters on an entire PKW**

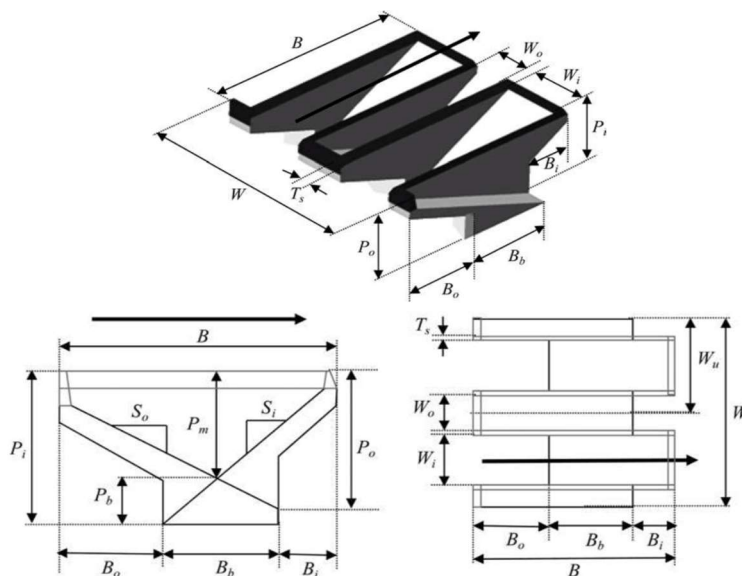


**Fig. 2.5 Fundamental parameters on an entire PKW - 3D view, plan view and cross section**  
(source: Pralong et al. (2011))

Likewise, different types of PKW were defined according to their overhangs: type A has symmetric overhangs, type B has a single upstream overhang, type C has a single downstream overhang and type D does not have overhangs (Figure 2.6). With the goal to understand the hydraulic behaviour and the discharge efficiency of each type, Noui and Ouamane (Noui and Ouamane, 2011) tested 14 different PKW models and revealed that Type B was 9% to 12% more efficient than type A. Lempérière et al. (Lempérière, Vigny and Ouamane, 2011) summarize the efficiency and best implementation for each type:

- Type A has a good efficiency and could be the best solution for raising the water level in existing dams due to the easier self-balanced attribute of the structure.
- Type B appears to be the most hydraulic efficient solution and it could be the best solution for new projects.
- Type C is less efficient than type A and B, thus, seems less interesting except for its implementation as a fusegate.
- Type D could be a solution if there is enough space in banks or rivers.

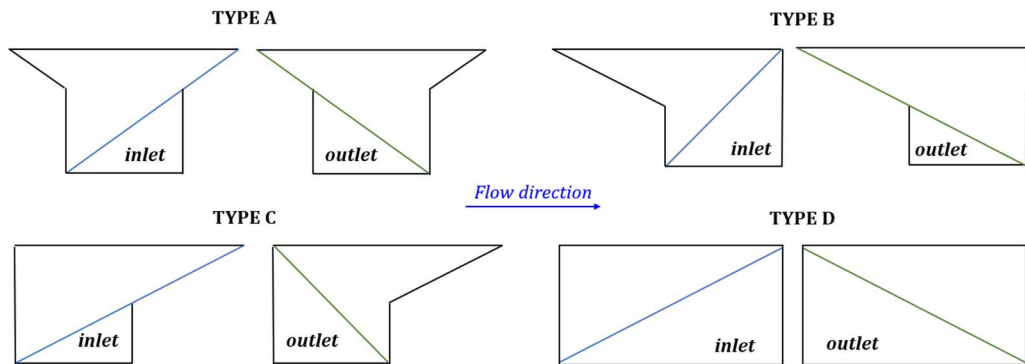


**Fig. 2.6 type A, type B, type C and type D PKWs.**

Furthermore, Cicero (Cicero and J.R. Delisle, 2013) confirmed that the type B was from 5 to 15% more efficient than the type A, which was 15% more efficient than the type C. Nevertheless, Machiels et al. (Machiels, 2012) tested several up- and downstream overhang lengths and found out that for lower heads, the type B configuration is the most efficient, but this efficiency decreases for higher heads,

indeed, for  $H/W_u > 0.3$ , the gain becomes negligible compared to the type A. Therefore, further research may be carried out to prove which PKW type is the most efficient.

PKWs have been also tested as side weirs by Karimi et al. (Karimi *et al.*, 2017, 2018). They tested nine type C PKWs, nine rectangular labyrinth side weirs (RLSW) and three linear side weirs (LSW) under free and submerged flow conditions. The influence area of streamlines of the principal flow driven by the side weir is bigger for PKSW than for RLSW and LSW. This occurs because the deflection angle of the PKW, especially at the bottom, is higher, increasing the outflow discharge. They also found that the PKSW and the RLSW discharge coefficient are higher than the LSW, whereas coefficients of the PKSW and the RLSW are comparable among each other.

Trapezoidal labyrinth weirs revealed that a sidewall angle can improve the discharge capacity, therefore, Trapezoidal PKWs (TPKW) were also studied. In this context, Cicero et al. (Cicero and J.R. Delisle, 2013; Cicero and J. R. Delisle, 2013) analysed two configurations of TPKW, one with the same developed length and the other one with the same inlet and outlet overhangs lengths, and compared them with a Type A rectangular PKW. They concluded that the TPKW was up to 20% more efficient than the rectangular PKW. Likewise, Mehboudi et al. (Mehboudi, Attari and Hosseini, 2016, 2017) observed that the discharge coefficient of the TPKW is about 22% higher than the rectangular PKW. Finally, Safarzadeh and Noroozi (Safarzadeh and Noroozi, 2017) used 3D free surface computational fluid dynamics to carry out a sensitivity analysis of hydrodynamics of a TPKW. They characterized water surface map, streamlines, velocity, fluid depth and Froude number along a rectangular labyrinth weir (RLW), PKW and TPKW with same developed crest lengths. They calculated the specific discharge along the crest and the percentage contribution of the inlet, outlet and side crests. They found out that the TPKW is up to 23% more efficient than a rectangular labyrinth and up to 18% more efficient than a rectangular PKW, achieving a lower efficiency loss at higher heads. Furthermore, the TPKW streamlines supply more uniformly the side crest, creating

fewer contractions that cause a reduction in discharge efficiency. In addition, the TPK geometry increases the inlet flow area, decreasing the inlet velocity and resulting in a better distribution of the inlet velocity.

In addition, Chahartaghi et al. (Karimi Chahartaghi, Nazari and Mahmoodian Shooshtari, 2019) tested the performance of several arced trapezoidal piano key weirs (ATPKW) with different arc angles: 90°, 65°, 50°, and 45°. The discharge coefficient obtained for each arced model was compared with the corresponding linear PKW model. At lower heads, the linear PKW has a better performance but when the H/P ratio starts to increase, the performance of ATPKW is better. Tests revealed that there was not any local submergence and that flow distribution in the ATPKW models was more uniform. The 45° had the best performance, followed by 90°, 65° and 50° respectively.

An alternative solution is the “Papaya spillway”, a combination between a PKW and a morning glory spillway, which is a funnel-shaped outlet that allows water to bypass the dam when it reaches its maximum capacity. This solution was tested by Cicero et al. (Cicero *et al.*, 2011) with a 1/20 scale model of the Bage Dam (France). The results showed that the Papaya spillway is up to 30% more efficient than a classical morning glory and it prevents the creation of vortices, avoiding submergence conditions at higher discharges. Furthermore, Ackers et al. (Ackers *et al.*, 2013) raised the morning glory spillway located in the Black Esk reservoir (Edinburgh) using the papaya spillway, resulting in a 24-cycle PKW with equal 15° sectors constructed using precast concrete units (Figure 2.7).



**Fig. 2.7 Papaya PKW at the Black Esk reservoir** (source: [www.moore-concrete.com](http://www.moore-concrete.com))

The good results obtained from testing several modified PKWs proves the reliable performance of the PKW structure, opening the possibility to further alter the classical PKW geometry.

### **2.2.2 PKW optimal design**

In order to understand the hydraulic behaviour of PKWs, aiming to improve their discharge capacity, many experimental and numerical studies have been performed focusing on which parameters mainly affect the discharge efficiency.

The PKW height has a major impact on the discharge capacity and by increasing it, the PKW performance improves, especially at lower heads (Leite Ribeiro *et al.*, 2011; Noui and Ouamane, 2011; Pralong, Montarros, *et al.*, 2011; Machiels, Erpicum and Piroton, 2012). The increasing efficiency is caused by the inlet key section area enlargement that reduces velocity and hydraulic loss. Additionally, the outlet key slope is steeper improving the flow evacuation and reducing the local submergence in the outlet key (Lefebvre, Vermeulen and Blancher, 2013).

Another way of increasing the inlet key section is by increasing the inlet width,  $W_i$ . The  $W_i/W_o$  ratio should be over 1 to improve the discharge capacity. Nonetheless, increasing the inlet key means a decrease of the outlet key, resulting in an increase of the local submergence, by overfilling the outlet key and decreasing

the discharge efficiency. For that reason, an optimal value for  $W_i/W_o$  ratio can be set between 1.25 and 1.5 (Leite Ribeiro *et al.*, 2011; Machiels *et al.*, 2011; Pralong, Montarros, *et al.*, 2011; Machiels, Erpicum and Piroton, 2012; Lefebvre, Vermeulen and Blancher, 2013; Olivier Machiels *et al.*, 2014).

Overhangs are the biggest difference between a PKW and a labyrinth weir and influence the discharge efficiency because they are related to the developed length and the inlet section.  $Bo/Bi$  ratios lower than 1 reduce the discharge capacity whereas extending the upstream overhang ( $Bo/Bi > 1$ ) increases the inlet cross section, avoiding flow contraction, reducing velocities, thus, energy loss. Moreover, it influences the discharge over the side crest, by improving the discharge efficiency of the PKW. However, increasing the upstream overhang decreases the outlet key slope and cross section, causing a more rapid filling of the outlet as well as the submergence of the lateral crest by the outlet flow, ultimately reducing the discharge efficiency. The upstream overhang effect could explain why type B PKWs seem to be more efficient. Nonetheless, type B PKWs appear to be more appropriate for higher PKWs because enable higher outlet key slopes, helping to avoid subcritical outlet flow that reduces the efficient length of the side crest, whereas type A PKWs appear more effective for lower configurations. Therefore, the optimum  $Bo$  value would be achieved implementing the longest upstream overhang that avoids an outlet key slope under the critical one (Pralong, Montarros, *et al.*, 2011; R. M. Anderson and Tullis, 2011; Machiels, Erpicum and Piroton, 2012; Machiels *et al.*, 2014).

Regarding the sidewall thickness, this parameter influences both inlet and outlet cross-sections. Increasing the wall thickness means a decrease in the discharge efficiency, especially for lower heads. Consequently, thinner sidewalls are preferred, however, this thickness is limited from a structural viewpoint so both the effective thickness should be thus optimized, in compliance with the structural constraints of the design (Laugier, Pralong and Blancher, 2011; Bremer and Oertel, 2017).

Crest shape can also have an influence on the discharge efficiency. Anderson and Tullis (R.M. Anderson and Tullis, 2011) tested flat-topped and half-rounded crests

---

on a laboratory-scaled model and concluded that half-rounded improves the discharge efficiency especially at lower heads. Cicero and Delisle (Cicero and Delisle, 2014) and Cicero (Cicero, Vermeulen and Laugier, 2016) tested a type A PKW with flat-topped, half-rounded and quarter-rounded crests. They remarked that the lateral crest has a big influence of the crest shape while the shape of the up- and downstream crest has negligible effects. Also, the half-round and quarter-round, wherever the rounded face is positioned (in the inlet or the outlet), have better performance than the flat-top shape with a gain of up to 25%, however, this influence decreases to 5% with higher upstream heads ( $H/P > 0.4$ ).

Parapet walls can be placed on the crest of the PKW either to heighten the structure or to modify the inlet and outlet keys slopes, keeping the global height,  $P$ , constant. As seen in Machiels et al. (Machiels, 2012; Olivier Machiels *et al.*, 2014), the discharge capacity does not increase when a parapet wall is placed on a PKW that has an already optimal weir height and the discharge capacity is the same if the optimum height of the PKW is achieved with or without parapet walls. Also, the height of the parapet wall must be limited to keep the interest of using overhang use, otherwise the weir becomes more similar to a labyrinth weir, decreasing the efficiency. Likewise, it is more economical and convenient from a construction viewpoint to achieve this height without parapet walls. Nonetheless, parapet walls could be useful in the future to increase the capacity on reservoirs, however, the efficiency of the resulting PKW would decrease as the maximum upstream level would remain the same.

### **2.2.3 Analytical equations to predict discharge coefficients of PKWs.**

With the aim of providing effective analytic formulations able to predict the discharge capacity of PKWs, several researchers have developed equations using two different approaches: a specific discharge coefficient derived from the Poleni's equation or a discharge enhancement ratio which compares the PKW discharge with a sharp-crested weir discharge. Herein, several design equations are presented

to predict the discharge capacity of a PKW, achieved by using data from experimental models or from computational simulations.

### 2.2.3.1 Leite Ribeiro et al. equation

Leite Ribeiro et al. (Ribeiro *et al.*, 2012) proposed an empirical formulation to estimate the discharge augmentation ratio between the PKW discharge and that of a rectangular sharp-crested weir with the same width,  $r = Q_{PKW}/Q_W$ , where  $Q_{PKW}$  is the discharge of the PKW [ $m^3s^{-1}$ ] and  $Q_W$  is the discharge of a rectangular sharp-crested weir [ $m^3s^{-1}$ ]. Their analysis identified primary parameters such as relative developed crest length,  $L$ , and upstream head,  $H$ , that have a significant effect on the discharge. Likewise, they identified secondary parameters, which have a smaller influence, such as the inlet- outlet key widths ratio,  $W_i$  and  $W_o$ , the inlet-outlet key heights,  $P_i$  and  $P_o$ , the inlet-outlet overhang lengths,  $B_i$  and  $B_o$ , and the relative height of the parapet walls,  $R_o$ . The ratio can be calculated as:

$$r = 1 + 0.24\delta(wp b_{LR} a) \quad (2.3)$$

where  $\delta$  is a parameter that includes the geometric parameters mainly affecting the PKW discharge efficiency:

$$\delta = \left( \frac{(L - W)P_i}{WH} \right)^{0.9} \quad (2.4)$$

where  $L$  is the developed length of the weir [m],  $W$  is the width of the weir [m],  $P_i$  is the inlet key height [m], and  $H$  is the upstream head [m] and  $w$ ,  $p$ ,  $b$  and  $a$  are correction factors related to secondary effects. The former factor,  $w$ , is related to the  $W_i/W_o$  ratio:

$$w = \left( \frac{W_i}{W_o} \right)^{0.05} \quad (2.5)$$

where  $W_i$  is the inlet key width [m] and  $W_o$  is the outlet key width of the weir [m]. The second correction factor,  $p$ , is related to  $P_o/P_i$  ratio:

$$p = \left( \frac{P_o}{P_i} \right)^{0.25} \quad (2.6)$$

where  $P_o$  is the outlet key height [m] and  $P_i$  is the inlet key height of the weir [m].

The effects of the overhang lengths  $B_o$  and  $B_i$  are estimated by the  $b$  factor:

$$b_{LR} = \left(0.3 + \frac{B_o + B_i}{B}\right)^{-0.50} \quad (2.7)$$

where  $B_o$  is the upstream overhang length [m] and  $B_i$  is the downstream overhang length [m]. Likewise, parapet walls increase the discharge capacity, so this analysis includes a fourth correction factor:

$$a = 1 + \left(\frac{R_o}{P_o}\right)^2 \quad (2.8)$$

where  $R_o$  is the height of the parapet wall of the outlet key [m].

These equations are based on a physical model which represents a sectional channel set-up, neglecting the distal effect occurring, for instance, on a reservoir. For linear standard weirs, the effective width is usually reduced to predict an accurate discharge. To consider this effect for PKWs, the effective width may be reduced, including a reduction factor  $\xi$ :

$$Q_{PKW} = \xi r Q_W \quad (2.9)$$

where

$$\xi = 1 - \left(\frac{1.5W_o}{W}\right) \quad (2.10)$$

The range tested in this research limits the applicability of these equations to:  $0.1 \leq H/P \leq 2.8$ ,  $3.0 \leq L/W \leq 7.0$ ,  $1.5 \leq B/P \leq 4.6$ ,  $0.5 \leq W_i/W_o \leq 2.0$ ,  $0.2 \leq B_i/B \leq 0.4$ ,  $0 \leq R_o/P_o \leq 0.22$  and therefore, to  $0 < \delta < 20$ ,  $0.97 \leq w \leq 1.04$ ,  $0.92 \leq p \leq 1.08$ ,  $0.95 \leq b_{LR} \leq 1.20$  and  $1 \leq a \leq 1.05$ .

Results from physical model tests, conducted at the Laboratory of Hydraulic Constructions (LCH) of Ecole Polytechnique Fédérale de Lausanne, were used to validate the equations. The coefficient of determination between the measured values and the prediction according to Eq. (2.3) is  $R^2 = 0.976$ . Furthermore, maximum errors of +18 and -11% occurred between measured and computed values of  $r$ . The NRMSD (Normalized Residual Mean Square Difference) between measured and computed values is 0.018.

### 2.2.3.2 Kabiri-Samani and Javaheri equation

Kabiri-Samani and Javaheri (Kabiri-Samani and Javaheri, 2012) investigated several geometrical parameters to develop a dimensionless analytic ratio of the discharge coefficient. They applied dimensional analysis, developing a trial-and-error procedure coupled with a mathematical software, to calibrate the experimental observations.

The discharge coefficient for free flow, when the downstream/upstream head ratio,  $H_d/H \leq 0.6$ , is calculated as:

$$C_D = 0.212 \left(\frac{H}{P}\right)^{-0.675} \left(\frac{L}{W}\right)^{0.377} \left(\frac{W_i}{W_o}\right)^{0.426} \left(\frac{B}{P}\right)^{0.306} \times \exp\left(1.504 \frac{B_o}{B} + 0.093 \frac{B_i}{B}\right) + 0.606 \quad (2.11)$$

where  $P$  is the height of the weir [m] and  $B$  is the lateral crest length [m]. This equation is subject to the following constraints:  $H > 30$  mm,  $0.1 \leq H/P \leq 0.6$ ,  $2.5 \leq L/W \leq 7$ ,  $1 \leq B/P \leq 2.5$ ,  $0.33 \leq W_i/W_o \leq 1.22$ ,  $0 \leq B_i/B \leq 0.26$ ,  $0 \leq B_o/B \leq 0.26$ .

The discharge coefficient for submerged flow is calculated as:

$$C_S = \left(1 - 0.858 \left(\frac{H_d}{H}\right) + 2.628 \left(\frac{H_d}{H}\right)^2 - 2.489 \left(\frac{H_d}{H}\right)^3\right) \times \left(\frac{L}{W}\right)^{0.055} \quad (2.12)$$

subject to the following constraints:  $2.5 \leq L/W \leq 6$ ,  $1 \leq B/P \leq 2.5$ ,  $0.33 \leq W_i/W_o \leq 1.22$ ,  $0 \leq B_o/B \leq 0.26$ ,  $0 \leq B_i/B \leq 0.26$  and  $H_d/H > 0.6$ .

Results from physical model test were compared to those obtained with the presented equations. The NRMSE was equal to 0.077 and  $R^2 = 0.986$  for free flow and NRMSE = 0.122 and  $R^2=0.97$  for submerged flow conditions.

### 2.2.3.3 Machiels et al. equation

Machiels et al. (Machiels et al., 2014) combined many results from experimental tests and presented an analytical approach. They divided the discharge into three parts, according to the PKW geometry: the discharge passing over the upstream crest of the outlet, the discharge passing over the downstream part of the inlet and the one passing over the lateral crests in-between the inlet and the outlet. The specific discharge of the PKW is thus calculated as:

$$q = q_{UC} \frac{W_o}{W_u} + q_{DC} \frac{W_i}{W_u} + q_{LC} \frac{2B}{W_u} \quad (2.13)$$

where  $q_{UC}$  is the discharge over the upstream crest [ $m^3s^{-1}m^{-1}$ ],  $q_{DC}$  is the discharge over the downstream crest [ $m^3s^{-1}m^{-1}$ ], and  $q_{LC}$  is the discharge passing over the lateral crests [ $m^3s^{-1}m^{-1}$ ]. These three discharges can be calculated as:

$$q_{UC} = 0.374 \left(1 + \frac{1}{1000H + 1.6}\right) \left(1 + 0.5 \left(\frac{H}{H + P}\right)^2\right) \sqrt{2gH^3} \quad (2.14)$$

$$q_{DC} = 0.445 \left(1 + \frac{1}{1000H + 1.6}\right) \left(1 + 0.5 \left(\frac{H}{H + P_i}\right)^2\right) \sqrt{2gH^3} \quad (2.15)$$

$$q_{LC} = 0.410 \left(1 + \frac{1}{833H + 1.6}\right) \left(1 + 0.5 \left(\frac{0.833H}{0.833H + P_e}\right)^2\right) \left(\frac{P_e^\alpha + \beta}{(0.833 + P_e)^\alpha + \beta}\right) K_{W_i} K_{W_o} \sqrt{2gH^3} \quad (2.16)$$

The corrective coefficients guarantee that the lateral discharge corresponds to the discharge of a sharp-crested weir when the head tends to 0 and that the lateral discharge became negligible when head tends to infinity. The  $\alpha$  and  $\beta$  parameters depend on the inlet key slope and can be calculated as:

$$\alpha = \frac{0.7}{S_i^2} - \frac{3.58}{S_i} + 7.55 \quad (2.17)$$

$$\beta = 0.029e^{-\frac{1.446}{S_i}} \quad (2.18)$$

$P_e$  is the mean lateral crest height and is calculated as:

$$P_e = P \frac{B_o}{B} + P_i \frac{1 - \frac{B_o}{B}}{2} \quad (2.19)$$

$K_{W_i}$  considers the effect of the inlet key width on the side crest efficiency:

$$K_{W_i} = 1 - \frac{\gamma^*}{\gamma^* + W_i^2} \quad (2.20)$$

where

$$\gamma^* = 0.0037 \left(1 - \frac{W_i}{W_o}\right) \quad (2.21)$$

and  $K_{W_o}$  considers the reduction of the effective side crest length because of the local submergence induced by the outlet key:

---

$$K_{W_o} = 1 \quad \text{for } \frac{H}{W_o} \leq \delta_1 \quad (2.22)$$

$$K_{W_o} = \frac{2}{(\delta_2 - \delta_1)^3} \left( \frac{H}{W_o} \right)^3 - \frac{3(\delta_2 + \delta_1)}{(\delta_2 - \delta_1)^3} \left( \frac{H}{W_o} \right)^2 + \frac{6\delta_2\delta_1}{(\delta_2 - \delta_1)^3} \frac{H}{W_o} + \frac{\delta_2^2(\delta_2 - 3\delta_1)}{(\delta_2 - \delta_1)^3} \quad \text{for } \delta_1 < \frac{H}{W_o} < \delta_2 \quad (2.23)$$

$$K_{W_o} = 0 \quad \text{for } \frac{H}{W_o} \geq \delta_2 \quad (2.24)$$

where

$$\delta_1 = -0.788S_o^{-1.88} + 5 \quad (2.25)$$

$$\delta_2 = 0.236S_o^{-1.94} + 5 \quad (2.26)$$

The application domain for these equations is limited by:  $0.1 \leq H/P \leq 5.0$ ,  $4.2 \leq L/W \leq 5.0$ ,  $1.0 \leq B/P \leq 6.0$ ,  $0.50 \leq W_i/W_o \leq 2.0$  and  $0.29 \leq B_i/B \leq 0.33$ .

The comparison between the measured values from experimental results and computed values of the final analytical formulation resulted in a  $R^2 = 0.982$ .

#### 2.2.3.4 Hu et al. equation

Hu et al. (Hu et al., 2018) simulated three-dimensional flow fields in PKWs using the Volume of Fluid (VoF) model and presented an analytical approach, also divided in three discharges corresponding to the upstream, downstream and lateral crests. The upstream crest discharge is calculated as:

$$q_{UC} = K_u \left( 0.405 + \frac{0.003}{H} \right) \left( 1 + 0.55 \left( \frac{H}{H+P} \right)^2 \right) \sqrt{2gH^3} \quad (2.27)$$

where  $K_u$  is a coefficient obtained from simulations of several PKW structures and geometries and comes from the value of  $q_{UC}/q_{sharp-crested}$  and is equal to  $K_u = 0.932$ .

The downstream discharge can be calculated as:

$$q_{DC} = K_i K_d \left( 0.405 + \frac{0.003}{H} \right) \left( 1 + 0.55 \left( \frac{H}{H+P} \right)^2 \right) \sqrt{2gH^3} \quad (2.28)$$

where  $K_i$  and  $K_d$  are defined as:

$$K_i = 1 + \frac{0.3902 \arctan\left(\frac{B - B_o}{P}\right)}{\pi} \quad (2.29)$$

$$K_d = 1 - \frac{0.577 \left(\frac{H}{W_u}\right)^{0.962}}{\left(\frac{P}{W_u}\right)^{e^*} + 0.808 \left(\frac{H}{W_u}\right)^{0.858}} \quad (2.30)$$

where:

$$e^* = -3.343 \left(\frac{H}{W_u}\right)^2 + 1.518 \left(\frac{H}{W_u}\right) + 3.578 \quad (2.31)$$

Finally, the side crest discharge is defined as:

$$q_{LC} = K_s K_W \left(0.405 + \frac{0.003}{H}\right) \left(1 + 0.55 \left(\frac{H}{H + P_e^*}\right)^2\right) \sqrt{2gH^3} \quad (2.32)$$

where  $P_e$  is the mean height of the side weir and is expressed as:

$$P_e^* = \frac{B_o}{B} P_T + \left(1 - \frac{B_o}{B}\right) \frac{P}{2} \quad (2.33)$$

and  $K_W$  and  $K_s$  can be calculated as:

$$K_W = -0.238 \left(\frac{W_i}{W_o}\right)^2 + 0.668 \left(\frac{W_i}{W_o}\right) + 0.57 \quad (2.34)$$

$$K_s = \frac{a^*}{\left(\frac{H}{W_u}\right)^{1.906} + a^*} \quad (2.35)$$

with

$$a^* = -0.597 \left(\frac{P}{B}\right)^2 + 0.947 \left(\frac{P}{B}\right) - 0.1 \quad (2.36)$$

To validate the equations, the calculation results were compared with Lempérière's experimental results (Lempérière and Ouamane, 2003). The maximum relative error and the average relative error were 6.7% and 3.7%, respectively. Additionally, the calculation results of Kabiri-Samani's (Kabiri-Samani and Javaheri, 2012) formula and Machiels' formula (Machiels *et al.*, 2014) were compared with those obtained with Hu *et al.* (Hu *et al.*, 2018). The maximum relative error and the average relative error of Samani's formula were 23.6% and 11.9% respectively; and the maximum relative error and the average relative error of Machiels' formula were 16.3% and 10.1%.

---

### 2.2.3.5 Guo *et al.* equation

Guo *et al.* (Guo *et al.*, 2019) also developed a dimensionless analytic ratio of the discharge coefficient. They investigated the main geometrical parameters affecting the discharge capacity, such as the length, horizontal width of the weir, vertical height, widths of the inlet and outlet keys, crest length and the weir head. By analysing the existing experimental data of the PKW and calibrating the coefficients through an optimization procedure of meta-heuristic algorithm, they derived an analytical equation where the side wall thickness, the height of the parapet on the weir, and the parapet shape are secondary factors, not included in the assessment. Therefore, the discharge coefficient can be computed as:

$$C_D = 0.1 + 0.285 \left(\frac{L}{W}\right)^{0.45} \left(\frac{B}{P}\right)^{0.1} \left(\frac{W_i}{W_o}\right)^{0.05} \left(\frac{H}{P}\right)^{-0.465} \quad (2.37)$$

with an application domain of  $H/P > 0.1$ ,  $2.5 < L/W < 8.5$ ,  $0 < W_i/W_o < 2.45$ , and  $1 < B/P < 6$ .

Analysis results showed that the values predicted by the proposed formula were in good agreement with the published test data from Kabiri-Samani and Javaheri (Kabiri-Samani and Javaheri, 2012), Leite Ribeiro *et al.* (Ribeiro *et al.*, 2012) and Machiels *et al.* (Machiels, 2012; Machiels *et al.*, 2014) with an average error in the range of 5–8% if the head ratio  $H/P > 0.15$  PKW.

## 2.2.4 PKW velocity, surface profile and nappe behaviour

Machiels *et al.* (Machiels, 2012; Machiels, Erpicum and Piroton, 2012) defined the nappe behaviour at different  $H/P$  ratios. Regarding the downstream and lateral crests, for low heads ( $H/P = 0.05$ ), the leaping nappe remains in contact with the crest. For  $0.09 \leq H/P \leq 0.10$ , the nappe starts springing free and is detached from the crest along the downstream crest portion and on the downstream inlet crest. For  $0.11 \leq H/P \leq 0.12$  the transition from leaping to springing nappe occurs. Nonetheless, at the upstream crest, for the lowest head ratios, the nappe is completely attached to the walls, while for  $0.16 \leq H/P \leq 0.17$  the nappe is fully aerated. In terms of streamlines, the distribution is regular for low heads ( $H/P \leq$

0.2). The downstream inlet crest is mainly supplied by the bottom current, the upstream outlet crest is supplied by the surface current and the lateral crest is supplied by the outlet and inlet current. For  $H > 0.2$ , the streamlines distribution is less regular. The upstream crest is still supplied by the surface stream, the downstream crest is supplied by the bottom stream, but also by surface stream and the side crest is overall badly supplied. This stream transition corresponds to the change from flat ( $H/P=0.1$ ) to undular ( $H/P=0.35$ ) free surface profile along the inlet key. In terms of velocity, the velocity profiles for  $H/P < 0.2$  are quite uniform along the side wall and the inlet centre. For higher head, the velocity increases along the inlet centre, with higher values towards downstream.

### **2.2.5 PKW in rivers**

The location of PKWs in rivers allows increasing the water level for river hydropower plants (Eichenberger, 2014). This involves installing a weir able to maintain a fixed water level, with high discharge capacity that helps to avoid floods caused by overtopping of the banks in usually high populated places. Nonetheless, the possible blocking of the PKW with driftwood may be taken into consideration along with the necessity of an effective sediment passage over the weir.

One of the flow characteristics of PKWs is that when the upstream flow approaches the weir, a velocity component in the z-direction emerges. This behaviour was observed by Sharma and Tiwari (Sharma and Tiwari, 2014) and they concluded that this z-component velocity was enough to uplift sediments up to 2 mm of diameter. Furthermore, for higher head this component increases leading to a PKW with the capacity of flushing sediments. Noseda et al. (Noseda *et al.*, 2019) studied with a physical model the sediment passage over the PKW using three different geometries, two sediment granulometries and six different discharges. They observed that a mobile bed creates an upstream front-scour while a fixed bed prevents this to happen, although the rating curve of the combined mobile bed with the front-scour is more efficient. They also observed sediment passage in all tests with a densimetric Froude number  $F_d > 1.3$  with initially a filled inlet key that

empties after with  $F_d > 1.7$ . Likewise, they noted that values of  $F_d > 2.5$  could result in an important upstream front-scour.

However, sediment transport can incur scouring events that may disrupt the PKW. Pfister et al. (Pfister, Jüstrich and Schleiss, 2017) tested several scenarios: a natural sediment bed; a natural and coarse sediment bed; a pre-excavated plunge pool protected with riprap. The obtained values are were too high to be acceptable, so a fixed bed (protected with riprap) could be recommended because no scour was observed on these cases. Lastly, they also observed that the tailwater flow velocity is enough to start sediment transport, though for the coarse sediment a ridge up appears.

Besides sediment transportation, driftwood can be carried by the river during flood events, and it should be taken into consideration when the PKWs are planned to be located on a river. Driftwood can be stuck near the PKW, thus decreasing the discharge capacity and increasing the water depth upstream the weir. Based on this, Pfister et al. (Pfister, Schleiss and Tullis, 2014) carried out several laboratory-scale tests using different PKW geometries located in reservoir and varying the size of driftwood trunks which are typically found in Alpine and pre-Alpine catchments. After testing every case with different specific discharges, results showed that the volume of driftwood blocked increases when the unit discharge decreases and when the supplied driftwood volume increases. Although, in some cases the latter incorporated driftwood in addition to the higher upstream head allowed the PKW to wash some trunks, thus the probability of washed driftwood increases at increasing the unit discharge. It was also observed that the trunks were orientated parallel to the flow until be blocked where they were oriented parallel to the PKW axis. Finally, they noted that the discharge coefficient decreases to the driftwood collected at the PKW.

### **2.2.6 Scale effects in PKW physical models**

Despite the progress on numerical data simulation, physical models have been always the basic tool for engineers to optimize and improve hydraulic complex

---

structures. These physical models should be based on geometric, kinematic (flow patterns) and dynamic (same force ratios) similitude. Geometric similitude can be achieved by reproducing the structure and flow domain at different size scales. Dynamic similitude can be achieved by respecting the scale ratios for all the relevant forces, such as gravity and inertia forces related to free-surface flow similitude (Froude similitude), viscous forces (Reynolds similitude) and surface tension (Weber similitude). Nevertheless, it is impossible to keep a dynamic similitude (gravity, viscous and surface tension) when the same fluid is used in model and prototype, thus, the data from a model based on Froude scaling similitude should be limited to certain flow conditions.

With the purpose of understanding the influence of surface tension and viscous effects on PKW Froude-scale modelling, several studies have been carried out to find the minimum values of the upstream head above which these effects can be considered negligible. For instance, Cicero et al. (Cicero, Menon and Luck, 2011) created two scale models of 1/30 and 1/60 of the Malarce Dam (France). The discharge coefficients measured on both models were comparable. At very low heads ( $H/P < 0.1$ ) a peak on the discharge coefficient appeared. For higher heads the rating curves are not influenced by the upstream water level, so the scale effects become negligible. The results of both models are close when the head is larger than 0.015m and the Weber number is bigger than 30. Pfister et al. (Pfister *et al.*, 2014) combined several simulations with an analytical approach to derive the minimal heads on round crested PKWs. They concluded that for small heads, the flow over the rounded? crest is dominated by the crest shape when  $H/R < 2$ , with R being the radius of the rounded crest [m]. The inception of flow is observed for values of H of 4mm and 5mm. The limit for avoiding surface tension and viscous forces is a limiting head of  $H=0.03\text{m}$  for  $0.005\text{ m} \leq R \leq 0.3\text{ m}$ . Likewise, Erpicum et al. (Erpicum *et al.*, 2016) tested three scale models (1:7, 1:15 and 1:25) of the PKW geometry of the Escouloubre Dam (France). Surface tension effects increase when the head decreases because the water is not able to overcome the weir crest initially, thus, the scale effects were more significant in the 1:25 model. They observed that the scaled physical model underestimates the discharge

capacity of the prototype. Moreover, scale effects can also affect nappe behaviour in the scaled models. In free surface flow, surface tensions maintain the air-water interface and, as flow turbulence increases, this interface becomes more irregular, leading to air entrainment and aerated nappe flow. Also, the volume of air cavity located between the nappe and the downstream wall depends on the air entrance, so if the nappe aeration also decreases the air cavity does, increasing the negative pressures that cause the nappe trajectory to reduce. Therefore, they concluded that a minimum upstream head of 0.03 m is required to avoid scale effects due to viscous and surface tension. Correspondently, the minimum Weber number is 54. If a geometrically similar nappe trajectory is necessary, the minimum head of 0.06 m would be required.

### **2.2.7 PKW numerical modelling**

In order to assess how geometric parameters influence the discharge and to estimate the discharge coefficient, two design approaches are usually combined: analytical equations and CFD modelling.

Physical modelling is appreciated to determine the discharge capacity of specific projects and provides the possibility to gather a lot of information in a short period of time. However, laboratory set-ups need relevant economic and time-consuming efforts and results are limited to the installation constraints. On the contrary, CFD models are more affordable, faster to implement and modify but simulation time is usually quite extensive, requiring several days to obtain one data set. Moreover, numerical modelling requires experimental data to calibrate and validate the CFD obtained results, thus, coupling empirical and CFD models seems the optimal solution for collecting a wider range of data.

Some authors mentioned in previous sections appliedd CFD models in order to test new PKW geometries (Blancher, Montarros and Laugier, 2011; Ackers *et al.*, 2013; Safarzadeh and Noroozi, 2017), obtain data to assess the impact of several parameters (Pralong, Montarros, *et al.*, 2011; Lefebvre, Vermeulen and Blancher, 2013; Bremer and Oertel, 2017) or to develop analytical equation to predict the discharge coefficient (Hu *et al.*, 2018). Likewise, specific research has been done

regarding the development of CFD models for PKWs. As several turbulence models are available in CFD, Crookston (Crookston, Anderson and Tullis, 2018) analysed the influence of Large Eddy Simulation (LES) and Re-Normalization Group (RNG) k-epsilon turbulence models on solution results. LES and RNG k-epsilon were observed to provide comparable scatters, but RNG k-epsilon model required lower computational efforts. Similar convergence results were found, thus the additional LES-specific grid refinement resulted to be unnecessary. Therefore, both models were suitable for estimating the discharge coefficient of PKW with relative scatters in the order of 3-4%. This was confirmed by Pralong et al. (Pralong, Montarros, *et al.*, 2011) research wherein the authors tested several turbulence models and found out that there is no influence of the turbulence model on the results.

At the same time, the quality and accuracy of model simulations are strictly related to the mesh geometry and resolution, indeed the mesh convergence is an essential parameter to achieve reliable numerical results (Celik *et al.*, 2008). Bremer and Oertel (Bremer and Oertel, 2018) investigated the allowable maximum mesh sizes applying the Grid Convergence Index Method (GCI) as a sensitivity analysis on mesh quality and independency. They implemented a PKW in CFD and measured the velocity magnitude at a distance of 5P upstream the PKW for different flowrates values. They tested 3 meshes: a coarsest mesh of  $\sim 7\%P$ , a medium one of  $\sim 3.3\%P$  and a finest one of  $\sim 1.67\%P$ . The results showed that general flow patterns can be reasonable reproduced with large mesh sizes ( $\sim 7\%P$ ) whereas obtaining a precise velocity magnitude required a mesh refinement. The velocity comparison between mesh sizes of  $\sim 3.3\%P$  and  $\sim 1.67\%P$  showed a maximum difference value of  $\sim 16\%$ , the smallest mesh could be not enough leading towards the implementation of a thinner mesh.

## References

- Ackers, J.C. et al. (2013) “Raising the bellmouth spillway at black esk reservoir using piano key weirs,” in *Labyrinth and Piano Key Weirs II*. doi:10.1201/b15985.
- Anderson, R. M. and Tullis, B.P. (2011) “Influence of piano key weir geometry on discharge,” *Labyrinth and Piano Key Weirs - Proceedings of the International Conference on Labyrinth and Piano Key Weirs, PKW 2011*, pp. 75–80. doi:10.1201/b12349-12.
- Anderson, R.M. and Tullis, B.P. (2011) “Influence of Piano Key Weir geometry on discharge,” in *Labyrinth and Piano Key Weirs – PKW 2011*, pp. 75–80.
- Blancher, B., Montarros, F. and Laugier, F. (2011) “Hydraulic comparison between piano key weirs and labyrinth spillways,” in *Labyrinth and Piano Key Weirs - Proceedings of the International Conference on Labyrinth and Piano Key Weirs, PKW 2011*. doi:10.1201/b12349-22.
- Bremer, F. and Oertel, M. (2017) “Numerical investigation of wall thickness influence on Piano Key Weir discharge coefficients: A preliminary study,” in *Labyrinth and Piano Key Weirs III – PKW 2017*. doi:10.1201/9781315169064-14.
- Bremer, F.L. and Oertel, M. (2018) “Numerical uncertainty of piano key weir discharge coefficient estimations by means of 3D CFD modelling - A preliminary study,” in *7th IAHR International Symposium on Hydraulic Structures, ISHS 2018*. doi:10.15142/T39W7R.
- Celik, I.B. et al. (2008) “Procedure for estimation and reporting of uncertainty due to discretization in CFD applications,” *Journal of Fluids Engineering, Transactions of the ASME*, 130(7), pp. 0780011–0780014. doi:10.1115/1.2960953.
- Cicero, G.M. et al. (2011) “Study of a piano-key morning glory to increase the spillway capacity of the Bage dam,” in *Labyrinth and Piano Key Weirs - Proceedings of the International Conference on Labyrinth and Piano Key Weirs, PKW 2011*. doi:10.1201/b12349-13.

- Cicero, G.M. and Delisle, J.R. (2013) “Discharge characteristics of Piano Key weirs under submerged flow,” in *Labyrinth and Piano Key Weirs II – PKW 2013*, pp. 101–109.
- Cicero, G.M. and Delisle, J. R. (2013) “Experimental and numerical study of the hydraulic performance of a trapezoidal piano key weir,” in *Labyrinth and Piano Key Weirs II*. doi:10.1201/b15985.
- Cicero, G.M. and Delisle, J.R. (2014) “Effects of the crest shape on the discharge efficiency of a type A Piano Key weir,” in *Labyrinth and Piano Key Weirs II – PKW 2013*. Taylor & Francis Group, pp. 41–48.
- Cicero, G.M., Menon, J.M. and Luck, M. (2011) “Experimental study of side and scale effects on hydraulic performances of a Piano Key Weir,” in *Labyrinth and Piano Key Weirs – PKW 2011*, pp. 167–174.
- Cicero, G.M., Vermeulen, J. and Laugier, F. (2016) “Influence of some geometrical parameters on Piano Key Weir discharge efficiency,” in *6th International Symposium on Hydraulic Structures: Hydraulic Structures and Water System Management, ISHS 2016*. doi:10.15142/T3320628160853.
- Crookston, B.M., Anderson, R.M. and Tullis, B.P. (2018) “Free-flow discharge estimation method for Piano Key weir geometries,” *Journal of Hydro-Environment Research* [Preprint]. doi:10.1016/j.jher.2017.10.003.
- Eichenberger, P. (2014) “The first commercial Piano Key Weir in Switzerland,” in *Labyrinth and Piano Key Weirs II - PKW 2013*, pp. 227–234.
- Erpicum, S. et al. (2016) “Scale effects in physical piano key weirs models,” *Journal of Hydraulic Research*. Taylor and Francis Ltd., pp. 692–698. doi:10.1080/00221686.2016.1211562.
- Guo, X. et al. (2019) “Discharge capacity evaluation and hydraulic design of a piano key weir,” *Water Science and Technology: Water Supply* [Preprint]. doi:10.2166/ws.2018.134.

- Hu, H. et al. (2018) “Numerical study of characteristics and discharge capacity of piano key weirs,” *Flow Measurement and Instrumentation* [Preprint]. doi:10.1016/j.flowmeasinst.2018.05.004.
- Johnson, M.C. (2000) “Discharge coefficient analysis for flat-topped and sharp-crested weirs,” *Irrigation science*, 19(3), pp. 133–137.
- Kabiri-Samani, A. and Javaheri, A. (2012) “Discharge coefficients for free and submerged flow over Piano Key weirs,” *Journal of Hydraulic Research* [Preprint]. doi:10.1080/00221686.2011.647888.
- Karimi Chahartaghi, M., Nazari, S. and Mahmoodian Shooshtari, M. (2019) “Experimental and numerical simulation of arced trapezoidal piano key weirs,” *Flow Measurement and Instrumentation* [Preprint]. doi:10.1016/j.flowmeasinst.2019.101576.
- Karimi, M. et al. (2017) “Experimental study of discharge coefficient of a Piano Key Side Weir,” in *Labyrinth and Piano Key Weirs III – PKW 2017*. doi:10.1201/9781315169064-15.
- Karimi, M. et al. (2018) “Side weir flow characteristics: Comparison of piano key, labyrinth, and linear types,” *Journal of Hydraulic Engineering* [Preprint]. doi:10.1061/(ASCE)HY.1943-7900.0001539.
- Khassaf, S.I. and Al-Baghdadi, M.B. (2015) *INTERNATIONAL JOURNAL OF ENERGY AND ENVIRONMENT* Experimental study of non-rectangular piano key weir discharge coefficient, *Journal homepage: www.IJEE.IEEFoundation.org* ISSN. Online. Available at: [www.IJEE.IEEFoundation.org](http://www.IJEE.IEEFoundation.org).
- Laugier, F., Pralong, J. and Blancher, B. (2011) “Influence of structural thickness of sidewalls on PKW spillway discharge capacity,” in *Labyrinth and Piano Key Weirs - Proceedings of the International Conference on Labyrinth and Piano Key Weirs, PKW 2011*. doi:10.1201/b12349-24.
- Lefebvre, V., Vermeulen, J. and Blancher, B. (2013) “Influence of geometrical parameters on pk-weirs discharge with 3d numerical analysis,” in *Labyrinth and Piano Key Weirs II*. doi:10.1201/b15985.

- Leite Ribeiro, M. et al. (2011) “Experimental parametric study for hydraulic design of PKWs,” in Labyrinth and Piano Key Weirs - Proceedings of the International Conference on Labyrinth and Piano Key Weirs, PKW 2011. doi:10.1201/b12349-28.
- Lempérière, F. and Ouamane, A. (2003) “The Piano Keys weir: A new cost-effective solution for spillways,” International Journal on Hydropower and Dams [Preprint].
- Lempérière, F., Vigny, J.P. and Ouamane, A. (2011) “General comments on labyrinths and Piano Key Weirs: The past and present,” in Labyrinth and Piano Key Weirs - Proceedings of the International Conference on Labyrinth and Piano Key Weirs, PKW 2011.
- Machiels, O. et al. (2011) “Influence of the Piano Key Weir height on its discharge capacity,” in Labyrinth and Piano Key Weirs - Proceedings of the International Conference on Labyrinth and Piano Key Weirs, PKW 2011. doi:10.1201/b12349-10.
- Machiels, O. (2012) Experimental study of the hydraulic behaviour of Piano Key Weirs.
- Machiels, O. et al. (2014) “An analytical approach for piano key weir hydraulic design,” in Labyrinth and Piano Key Weirs II, PKW 2013 - Proceedings of the 2nd International Workshop on Labyrinth and Piano Key Weirs 2013. doi:10.1201/b15985-19.
- Machiels, Olivier et al. (2014) “Experimental parametric study and design of Piano Key Weirs,” Journal of Hydraulic Research [Preprint]. doi:10.1080/00221686.2013.875070.
- Machiels, O., Erpicum, S. and Piroton, M. (2012) “Experimental analysis of PKW hydraulic performance and geometric parameters optimum,” in Proceedings of International Workshop on Piano Key Weir for In-stream Storage and Dam Safety (PKWISD-2012).

- Mehboudi, A., Attari, J. and Hosseini, S. (2017) “Flow regimes over trapezoidal Piano Key Weirs,” in *Labyrinth and Piano Key Weirs III – PKW 2017*. doi:10.1201/9781315169064-9.
- Mehboudi, A., Attari, J. and Hosseini, S.A. (2016) “Experimental study of discharge coefficient for trapezoidal piano key weirs,” *Flow Measurement and Instrumentation* [Preprint]. doi:10.1016/j.flowmeasinst.2016.06.005.
- Nosedá, M. et al. (2019) “Upstream Erosion and Sediment Passage at Piano Key Weirs,” *Journal of Hydraulic Engineering*, 145(8).
- Noui, A. and Ouamane, A. (2011) “Study of optimization of the Piano key weir,” in *Labyrinth and Piano Key Weirs - Proceedings of the International Conference on Labyrinth and Piano Key Weirs, PKW 2011*. doi:10.1201/b12349-27.
- Oertel, M. (2015) “Discharge Coefficients of Piano Key Weirs From Experimental and Numerical Models,” 36th IAHR World Congress [Preprint].
- Ouamane, A. and Lempérière, F. (2006) “Design of a new economic shape of weir,” in *Proceedings of the International Symposium on Dams in the Societies of the 21st Century, ICOLD-SPANCOLD - Dams and Reservoirs, Societies and Environment in the 21st Century*. doi:10.1201/b16818-74.
- Paxson, G.S., Tullis, B.P. and Hertel, D.J. (2013) “Comparison of piano keyweirs with labyrinth and gated spillways: Hydraulics, cost, constructability and operations,” in *Labyrinth and Piano Key Weirs II*. doi:10.1201/b15985.
- Pfister, M. et al. (2014) “Scale effects related to the rating curve of cylindrically crested Piano Key weirs ,” in *Labyrinth and Piano Key Weirs – PKW 2013* , pp. 73–84.
- Pfister, M., Jüstrich, S. and Schleiss, A.J. (2017) “Toe-scour formation at Piano Key Weirs,” in *Labyrinth and Piano Key Weirs III*, pp. 147–156.
- Pfister, M., Schleiss, A.J. and Tullis, B.P. (2014) “Effect of driftwood on hydraulic head of Piano Key weirs,” in *Labyrinth and Piano Key Weirs II – PKW 2013*, pp. 255–264.
- Pralong, J., Vermeulen, J., et al. (2011) “A naming convention for the Piano Key Weirs geometrical parameters,” in *Labyrinth and Piano Key Weirs -*

Proceedings of the International Conference on Labyrinth and Piano Key Weirs, PKW 2011. doi:10.1201/b12349-40.

- Pralong, J., Montarros, F., et al. (2011) “A sensitivity analysis of Piano Key Weirs geometrical parameters based on 3D numerical modeling,” in Labyrinth and Piano Key Weirs - Proceedings of the International Conference on Labyrinth and Piano Key Weirs, PKW 2011. doi:10.1201/b12349-21.
- Ribeiro, M.L. et al. (2012) “Hydraulic design of a-type piano key weirs,” Journal of Hydraulic Research [Preprint]. doi:10.1080/00221686.2012.695041.
- Safarzadeh, A. and Noroozi, B. (2017) “3D Hydrodynamics of Trapezoidal Piano Key Spillways,” International Journal of Civil Engineering [Preprint]. doi:10.1007/s40999-016-0100-8.
- Schleiss, A.J. (2011) “From labyrinth to Piano Key weirs - A historical review,” in Labyrinth and Piano Key Weirs - Proceedings of the International Conference on Labyrinth and Piano Key Weirs, PKW 2011. doi:10.1201/b12349-3.
- Sharma, N. and Tiwari, H. (2014) “Experimental study on vertical velocity and submergence depth near Piano Key weir ,” in Labyrinth and Piano Key Weirs II - PKW 2013, pp. 93–100.
- Tullis, S.P. et al. (1995) “DESIGN OF LABYRINTH SPILLWAYS,” Journal of Hydraulic Engineering, 121, pp. 247–255

---

## Chapter 3

### Fish Passes

---

For decades, humans have modified water bodies, including rivers, for agriculture, navigation or hydropower. For these purposes, many structures have been built resulting in altered habitats, modified flows, loss of river continuity and connectivity and especially severe damaging impacts on the aquatic environment (Nilsson and Berggren, 2000; Nilsson *et al.*, 2005; Moore, Arrigoni and Wilcox, 2012). Indeed, rivers support some of the most biodiverse ecosystems in the world, but also some of the most threatened because of habitat fragmentation (Liermann *et al.*, 2012), which includes fish (Franchi *et al.*, 2014; Poulos *et al.*, 2014), amphibians (Naniwadekar and Vasudevan, 2014) and macroinvertebrates habitats (Holt *et al.*, 2015). Fish movements can be classified as migrations (synchronized movements by populations motivated by the transitory availability and changing location of key resources) and dispersal (one-way movement, away from a site as a result of individual behavioral decisions made at different life stages, temporal and spatial scales). Both moves play an essential role for human population, such as food consumption, as well as for ecosystems welfare, so the anthropogenic barrier strongly affect populations and the persistence of some species (Lucas and Baras, 2001; Radinger and Wolter, 2014).

In Europe, the most common pressures on surface water bodies are hydromorphological, affecting 40% of such bodies, with 17% designated as heavily modified or artificial (European Environment Agency, 2018). Indeed, nearly

---

630,000 barriers have been added to the Adaptive Management of Barriers in European Rivers (AMBER) Barrier Atlas, however, this inventory is probably still lacking the astonishing amount of 600,000 barriers (Belletti *et al.*, 2020). Considering the crucial role of freshwater fish populations and the countless ecosystem services they provide (Lynch *et al.*, 2016), efforts must be done to ensure the maintenance of fish habitats. Within this context, the European Environment Agency (European Environment Agency, 2018) aims to establish policies to ensure that enough good-quality water is available for both people's needs and the environment. Some of the measurements to ensure the restoration of hydromorphological conditions include:

- Improve river continuity by removing obstacles and installing fish passes.
- Restoring aquatic habitats by improving physical habitats.
- Managing sediment to ensure the correct transportation along the length of rivers.
- Restoring the natural water flow regime through, for example, setting minimum flow and ecological flow requirements.

Fishways, also known as fish passes, represent an effective solution to improve some of these hydromorphological conditions. They can be defined as any structure deliberately designed to facilitate a safe fish movement (migration or dispersal) to overtake an obstacle. They are usually installed to help improving the river connectivity and to contribute restoring minimum ecological flow in rivers, improving the damaging effects of barriers (Schilt, 2007) by allowing upstream and downstream movements (Calles and Greenberg, 2009). Depending on their design, fish passes can be classified as: (a) technical structures (pool-type, vertical-slot and Denil fishways), (b) nature-like structures (nature-like bypass channels and fish ramps) and (c) special-purpose structures (eel ladders, fish locks and fish lifts) (Food and Agriculture Organization of the United Nations, 2002). In this chapter, the main hydraulic requirements needed for fish passes are presented, as well as several types of fish pass structures and the limits of application for each type.

### **3.1 Hydraulic requirements for fish passes**

To achieve an effective installation of fish passes, several requirements are needed to allow the effective pass of fishes. In this context, both an “hydraulic” and a “biological” operating range should be properly specified. The hydraulic range pertains the correct operating range for the fish pass, thus, establishing the minimum flow required for helical currents to generate. Below this flow the fishway acts as a mini-pool pass and above a certain flow, the helical currents only form occasionally, the flow progressively becomes supercritical, and the baffles do not fulfil their energy-dissipating role. The biological operating range regards defining the most suitable fish pass and baffle for certain species and certain sizes of fish. However, certain requirements can be generally applied and are herein presented.

#### **3.1.1 Fish pass entrance and attraction flow**

The current perception by aquatic organisms plays a crucial role in their ability to guide in rivers. Fish are generally characterized by positive rheotaxis, which means they usually swim against the main oncoming current, however, they not only swim within the maximum flow but also along its edge. Indeed, if there is an obstruction blocking the movement process, the fish seeks forward routes by trying to border the obstacle. Therefore, the attraction effectiveness of a fish pass depends on the location of its entrance in relation to the river obstruction (dam, weir, barrage, etc), and the hydraulic conditions, such as flow discharges, velocities, and flow patterns, near the entrance. The fish pass entrance must be located where the fish concentrate, which ultimately depends on the tailwater currents and the obstacle type. For instance, these may be located directly downstream of the weir or dam, at the foot of the barrage or at the turbine outlets in hydropower plants. Nonetheless, the velocity of the attracting current formed at the entrance of the fish pass can be within the range of 0.8 to 2.0 m s<sup>-1</sup> (Food and Agriculture Organization of the United Nations, 2002). The entrance of the fish pass must be submerged, including the most downstream baffle if present, to a depth sufficient to prevent any

local acceleration in flow and avoiding the formation of drops. Likewise, fish must be able to enter a baffle fishway swimming, without having to jump (Larinier, 2002).

### **3.1.2 Discharge and current conditions in the fish pass**

Discharge through a fish pass is frequently of great importance for originating and stimulating upstream migration (Aarestrup and Koed, 2003; Arnekleiv and Rønning, 2004; Mitchell and Cunjak, 2007). The discharge through a fish pass depends on the fish pass type, the geometric characteristics and the headwater. However, some hydraulic constraints should be always considered. For instance, the discharge through the fish pass must be sufficient to compete with the flow in the river during the migration period. Generally, this flow must be of the order of 2–5% of the competing flow, which can be either the turbine discharge, the ecological flow or the spilling discharge at the weir (Larinier, 2008). The flow turbulence through the fish pass must be as low as possible, allowing the fish to migrate through the pass regardless of their swimming ability. Indeed, the fish pass must ensure low velocity flow, permitting turbulent flow just at certain locations. A flow velocity limit of  $2.0 \text{ m s}^{-1}$  must be assured at all points to achieve the effective design of the fish pass; however, the average velocity value must be considerably lower than this limit (Food and Agriculture Organization of the United Nations, 2002).

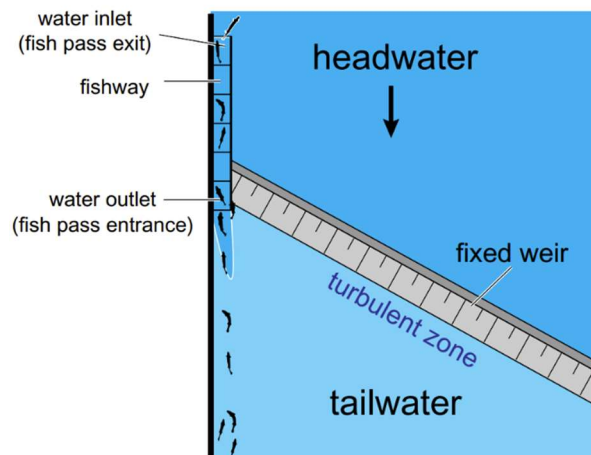


**Fig. 3.1 Fish pass entrance and exit** (Food and Agriculture Organization of the United Nations, 2002)

### **3.1.3 Fish pass exit conditions**

For fish pass located near hydropower plants, specific conditions must be considered regarding the exiting conditions of the fish pass to the headwater. The fish pass exit should avoid any zone where the presence of attraction currents from the weir or the turbine intake may attract fish, thus, a recommended minimum distance of 5 m should be always respected. If the headwater current has a velocity higher than  $0.5 \text{ m s}^{-1}$ , the exit area must be extended by a partition wall (Food and Agriculture Organization of the United Nations, 2002).

### **3.1.4 Optimal location of the fish pass on the river**

The location of the fish pass on the river is one of the key factors for its effective operations. On natural rivers, the whole cross section allows fish to pass, however, when a dam or weir is installed, this section is considerably reduced and the effective geometry of the fish pass is restraint by engineering, hydraulic and economic constraints, especially in larger rivers. Usually, fish and aquatic invertebrates move upstream in, or along, the main current, so to facilitate the detection of the fish pass entrance, the structure should be located at the bank of the river where the highest current is begot. Additionally, positioning the fish pass at the bank allows connecting more easily the fish pass bottom substrate to the bank substrate. Regarding the optimal location nearby hydroelectric power stations, two main options can be considered. The former is to build the fish pass at the power station, preferably in the riverbank, as fish are attracted by the flow discharge coming from the turbines. The latter is to build the fish pass at the weir, acting as a connection between the original natural main channel and the headwater of the impoundment. As fish follows the strongest current, in general conditions, they more likely are attracted by the turbine rather than the weir. Nonetheless, if excess water is discharged over the weir or the weir provides the minimum ecological flow, this current may be also attracting. From an ecological viewpoint, the best solution would be to install two fish passes, one at the hydropower plant and the other one at the weir.

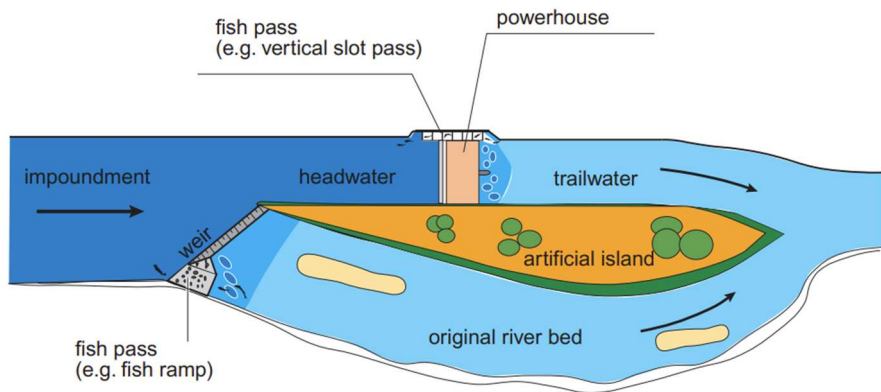


**Fig. 3.2. Fish locations at hydropower plants** (Food and Agriculture Organization of the United Nations, 2002)

## 3.2 Technical fish passes

### 3.2.1 Pool passes

A pool pass consists of a channel divided through cross-walls, forming a sequence of stepped pools. Fishes migrate from one pool to the subsequent through openings in the cross-walls that are placed at the bottom (submerged orifices) or at the top (notches) (Figure 3.3). Fishes only encounter high flow velocities during their passage through the orifices, whereas the pools offer shelter for resting, given the low flow velocities. The application limits are:

- difference in water level  $\Delta h < 0.2$  m.
- bottom slopes,  $I$ , from 1:7 to 1:15. Steeper slopes can be achieved with shorter pools, but anyway respecting the allowable differences in water level.
- length of the pools ranges from 1.0 m to 2.25 m.

The pool dimension must be great enough to allow fishes moving and to dissipating sufficient energy to achieve a low turbulence flow. Moreover, the bottom of the pools must always have a rough surface to reduce the flow velocity in the proximity of the bottom.

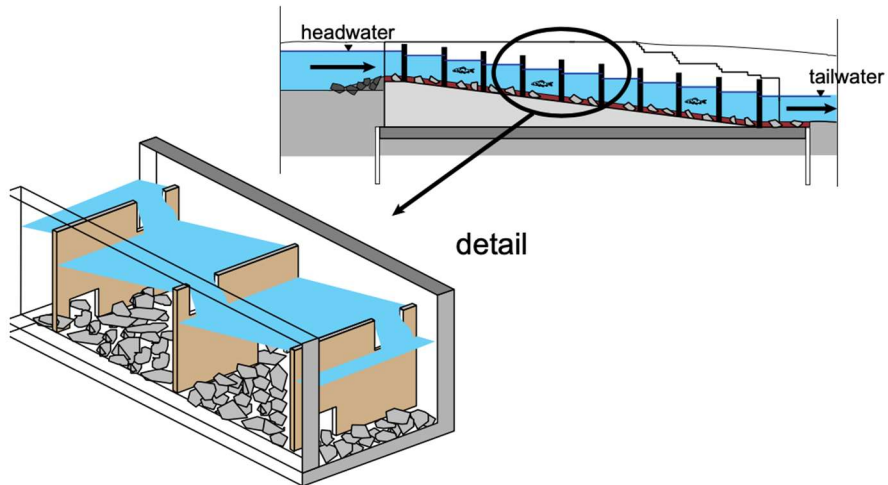


**Fig. 3.3 Conventional pool type fish pass** (Food and Agriculture Organization of the United Nations, 2002)

Conventional pool passes are characterised by vertical cross-walls located at  $90^\circ$  angles to the pool main flow direction. Submergence of cross-walls should be avoided wherever possible, allowing the discharge only through surface notches and leaving the submerged orifices to fish pass. Another pool-pass type is the rhomboid pass, which differs from the conventional pool pass as cross-walls are arranged obliquely (between  $45^\circ$  to  $60^\circ$ ) and alternatively to the pool axis, thus, having each pool a long side and a short side. Submerged orifices are always located at the upstream end of the cross-wall whereas surface notches are always in the downstream corner. The advantages of this design are more favourable flow characteristics in the pools and improved self-cleaning. The inclined cross-walls act as guides leading the ascending fish to the next orifice (Food and Agriculture Organization of the United Nations, 2002).

### 3.2.2 Vertical Slot Pass

The slot pass is a variation of the pool pass where the cross-walls are notched by vertical slots extending over the entire height of the cross-wall. The cross-walls present one or two slots and in the one-slot design and the slots are always on the same side, which differs from the pool passes orifices that have an alternated

arrangement. The shape of the cross-walls should avoid short-circuit current, meaning that water pass through the pools in a straight line from slot to slot, but allow the main current to curl back on itself, employing the entire pool volume to dissipate energy to achieve low turbulence flow. Incorporating a hook shaped projection into the cross-walls can encourage such current regimes as it deflects the flow in the area in front of the slot aperture (Figure 3.4).



**Fig. 3.4 Vertical Slot fish pass** (sources: Food and Agriculture Organization of the United Nations and upcommons.upc.edu)

### **3.2.3 Denil pass**

#### *3.2.3.1 Denil pass overview*

The Denil fish pass consists of a linear channel, in which baffles are regularly arranged at short intervals, angled against the flow direction (Figure 3.5). Frequent baffles make the channel very rough, which results in considerably high energy dissipation (Cea *et al.*, 2007). The current within the Denil pass is divided into two parts: the main current along the centre axis of the channel and lateral currents along the frame position. The energy dissipation is considerable high due to the interaction of these currents, allowing a relatively low flow velocity in the lower part of the baffle. This allows the Denil pass to have a steeper slope compared with other fish passes and to overcome greater height difference between the head- and tailwater over fairly short distances.

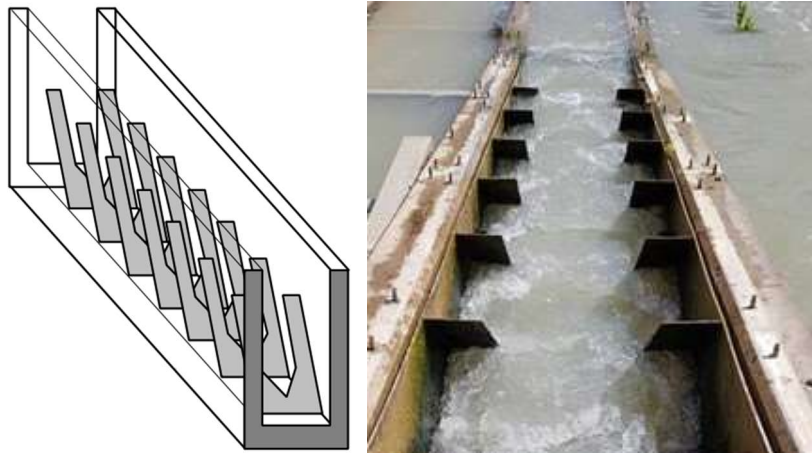


**Fig. 3.5 Denil fish pass** (sources: Food and Agriculture Organization of the United Nations and wetlandinfo.des.qld.gov.au)

The Denil fish pass has the following advantages:

- steeper slopes in comparison with other fish passes.
- not susceptible to tailwater level variations.
- usually begets a good current attraction in the tailwater.

However, this pass also presents some disadvantages:

- high susceptibility to headwater level variations, with a maximum variation of about 0.2 m;
- more easily clogged with debris so requires regular maintenance.
- experimental tests have shown that the extrapolation of data for other Denil passes with different geometric parameters is highly undefined.

The hydraulic conditions (velocity, turbulence and discharge) of Denil passes have been proven successful just for specific species like salmonids and cyprinids. Their application is thus advised where other structures cannot be installed, for instance, due to the lack of great space.

### 3.2.3.2 Denil pass geometric characteristics

Denil passes are geometric characterized according to the fish target species, limiting channel and baffles geometry. The channel geometric constrains are gathered in Table 3.1 and presented herein:

- maximum length of the channel between 6-8 m for cyprinids and 10-12 m for salmonids. This limitation is implemented because fish must surpass the Denil pass in one episode, without resting. Nonetheless, higher distance may be achieved by dividing the structure into two and locating a resting pool between the channels.
- the channel width must be between 0.6 and 1.2 m.
- the bottom slope for the channel must be between 1:5 (20%) and 1:10 (10%).

Fish fauna	Channel width [m]	Recommended slopes		Water discharge for $h^*/ba = 1.5$ [ $m^3s^{-1}$ ]
		%	1:n	
<b>Brown trout, Cyprianids and others</b>	0.6	20.0	1:5.00	0.26
	0.7	17.0	1:5.88	0.35
	0.8	15.0	1:6.67	0.46
	0.9	13.5	1:7.40	0.58
	0.8	20.0	1:5.00	0.53
<b>Salmon, Sea trout and Huchen</b>	0.9	17.5	1:5.70	0.66
	1.0	16.0	1:6.26	0.82
	1.2	13.0	1:7.70	1.17

**Tab. 3.1 Guide values for channel widths and slopes in Denil passes** (Food and Agriculture Organization of the United Nations, 2002)

Regarding the baffles located within the channel, the British Institution of Civil Engineers' Committee on Fish Passes (Committee of Fish Passes, 1942) conducted a study to test 25 types of fishway baffles. They concluded that the standard design of a Denil fish pass, with baffles inclined in upstream direction at an angle of  $45^\circ$  and with a U-shaped that is triangular in its lower part, is the most efficient in terms of construction, reduction of flow velocity and increase of the passage area for fish. Furthermore, Wang et al. (Wang *et al.*, 2012) and Yu et al. (Yu, Wang and Xie, 2012) experimentally tested arc-type baffles, similar to the original Denil baffle,

characterized with V-shape notch, orifices around the notch for water flow and debris orifices for sediment cleaning on both bottom corners (Figure 3.6). They found that the flow downstream of the arc-type baffles is steadier, which facilitates fish to find the upstream direction and ascend efficiently, however, this design method carries many uncertainties, requiring additional modelling and testing in real conditions. Therefore, accounting for the traditional baffles is still recommended.

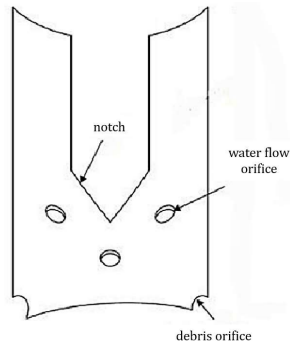


**Fig. 3.6 Arced-type baffle for a Denil pass (Wang *et al.*, 2012; Yu, Wang and Xie, 2012)**

The geometry of a single baffle is shown in Figure 3.7. The baffle cutouts dimensions,  $b_a$ ,  $c_1$  and  $c_2$ , and the distance  $s$  between the baffles depends on the channel widths. Modifications in the dimensions of Denil passes may highly influence the current conditions, thus, it is recommended to follow the prescribed geometry.

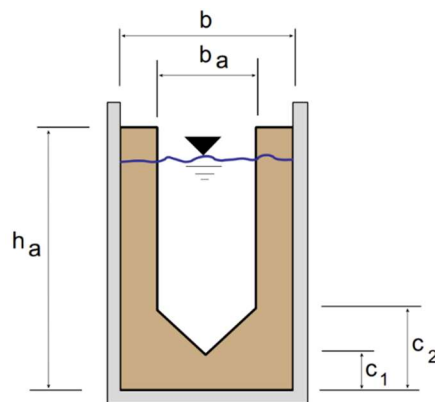


**Fig. 3.7 Baffle of a Denil pass (Food and Agriculture Organization of the United Nations, 2002)**

Values gathered in Table 3.2 can be used as guidelines for designing the baffles. The baffles are usually made of wood and, in exceptionally cases, of metal. Nevertheless, all edges must be rounded to avoid potential injuries to the fish.

		<b>Tolerance range</b> [-]	<b>Recommended guide values</b> [-]
Baffle width	$b_a/b$	0.50-0.60	0.58
Baffle spacing	$s/b$	0.50-0.90	0.66
Distance between the lowest point of the cutout and the bottom	$c_1/b$	0.23-0.32	0.25
Depth of the triangular section	$c_2/c_1$	2.00	2.00

**Tab. 3.2 Guide values for baffles dimensions in Denil passes** (Food and Agriculture Organization of the United Nations, 2002)

### 3.2.3.3 Discharge through a Denil pass

Denil baffles can be meant as a combination of a contracted rectangular weir located on the sides, without the horizontal crest, and a V-notch weir at the bottom. Nonetheless, the placement of the baffles at 45° to the bottom, which has its own slope, consistently with the distance between the baffles, entails a more challenging derivation from the classical weir equation. Additionally, the jet coming from an upstream baffle is attached to the downstream baffle, causing an adherent nappe. This means that the pressure distribution is neither hydrostatic nor atmospheric. Furthermore, when the notch is submerged, the discharge also depends on the head upstream and the water level downstream. However, the downstream water level is difficult to measure due to the flow turbulence (Odeh, 2003). Consequently, several authors proposed numerical equations based on experimental results to estimate the discharge through a Denil pass.

Katopodis et al. (Katopodis, Rajaratnam and Tovell, 1997) proposed the following discharge equation:

$$Q = \sqrt{g I b_a^5} \left[ 1.15 \left( \frac{h^*}{b_a} \right)^{1.85} \right] \quad (3.1)$$

where  $b_a$  is the cut-out width of the baffle [m],  $I$  is the slope of the channel bottom [-] and  $h^*$  is the upstream head from the V-notch [m], as shown in Figure 3.8.

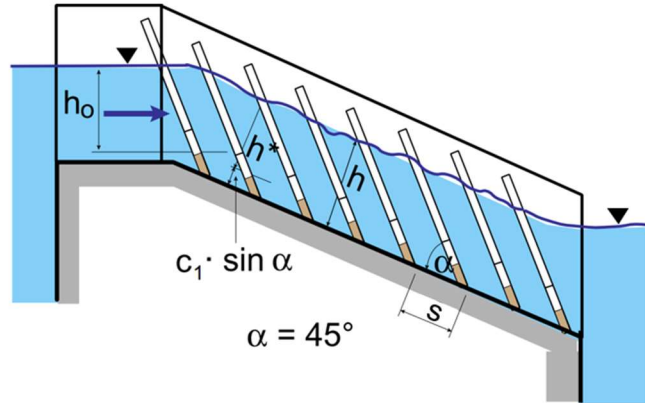


**Fig. 3.8 Longitudinal section of a Denil pass passes** (Food and Agriculture Organization of the United Nations, 2002)

Additionally, the FAO has recommended using the Krüger et al. (Krüger, 1994) discharge equation, namely:

$$Q = 1.35 b_a^{2.5} \sqrt{g} I \left( \frac{h^*}{b_a} \right)^{1.584} \quad (3.2)$$

Moreover, Odeh presented a discharge equation that depends on the upstream water level,  $h_u$ , instead of  $h^*$ , with a discharge coefficient dependant on the bottom channel slope. Therefore, the discharge can be calculated as:

$$Q = C_D h_{up}^{1.75} b_a^{0.75} \sqrt{g} I \quad (3.3)$$

where  $C_D$  can be calculated as:

$$C_D = 1.24 - 1.84I \quad (3.4)$$

and  $h_{up}$  is the upstream water level of the reservoir above the V-notch of the most upper baffle [m] that can be calculated from:

$$h_{up} = h_E - c_1 \sin(45 + \arctan I) \quad (3.5)$$

where  $h_E$  the water level in the exit channel [m].

On the other hand, some authors have successfully studied the hydraulic behaviour of Denil passes using CFD models, by both assessing the discharge through a Denil fish pass and characterizing flow discharge, velocity profiles and flow patterns (Plymesser, 2014; Mahmoudian, Baharvand and Lashkar-Ara, 2019).

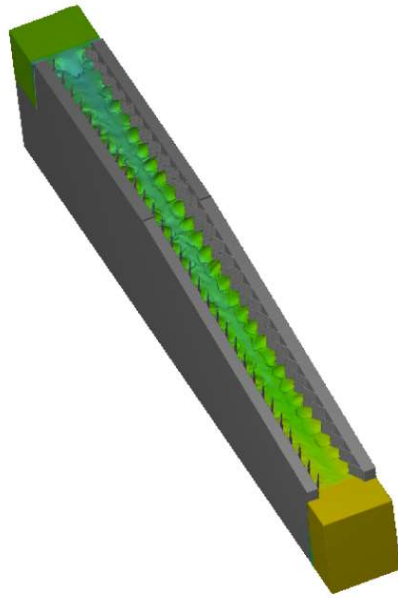


**Fig. 3.9** CFD models of Plymesser (Plymesser, 2014)

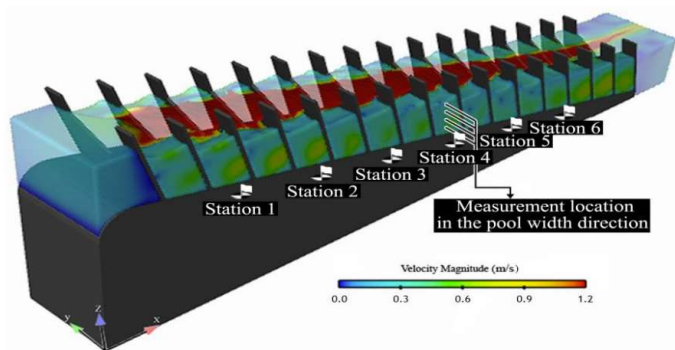


**Fig. 3.10** CFD models of Mahmoudian et al. (Mahmoudian, Baharvand and Lashkar-Ara, 2019)

## References

- Aarestrup, K. and Koed, A. (2003) “Survival of migrating sea trout (*Salmo trutta*) and Atlantic salmon (*Salmo salar*) smolts negotiating weirs in small Danish rivers,” *Ecology of Freshwater Fish*, 12(3), pp. 169–176. doi:10.1034/j.1600-0633.2003.00027.x.
- Arnekleiv, J.V. and Rønning, L. (2004) “Migratory patterns and return to the catch site of adult brown trout (*Salmo trutta* L.) in a regulated river,” *River Research and Applications*, 20(8), pp. 929–942. doi:10.1002/rra.799.
- Belletti, B. et al. (2020) “More than one million barriers fragment Europe’s rivers,” *Nature*, 588(7838), pp. 436–441. doi:10.1038/s41586-020-3005-2.
- Calles, O. and Greenberg, L. (2009) “Connectivity is a two-way street—the need for a holistic approach to fish passage problems in regulated rivers,” *River Research and Applications*, 25(10), pp. 1268–1286. doi:10.1002/rra.1228.
- Cea, L. et al. (2007) “Application of Several Depth-Averaged Turbulence Models to Simulate Flow in Vertical Slot Fishways,” *Journal of Hydraulic Engineering*, 133(2), pp. 160–172. doi:10.1061/(ASCE)0733-9429(2007)133:2(160).
- Committee of Fish Passes (1942) “Rep. of the committee of fish-passes.”
- European Environment Agency (2018) *European waters - assessment of status and pressures 2018*.
- Food and Agriculture Organization of the United Nations, D.V. für W. und K. e. V. (DVWK) (2002) *Fish passes - Design, dimensions and monitoring*.
- Franchi, E. et al. (2014) “Changes in the fish community of the upper Tiber River after construction of a hydro-dam,” *Journal of Limnology*, 73(2). doi:10.4081/jlimnol.2014.876.
- Holt, C.R. et al. (2015) “Macroinvertebrate Community Responses to Annual Flow Variation from River Regulation: An 11-Year Study,” *River Research and Applications*, 31(7), pp. 798–807. doi:10.1002/rra.2782.
- Katopodis, C., Rajaratnam, N. and Tovell, D. (1997) “DENIL FISHWAYS OF VARYING GEOMETRY By C. Katopodis, Member, ASCE, N. Rajaratnam/ Fellow,

- ASCE, S. WU,3 and D. Tovell 4,” *Journal of Hydraulic Engineering*, 123(c), pp. 624–631.
- Krüger, F. (1994) “Denil-Fischpässe,” *Wasserwirtschaft/Wassertechnik*, 3(94), pp. 24–32.
  - Larinier, M. (2002) “BAFFLE FISHWAYS,” *Bulletin français de la pêche et de la pisciculture*, (364), pp. 83–101.
  - Larinier, M. (2008) “Fish passage experience at small-scale hydro-electric power plants in France,” *Hydrobiologia*, 609(1), pp. 97–108. doi:10.1007/s10750-008-9398-9.
  - Liermann, C.R., et al. (2012) “Implications of dam obstruction for global freshwater fish diversity,” *Bioscience*, 62, pp. 539–548.
  - Lucas, M.C. and Baras, E. (2001) *Migration of freshwater fishes*. Blackwell Science Ltd.
  - Lynch, A.J. et al. (2016) “The social, economic, and environmental importance of inland fish and fisheries,” *Environmental Reviews*, 24(2), pp. 115–121. doi:10.1139/er-2015-0064.
  - Mahmoudian, Z., Baharvand, S. and Lashkar-Ara, B. (2019) “Investigating the Flow Pattern in Baffle Fishway Denil Type,” *Irrigation Sciences and Engineering (JISE)*, 42(3), pp. 179–196. doi:10.22055/jise.2019.23693.1689.
  - Mitchell, S.C. and Cunjak, R.A. (2007) “Relationship of upstream migrating adult Atlantic salmon ( *Salmo salar* ) and stream discharge within Catamaran Brook, New Brunswick,” *Canadian Journal of Fisheries and Aquatic Sciences*, 64(3), pp. 563–573. doi:10.1139/f07-032.
  - Moore, J.N., Arrigoni, A.S. and Wilcox, A.C. (2012) “Impacts of Dams on Flow Regimes in Three Headwater Subbasins of the Columbia River Basin, United States 1,” *JAWRA Journal of the American Water Resources Association*, 48(5), pp. 925–938. doi:10.1111/j.1752-1688.2012.00660.x.
  - Naniwadekar, R. and Vasudevan, K. (2014) “Impact of Dams on Riparian Frog Communities in the Southern Western Ghats, India,” *Diversity*, 6(3), pp. 567–578. doi:10.3390/d6030567.

- Nilsson, C. et al. (2005) “Fragmentation and Flow Regulation of the World’s Large River Systems,” *Science*, 308(5720), pp. 405–408. doi:10.1126/science.1107887.
- Nilsson, C. and Berggren, K. (2000) “Alterations of Riparian Ecosystems Caused by River Regulation,” *BioScience*, 50, pp. 783–792.
- Odeh, M. (2003) “Discharge Rating Equation and Hydraulic Characteristics of Standard Denil Fishways,” *Journal of Hydraulic Engineering*, 129(5), pp. 341–348. doi:10.1061/(asce)0733-9429(2003)129:5(341).
- Plymesser, K.E. (2014) “Modeling Fish Passage and Energy Expenditure for American Shad in a,” Thesis, (January), p. 178.
- Poulos, H.M. et al. (2014) “Fish Assemblage Response to a Small Dam Removal in the Eightmile River System, Connecticut, USA,” *Environmental Management*, 54(5), pp. 1090–1101. doi:10.1007/s00267-014-0314-y.
- Radinger, J. and Wolter, C. (2014) “Patterns and predictors of fish dispersal in rivers.,” *Fish and Fisheries*, 15(3), pp. 456–473.
- Schilt, C.R. (2007) “Developing fish passage and protection at hydropower dams,” *Applied Animal Behaviour Science*, 104(3–4), pp. 295–325. doi:10.1016/j.applanim.2006.09.004.
- Wang, J. et al. (2012) “Ecological fishway installed with arc-type baffles,” in *Applied Mechanics and Materials*, pp. 2008–2012. doi:10.4028/www.scientific.net/AMM.170-173.2008.
- Yu, F., Wang, J. and Xie, L. (2012) “Hydrodynamic characteristics in ecological arc-shaped baffle fishway,” in *Applied Mechanics and Materials*, pp. 1119–1122. doi:10.4028/www.scientific.net/AMM.212-213.1119.

---

## Chapter 4

### Experimental Investigations of type A PKWs

---

From the literature analysis carried out in Chapter 2, it was deduced that the discharge efficiency of PKWs significantly varies and, ultimately, it depends on the specific geometry and upstream head. This variation leads to the necessity of assessing the discharge coefficient of each geometry as many discharge equations are restricted to a certain range of application. The geometry selected was designed following the optimal range of values recommended in the literature (Chapter 2.2.2) that allows maximum discharge efficiency:  $W_i/W_o = 1.25 \div 1.5$  and  $Bo/Bi \geq 1$ . In regard to the  $P/W_u$  ratio, the optimal value in terms of efficiency would be 1.33, and from an economic viewpoint may be established equal to 0.83, therefore, the  $P/W_u$  ratio has been considered an intermediate value of 1.15.

Therefore, the aim of this chapter is further assessing the discharge efficiency of a type A PKW, by assessing the hydraulic behaviour of two configurations: a  $PKW_A$  with  $W_i > W_o$  and the same geometry but rotating the model  $180^\circ$ , obtaining a  $PKW_{A\_reverse}$  with  $W_i < W_o$  (Figure 4.1). The purpose of testing the  $PKW_{A\_reverse}$  is to collect further experimental data that will be compared to the results obtained with the numerical model.

The tests from the former geometry were performed aiming to characterize the hydraulic behaviour in terms of discharge coefficient and upstream velocity field while the latter configuration was tested in terms of discharge efficiency and for further results validation.

---

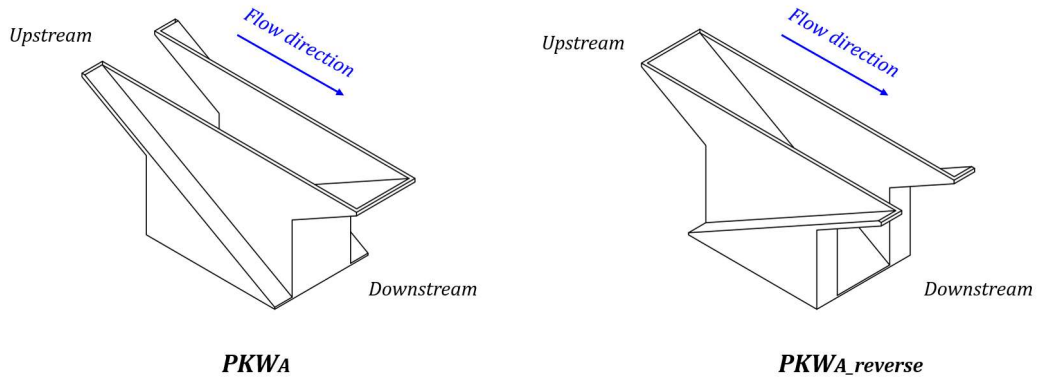


**Fig. 4.1 Isometric view of the PKW<sub>A</sub> and PKW<sub>A,reverse</sub>**

The tested type A model with detailed measures of parameters is shown in the following Figure (4.2):

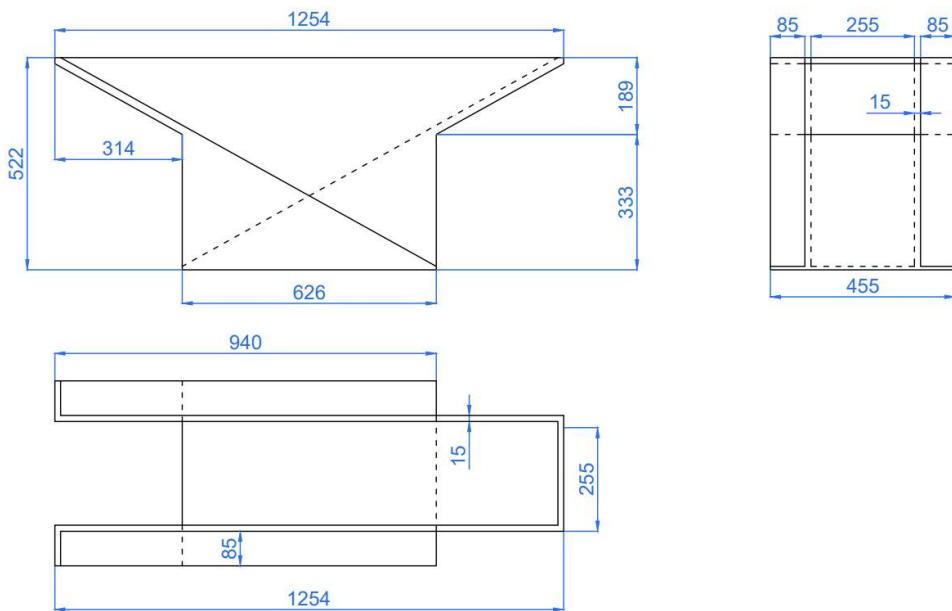


**Fig. 4.2 Cross section, plain view and lateral view of the tested type A model**

The parameters and dimensionless ratios of both the **PKW<sub>A</sub>** and the **PKW<sub>A,reverse</sub>** are gathered in Table 4.1 and Table 4.2, respectively.

<b>Type A</b>	<b>P</b>	0.522 m	<b>W<sub>i</sub></b>	0.170, 0.255 m
	<b>B</b>	1.254 m	<b>W<sub>o</sub></b>	0.255, 0.170 m
	<b>B<sub>o</sub></b>	0.314 m	<b>W<sub>u</sub></b>	0.455 m
	<b>B<sub>i</sub></b>	0.314 m	<b>L<sub>u</sub></b>	2.963 m
	<b>B<sub>b</sub></b>	0.626 m	<b>T<sub>s</sub></b>	0.015 m
<b>PKW<sub>A</sub></b>		PKW with $W_i=0.255 > W_o=0.170$		
<b>PKW<sub>A,reverse</sub></b>		PKW with $W_o=0.255 > W_i=0.170$		

Tab. 4.1 Geometry parameters for PKW<sub>A</sub> and PKW<sub>A,reverse</sub>

	<b>PKW<sub>A</sub></b>	<b>PKW<sub>A,reverse</sub></b>
<b>L/W</b>	6.51	6.51
<b>W<sub>i</sub>/W<sub>o</sub></b>	1.5	0.67
<b>B<sub>i</sub>/B<sub>o</sub></b>	1	1
<b>P/W</b>	1.15	1.15
<b>B/P</b>	2.40	2.40

Tab. 4.2 Dimensionless ratios for PKW<sub>A</sub> and PKW<sub>A,reverse</sub>

## 4.1 Laboratory set-up

The experiments were carried out at the Hydraulic Laboratory of the Department of Civil, Architectural and Environmental Engineering, University of Naples Federico II. The experimental set-up test range was defined aiming to avoid scale effects by assuring certain flow conditions that avoid viscous and surface tension effects. Namely, a minimum upstream head  $H > 3$  cm, corresponding to a Weber number above 54, as recommended by Erpicum et al., (2016). A plexiglas horizontal test channel 3.6 m long, 0.455 m wide and 1 m high was built to perform the experimental investigation, allowing the lateral observation of the flow patterns of the PKW models. The upstream side of the channel was located inside an open tank 4 m long, 1.92 m wide and with a maximum water level of about 0.59 m, with two 1 m long walls of the same channel width (Figure 4.3 and 4.4). The intake is a tank 1 m long and 4 m wide with a maximum discharge of  $80 \text{ L s}^{-1}$ . The connection between these two tanks is a grid that, in addition to the convergent walls, ensures uniform flow conditions.

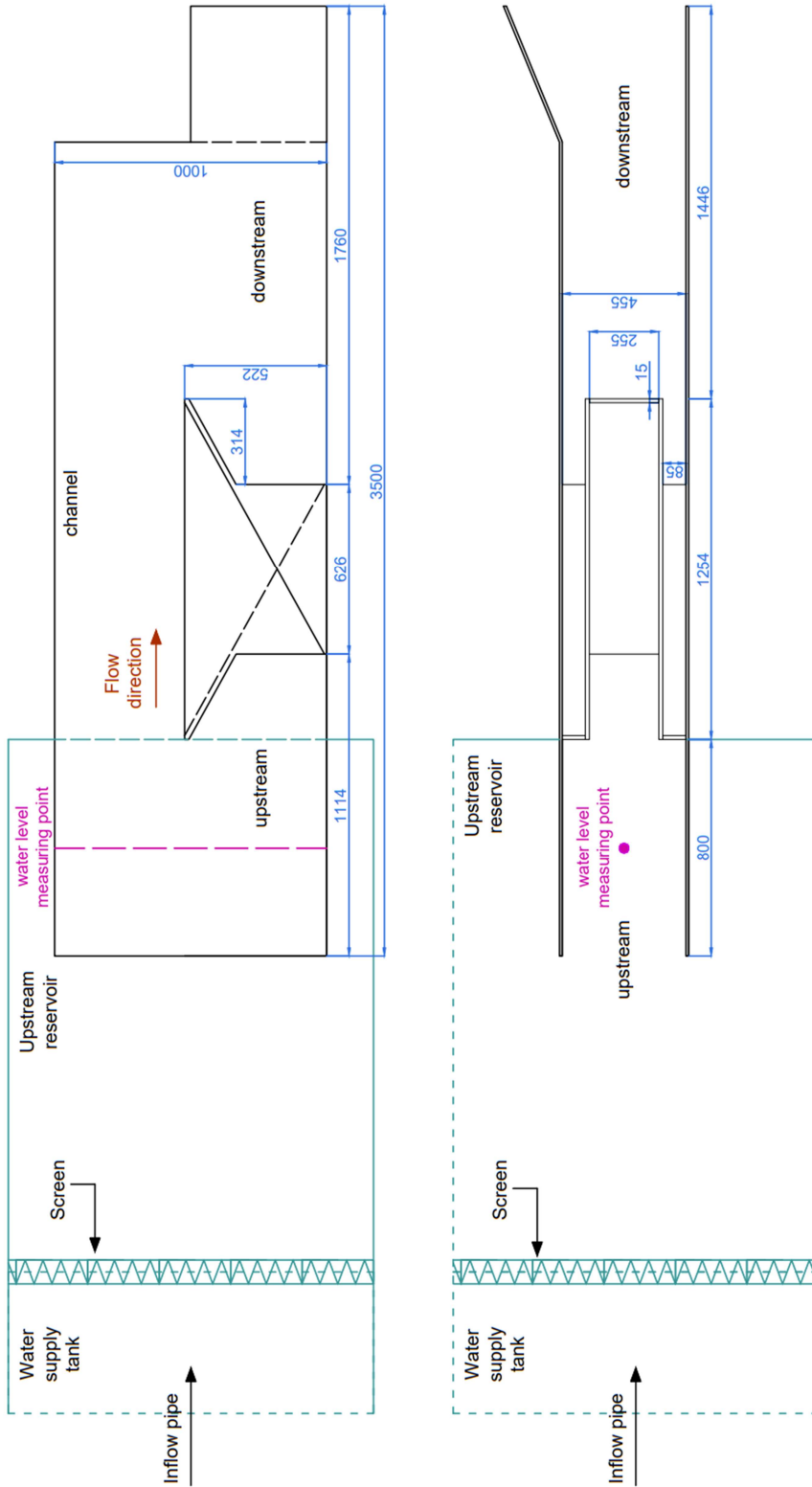


Fig. 4.3 Cross section (top) and Plain view (bottom) schemes of the laboratory setup

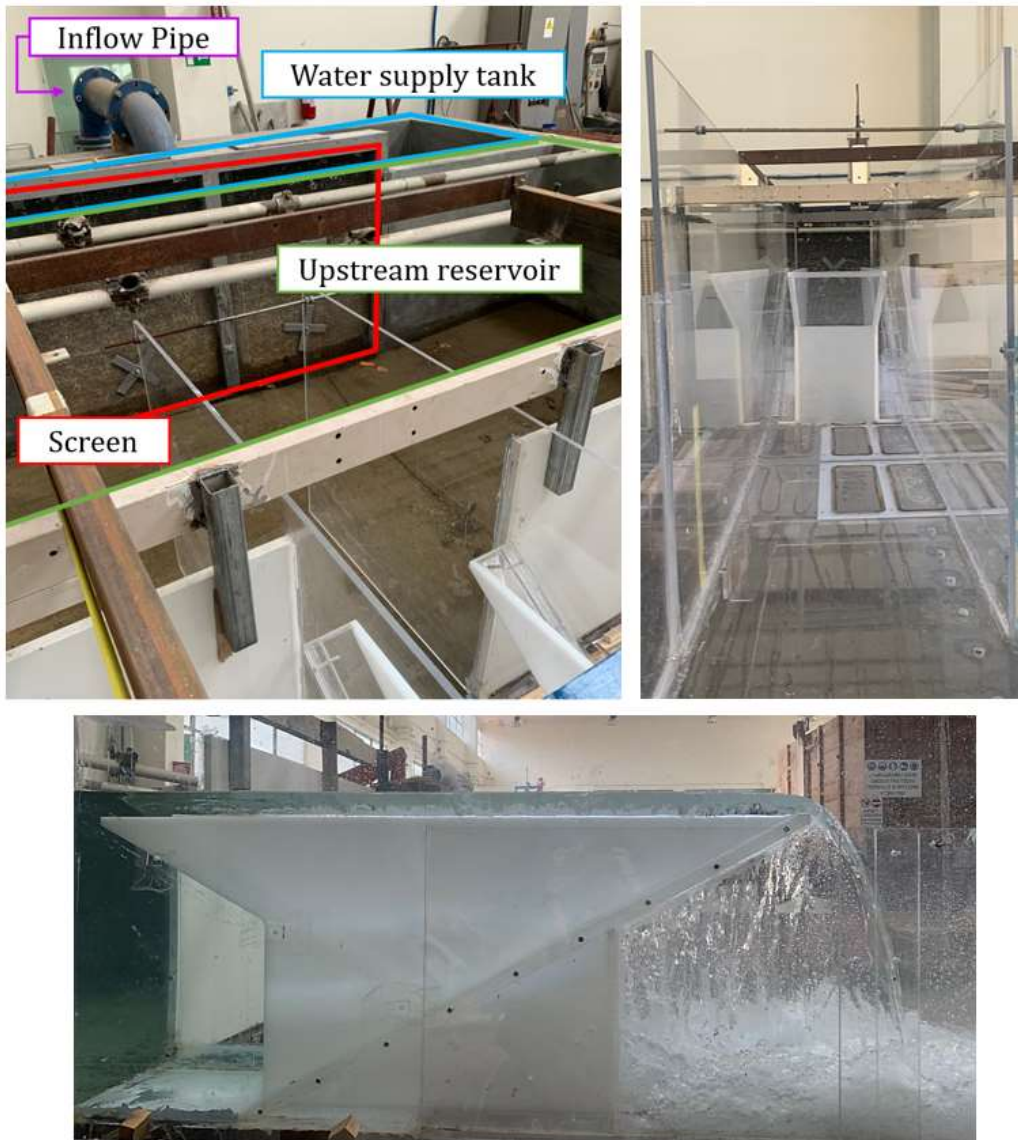
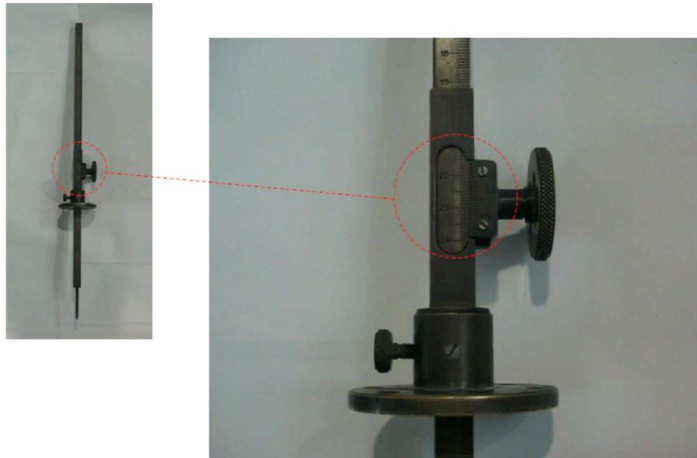


Fig. 4.4 Top left) Water supply elements; top right) channel; bottom) running test on the  $PKW_{A,reverse}$

The following devices were used to take measurements:

- A Point Gauge with  $\pm 1$  mm reading accuracy that allowed to measure the upstream water level in the channel.



**Fig. 4.5 Point Gauge**

- A Diaphragm Flowmeter to measure the inflow value to the tank. It consists of an orifice plate located into the pipe, causing pressure loss (Figure 4.6). The pressure differential before (P1) and after (P2) the orifice plate is measured through Bernoulli's principle. Specifically, the difference in flow velocity caused by the plate is measured using two pitot tubes with an accuracy of  $\pm 1$  mm, considering:

$$\Delta v = \sqrt{2g\Delta h_{diaph}} \quad (4.1)$$

where  $g$  is the acceleration of gravity [ $\text{m s}^{-2}$ ] and  $\Delta h_{diaph}$  is the differential of values measured using the pitot tubes [m]. The relationship between the flowrate and the velocity depends on the geometric characteristics of the orifice plate and the pipe where it is located. After a calibration process, the flow passing through the diaphragm,  $Q$  [ $\text{m}^3$ ], can be estimated using Equation 4.2.

$$Q = 0.04124997072 \sqrt{2g\Delta h_{diaph}} \quad (4.2)$$

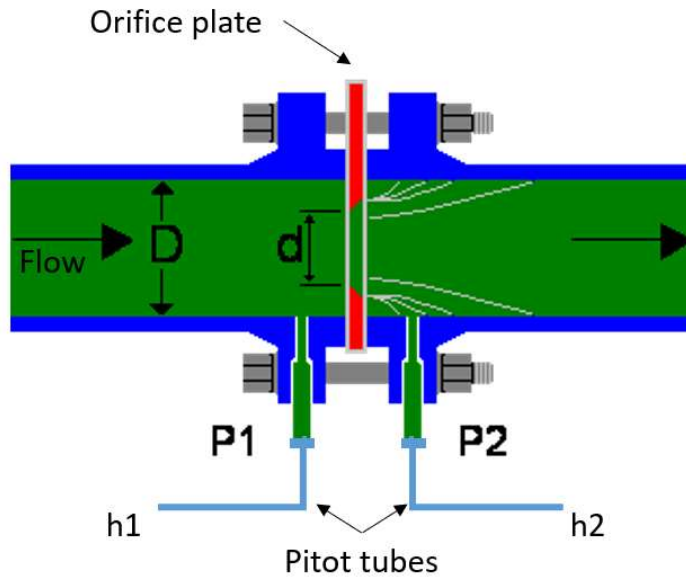
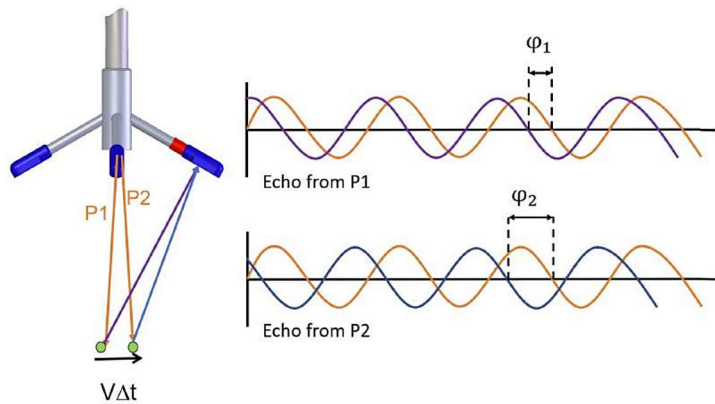


Fig. 4.6 Diaphragm flow meter

- An Acoustic Doppler velocimeter (ADV) used to measure water velocity in the inlet key of the PKW by applying the Doppler Effect principle. The Doppler Effect is the change in frequency of a sound wave when a wave source moves with respect to an observer, or when the observer itself moves relative to the wave source. The ADVs measure velocity by transmitting a pair of short sound pulses of a specific frequency into the water column. Part of the sound wave reflects back to the instrument from passive tracer particles suspended in the water, which move with the same speed as water, hence, the measurements correspond to the water flow itself (Figure 4.7). The velocity is calculated using Equation 4.3.

$$V = \frac{\Delta\phi C}{4\pi F_{source}} \Delta t \quad (4.3)$$

where  $V$  is the current velocity [ $\text{m s}^{-1}$ ],  $\Delta\phi$  is the phase difference [-],  $C$  is the speed of sound in liquid [ $\text{m s}^{-1}$ ],  $F_{source}$  is the transmitted frequency [Hz] and  $\Delta t$  is the time difference between two consecutive pulses [s].



**Fig. 4.7 Functioning principle of an ADV** (source: Nortek Manuals, 2018)

The selected ADV corresponds to a Nortek Vectrino (Figure 4.8), with a maximum velocity range of  $\pm 4 \text{ m s}^{-1}$  and an accuracy of  $\text{max}=[\pm 0.5\% \text{ measured value}; 1 \text{ mm s}^{-1}]$ .



**Fig. 4.8 Nortek Vectrino** (source: Nortek Manuals, 2018)

## 4.2 Uncertainty Analysis of Experimental Measurements

The uncertainty analysis to estimate the errors of the experimental measurements was carried out according to the Abernethy and Thompson, (1973) method. This approach is based upon the calculation of the Uncertainty,  $U$ , considered as composed of a Fixed Error or Bias Error,  $B$ , and a Random Error or Precision Error,  $R$ , of the recorded data set, calculated as:

$$U = \pm(B + t_{95}s^*) \quad (4.4)$$

with  $B$  the Fixed Error,  $s^*$  the standard deviation and  $t_{95}$  the 95<sup>th</sup> percentile of the two-tailed  $t$ -Student distribution. The Fixed Error  $B$  corresponds to the difference between the sample mean value  $\bar{x}$  and the true value  $x^*$ . In repeated measurements of the same entity, the Fixed Error remains constant, and its estimation could be achieved through instruments with greater precision, in order to quantify the distance between the measured  $x$  and the true value  $x^*$ . Moreover, for the presented experimental analysis,  $t_{95}$  was set equal to 2.00 according to (Moffat, 1982). Lastly, the statistic standard deviation  $s^*$  is related to the Random Error  $R$ , which represents the measurement variation, caused by external effects, which determines disagreements during the measurement repeating. This variation according to a probabilistic distribution follows the Normal Distribution, therefore, the mean  $\bar{\mu}$  and the variance  $\sigma^*$  can be calculated through the sample mean value  $\bar{x}$  (Equation 4.5) and the statistic standard deviation  $s^*$  (Equation 4.6), respectively:

$$\bar{x} = \frac{\sum_{i=1}^{N^*} x_i}{N^*} \quad (4.5)$$

$$s^* = \sqrt{\frac{\sum_{i=1}^{N^*} (x_i - \bar{x})^2}{N^* - 1}} \quad (4.6)$$

with  $x_i$  the individual measurement,  $\bar{x}$  the sample mean value,  $N^*$  the number of measurements and  $N^* - 1$  the statistical degrees of freedom.

For the upstream water level and the velocity field, the Fixed Error  $B$  was estimated as a function of the accuracy of the Point Gauge and the ADV, respectively.

Conversely, the error propagation method Abernethy and Thompson, (1973) was applied to estimate the Fixed Error  $B$  of the derived values, according to the following equation:

$$B = \sqrt{\sum_{j=1}^M \left( \frac{\partial f^*(x)}{\partial x_j} B(x_j) \right)^2} \quad (4.7)$$

where  $f^*$  is the function to calculate the required entity,  $M$  the number of the  $x_j$  measured parameters to calculate  $f^*(x)$  and  $B(x_j)$  the fixed error of the  $j$ -th measured parameter  $x_j$ .

### 4.3 Experimental Characterization of the Discharge Coefficient

The experimentally tested configurations were the  $PKW_A$  and  $PKW_{A\_reverse}$ , aiming to estimate the discharge coefficient and the upstream velocity distribution in the inlet key of the  $PKW_A$ .

The discharge coefficient for the PKW,  $C_{PKW}$ , has been computed using the Poleni's discharge equation (Equation 4.8):

$$C_{PKW} = \frac{Q_{PKW}}{W\sqrt{2gH^3}} \quad (4.8)$$

where  $C_{PKW}$  is the discharge coefficient for a PKW [-],  $Q_{PKW}$  is the discharge [ $m^3s^{-1}$ ] and  $H$  the head upstream the weir [m]. The discharge,  $Q_{PKW}$ , corresponds to the inflow of the tank measured through the Diaphragm (Equation 4.2) as experimental measurements were taken once the flow achieved steady flow conditions. Moreover, the upstream head,  $H$ , can be calculated according to the following Equation (4.9):

$$H = h - P + v^2/2g \quad (4.9)$$

where  $h$  is the water level measured with the Point Gauge [m],  $P$  is the PKW height (m) and  $v^2/2g$  term represents the kinetic term [m]. The velocity,  $\bar{v}$ , corresponds to the mean velocity of the section located upstream the PKW, and was calculated as (Equation 4.10):

$$\bar{v} = \frac{Q}{W \cdot h} \quad (4.10)$$

where  $Q$  is the inflow measured with the Diaphragm Flow meter [ $m^3s^{-1}$ ],  $W$  is the width of the channel corresponding to the PKW width [m] and  $h$  is the water level upstream the PKW, measured with the Point Gauge [m].

#### 4.4 Experimental Characterization of the Velocity Field in the Inlet Key

As mentioned in Section 4.2, an ADV was used to characterize the velocity field in the inlet key of the  $PKW_A$  by analysing nine points of two different sections (Figure 4.10), namely, Section A and Section B. Section A is located in the middle of the inlet key whereas Section B is located 5 cm from the lateral wall of the PKW, in order to respect the minimum distance established by the ADV manufacturer to ensure the correct gathering of data.

The velocity data obtained from the ADV was filtered using the MAJ's Velocity Signal Analyzer (MAJVSA) (Jesson, 2016). A pre-filter was applied to exclude data below a correlation limit of 80% and a Signal-to-Noise Ratio (SNR) limit of 15. The Despiking Filter applied was based on Velocity Correlation with a 12 Point 4 Order Polynomial Interpolation as Spike Replacement Method. The data obtained from the filtering process was the mean velocity value and the standard deviation in the streamwise direction ( $V_x$ ). The average uncertainty of the measurements was  $0.12 \text{ m s}^{-1}$ .

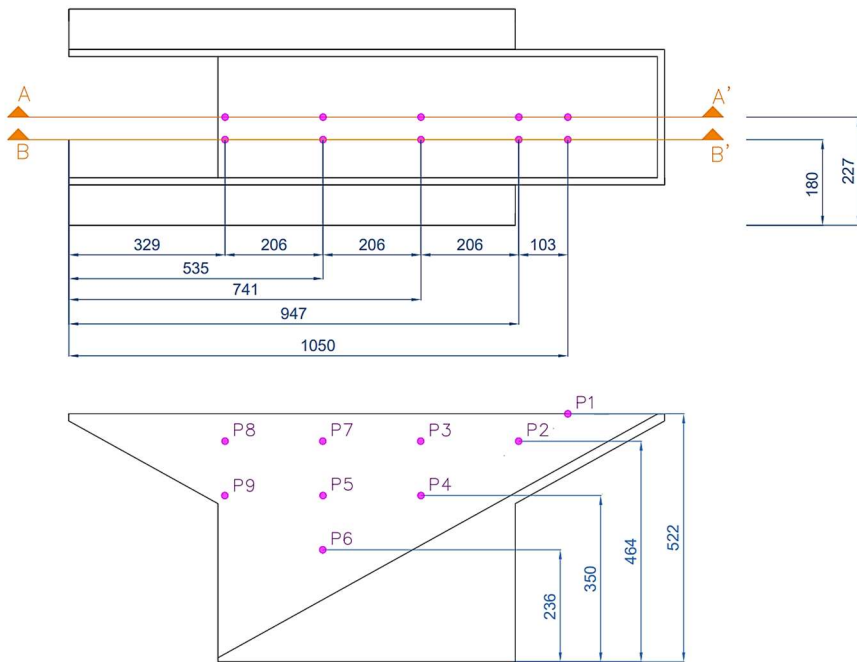


Fig. 4.9 Velocity measuring points at the  $PKW_A$

## **References**

- Abernethy, R.B. and Thompson, J.W. (1973) Handbook, Uncertainty in Gas Turbine Measurements.
- Erpicum, S. et al. (2016) “Scale effects in physical piano key weirs models,” Journal of Hydraulic Research. Taylor and Francis Ltd., pp. 692–698. doi:10.1080/00221686.2016.1211562.
- Jesson, M. (2016) MAJ’s Velocity Signal Analyser - Installation and User Guide v1.5.63.
- Moffat, R.J. (1982) “Contributions to the theory of single-sample uncertainty analysis.,” Journal of Fluid Engineering ASME, 104, pp. 250–260.
- Nortek Manuals (2018) The Comprehensive Manual for Velocimeters.

---

## Chapter 5

### CFD Modelling of type A and type B PKWs

---

As presented in the literature analysis of Chapter 2, CFD modelling has been an effective tool used in compliance with physical modelling to gather further information about the hydraulic behaviour of PKWs. Therefore, in this Chapter 5, the procedure to implement a Computational Fluid Dynamics model of PKWs is introduced. In greater detail, the herein presented analysis was focused on the implementation of three PKW geometries: the  $PKW_A$ , the  $PKW_{A\_reverse}$  and a type B PKW model,  $PKW_B$  (Figure 5.1).

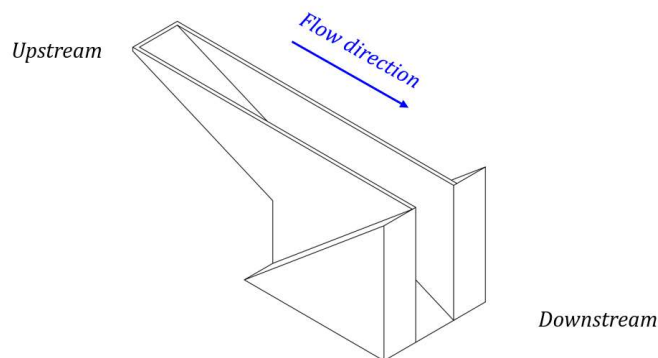


**Fig. 5.1 Isometric view of the  $PKW_B$**

The  $PKW_B$  is characterized with the same geometric features as  $PKW_A$ , in exception of the Bi/Bo ratio. This specific analysis was carried out aiming to further investigate the discharge efficiency of type B models after the results obtained from Noui and Ouamane (2011), Machiels (2012) and Cicero and Delisle (2013). The

analysis focused on the velocity field and discharge coefficient of the  $PKW_B$ , comparing the results with those corresponding to the  $PKW_A$ . The geometric parameters of the selected  $PKW_B$  are collected in Table 5.1.

$PKW_B$	$P$	0.522 m	$W_i$	0.255 m
	$B$	1.254 m	$W_o$	0.170 m
	$B_o$	0.628 m	$W_u$	0.455 m
	$B_i$	0 m	$L_u$	2.963 m
	$B_b$	0.626 m	$T_s$	0.15 m
<b>Dimensionless Ratios</b>		$L / W$		6.51
		$W_i / W_o$		1.5
		$B_i / B_o$		0
		$P / W$		1.15
		$B / P$		2.40

**Tab. 5.1 Geometric parameters and dimensionless ratios of the  $PKW_B$  tested model.**

The modelling procedure provided, as first step, the implementation of the PKW geometric configuration in a channel for later extracting the fluid domain related to the available geometry with the corresponding refinement for simulations that allowed to achieve up- and downstream suitable flow conditions. During the second step, the mesh generation was developed. Following step was directed to the simulation setting, by properly choosing the turbulence model, the boundary conditions and the applied solution methods for simulations. Moreover, a mesh sensitivity analysis was carried out aiming at finding the most suitable resolution, intended as the right balance between the results reliability and the computational time-consuming.

Therefore, simulations were performed, aiming at reproducing the fluid dynamics field of the tested devices, in order to analyse the computational results and to compare them with the performed experimental tests, discussed in Chapter 4.

The attention was specifically drawn to the difference in the hydraulic characteristics of the  $PKW_A$  and  $PKW_B$  models, specifically, in regard to the flow discharge over the upstream, downstream and lateral crests, as well as the velocity fields and surface profiles of the outlet and inlet keys.

## 5.1 3D Model

The geometric model was developed in AutoCAD® and implemented in ANSYS® DesignModeler™ tool. The size of the fluid domain was defined aiming to establish an upstream and downstream boundary at a distance of  $\sim 8P$  from the PKW, enough to achieve uniform flow condition upstream and to fully develop the hydraulic jump downstream. Then, the PKW structure was removed from the fluid domain, which was utterly discretized into six blocks.

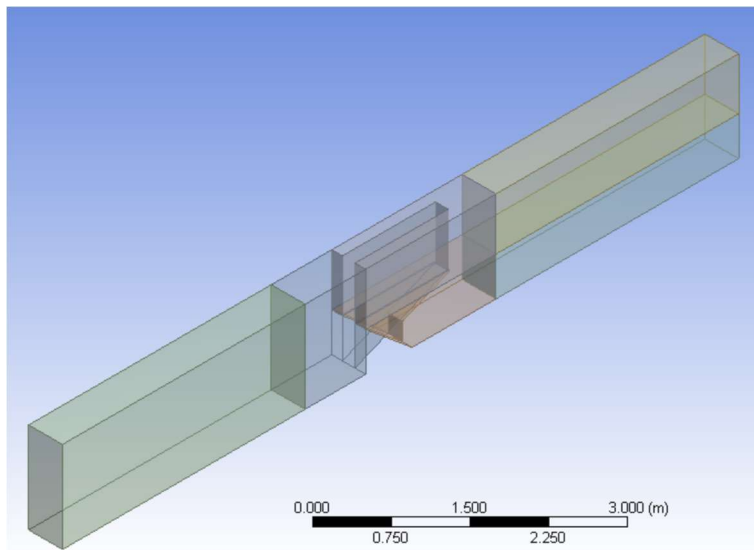


**Fig. 5.2 Isometric view of the volumes implemented in the ANSYS® DesignModeler™ tool for the PKW<sub>B</sub> model.**

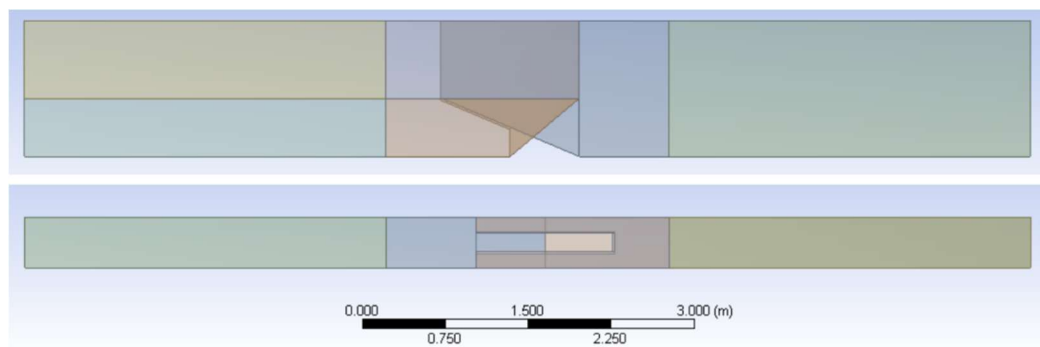


**Fig. 5.3 Lateral and plain view of the volumes implemented in the ANSYS® DesignModeler™ tool for the PKW<sub>B</sub> model.**

## 5.2 Boundary Conditions and Simulation Properties of the CFD Model for the PKWs.

Simulations were performed by using the ANSYS® Fluent™ code (*ANSYS Fluent 12.0 User's Guide*, 2019). The multiphase finite-volume method (VOF), with water and air phases was selected, and the Renormalized Group (RNG)  $k-\varepsilon$  turbulence model was selected among the settable turbulence models, with Enhanced Wall Treatment applied for the near-wall treatment. The choice of the RNG  $k-\varepsilon$  model was based in Crookston et al. (Crookston, Anderson and Tullis, 2018) research as this turbulence model is able to provide accurate results guaranteeing shorter computational times. A surface tension interaction between the primary phase (water) and the secondary phase (air) with a specific value of 0.072 N/m was accounted for.

To set the boundary conditions, the criterion followed during the experimental tests was considered, based upon the estimation of the upstream velocity, as a function of a set flow rate value. Thus, a uniform velocity distribution at inlet and a static pressure at outlet were set (Figure 5.4). In greater detail, for each simulation, the velocity magnitude was set at inlet surface and a static pressure equal to 101325 Pa was set at outlet surface. The upper surfaces were set as symmetry while lateral and bottom surfaces were considered as rigid walls. Furthermore, being the model composed of six separated volumes, ten matching interfaces were inserted to overcome the non-conformal mesh.

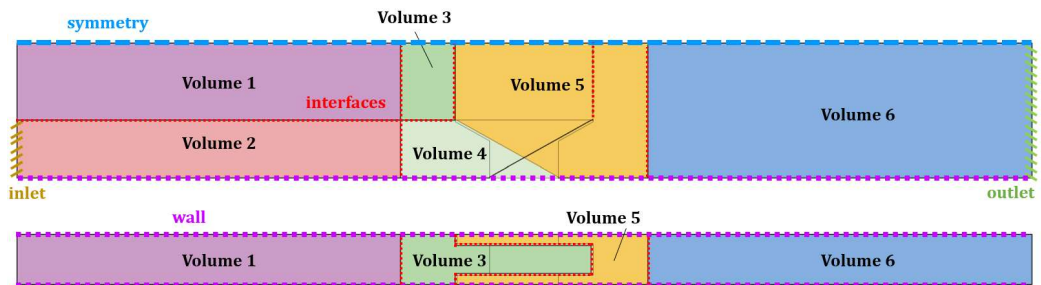


Fig. 5.4 Implemented Boundary Conditions and Interfaces

The simulations were solved applying the pressure-based solver, traditionally used for incompressible flows, with the implicit formulation, as converged steady-state solutions can be reached much faster in comparison with the explicit formulation. Furthermore, First Order Implicit Transient Formulation was set being able to provide great accuracy with less computational time and the Semi-Implicit Method for Pressure-Linked Equations (SIMPLE) algorithm was used to characterize the Pressure-Velocity coupling, established by the RANS equations. This model consists of an iterative procedure to achieve convergence and it is based upon the application of an approximation of the velocity field to solve the momentum equation. Then, the pressure gradient term is computed as a function of the pressure distribution of the previous iteration to define an updated pressure distribution, which allows to correct the face mass fluxes and the cell velocities. The choice was addressed to the SIMPLE algorithm because able to overcome the limitations related to the use of the Semi-Implicit Method for Pressure-Linked Equations Consistent (SIMPLEC).

Pressure Interpolation Scheme selected was body-force-weighted, advised for VOF calculations. Second Order Upwind discretization was implemented to solve Momentum, Turbulent Kinetic Energy and Dissipation Rate. The Second Order Upwind is able to achieve more accurate results when the flow is not aligned with the mesh, especially on tetrahedrons mesh and for complex flows. The Spatial Discretization was based on the Least Square Cell Based gradient and the Compressive method was selected to solve the Volume Fraction equation.

Lastly, the Time Step Size was calculated for each simulation according to the mesh size and the maximum expected velocity that ensured Courant Number below one.

### **5.3 Mesh Generation of the PKW**

Once the geometric model was completed, several meshes were implemented using the ANSYS® Meshing™ to perform a sensitivity analysis that allowed to establish the mesh resolution representing the best trade-off between results and

computational times. The implemented mesh was diversified for each volume of fluid domain (Figure 5.5): volume 1 was set with a mesh size equal to 2.5 cm (~4.8% P), volume 2 with 5 cm (~9.6% P) and volume 6 was set with a mesh equal to 5 cm (~9.6% P) with an inflation refinement corresponding to the bottom of the channel with a mesh size resolution variable. In addition, four levels of mesh resolution were evaluated, by varying the number of elements for the block domains surrounding the PKW, namely volume 3, volume 4 and volume 5.

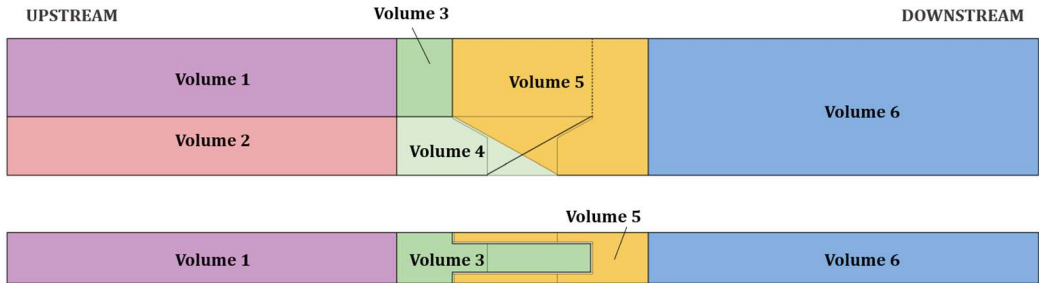


**Fig. 5.5 Specific volumes implemented in the ANSYS® model.**

The mesh resolutions tested were selected with the purpose to accomplish Mesh Convergence. The procedure was based on the calculation of the Grid Convergence Index, following Celik et al. (Celik *et al.*, 2008) methodology, where GCI can be defined as:

$$GCI^{21} = \frac{1.25e_a^{21}}{r_{21} - 1} \quad (5.1)$$

where  $e_a^{21}$  is the approximate relative error [-] and  $r_{21}$  is the refinement factor [-], calculated respectively as:

$$e_a^{21} = \left| \frac{\phi_1 - \phi_2}{\phi_1} \right| \quad (5.2)$$

$$r = h_{coarse}/h_{fine} \quad (5.3)$$

where  $h$  define the representative grid size [m], which for three-dimensional calculations can be estimated as:

$$h = \left[ \frac{1}{N} \sum_{i=1}^N (\Delta V_i) \right]^{1/3} \quad (5.4)$$

where  $\Delta V_i$  is the volume of the  $i$ th cell [m<sup>3</sup>] and  $N$  is the number of cells used for the computations. The mesh sizes selected respected the recommended  $r \geq 1.3$ . In greater detail, the specific mesh size for volumes 3, 4 and 5, as well as the inflation factor for volume 6 are summarized in Table 5.2, with the total number of cells for each mesh and the computational time required to achieve time convergence.

Mesh	Volume size [cm]				Number of cells	Computational time [days]
	3	4	5	6		
<b>h<sub>1</sub></b>	2.00	3.00	2.00	inflation of 2.00	696,799	~ 4
<b>h<sub>2</sub></b>	1.50	2.00	1.50	inflation of 1.50	1,521,601	~ 10
<b>h<sub>3</sub></b>	1.15	1.30	1.15	inflation of 1.15	3,569,820	~ 25
<b>h<sub>4</sub></b>	0.80	1.00	0.80	inflation of 0.80	9,503,531	~ 40

**Tab. 5.2 Mesh resolutions tested for the Mesh Convergence Method.**

A value of  $GCI_{CPKW}^{21} = 0.53\%$  was achieved between mesh  $h_1$  and  $h_2$  in terms of discharge coefficient and values of  $GCI_{VX}^{21?} = 2.46\%$  for the inlet key velocities in the X-direction. Meshes  $h_3$  and  $h_4$  required a computational time too long whereas the GCI values obtained between meshes  $h_1$  and  $h_2$  are relatively small, therefore mesh  $h_1$  (Figures 5.6 and 5.7) was accounted for simulations.

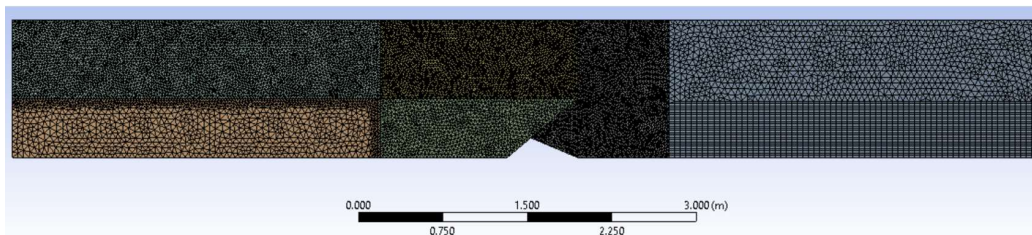


**Fig. 5.6 Mesh  $h_1$  implemented in the ANSYS® Meshing™.**

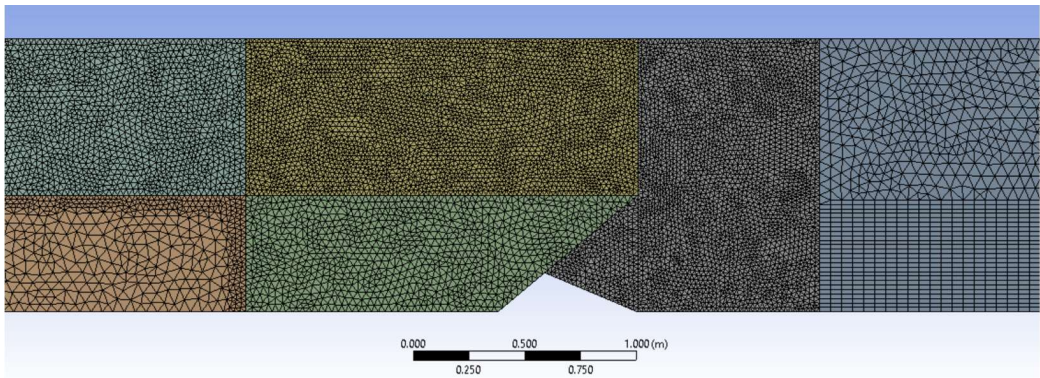


**Fig. 5.7** Zoom of the mesh  $h_1$  in the surrounding area of the PKW implemented in the ANSYS® Meshing™.

## References

- ANSYS Fluent 12.0 User's Guide. (2019).
- Celik, I. B., Ghia, U., Roache, P. J., Freitas, C. J., Coleman, H., & Raad, P. E. (2008). Procedure for estimation and reporting of uncertainty due to discretization in CFD applications. *Journal of Fluids Engineering, Transactions of the ASME*, 130(7), 0780011–0780014. <https://doi.org/10.1115/1.2960953>
- Cicero, G. M., & Delisle, J. R. (2013). Discharge characteristics of Piano Key weirs under submerged flow. *Labyrinth and Piano Key Weirs II – PKW 2013*, 101–109.
- Crookston, B. M., Anderson, R. M., & Tullis, B. P. (2018). Free-flow discharge estimation method for Piano Key weir geometries. *Journal of Hydro-Environment Research*. <https://doi.org/10.1016/j.jher.2017.10.003>
- Machiels, O. (2012). Experimental study of the hydraulic behaviour of Piano Key Weirs. University of Liège - Faculty of Applied Science.
- Noui, A., & Ouamane, A. (2011). Study of optimization of the Piano key weir. *Labyrinth and Piano Key Weirs - Proceedings of the International Conference on Labyrinth and Piano Key Weirs, PKW 2011*. <https://doi.org/10.1201/b12349-27>

---

## Chapter 6

### Experimental and Numerical Results and Discussion

---

In this Chapter, results from experimental tests presented in Chapter 4 and from the numerical model presented in Chapter 5 are given.

#### 6.1 Experimental results

The experimental tests were performed on the  $PKW_A$  and  $PKW_{A\_reverse}$ , and the flowrates tested and their corresponding H/P ratio values are presented in Table 6.1.

$PKW_A$	$H/P [-]$	0.059	0.067	0.073	0.082	0.088	0.094
	$Flowrate [L s^{-1}]$	30.75	34.66	40.85	45.12	50.03	55.41
	$H/P [-]$	0.101	0.109	0.116	0.125	0.131	
	$Flowrate [L s^{-1}]$	59.76	64.85	69.56	74.87	80.25	
$PKW_{A\_reverse}$	$H/P [-]$	0.067	0.077	0.087	0.091	0.101	0.114
	$Flowrate [L s^{-1}]$	30.91	35.41	40.85	45.12	50.03	56.01
	$H/P [-]$	0.122	0.132	0.139	0.144		
	$Flowrate [L s^{-1}]$	59.75	64.84	69.56	75.56		

**Tab. 6.1** Flowrates and dimensionless H/P ratios tested for  $PKW_A$  and  $PKW_{A\_reverse}$

---

The non-dimensional rating curves  $C_{PKW}(H/P)$  of the  $PKW_A$  and  $PKW_{A\_reverse}$ , from the experimental tests are given in Figure 6.1, with error bars showing the measurement uncertainties, calculated following the procedure of Section 4.2. As expected, the discharge coefficient decreases with increasing upstream head. The results showed that the loss in efficiency for both geometries is similar, however, the  $PKW_A$ , with  $W_i > W_o$ , is about 20% more efficient than the  $PKW_{A\_reverse}$ , with  $W_i < W_o$ . This decrease in efficiency lead to an increase of about 16% of the upstream head for same discharge values.

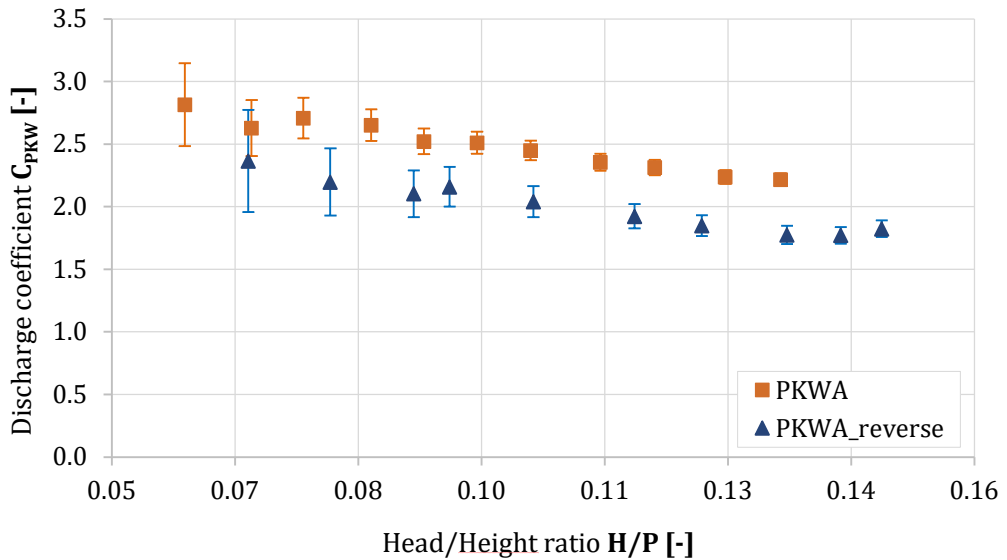


**Fig. 6.1** Experimental rating curves  $C_{PKW}(H/P)$  for  $PKW_A$  and  $PKW_{A\_reverse}$

Furthermore, following the procedure presented in Section 4.4, the velocity values, in  $m \cdot s^{-1}$ , was obtained for the streamwise (X-direction) in the A section, located in the middle of the inlet key, and in the B section, located 5 cm from the lateral wall of the PKW. The velocity values gathered from section A and section B are presented for the lower experimental tested range of flowrates ( $30.75 L s^{-1}$  –  $50.03 L s^{-1}$ ) in Figures 6.2 and 6.3, and for the higher tested range ( $55.41 s^{-1}$  –  $80.25 L s^{-1}$ ) in Figures 6.4 and 6.5.

Results show that velocities increase when increasing flowrates. Higher velocities can be observed in points P5 and lower velocities in point P9 at both

sections. Although both sections have quite similar velocity values, the middle section of the inlet key (Section A), show slightly greater values in all points less than in P8, in which Section B provides higher values.

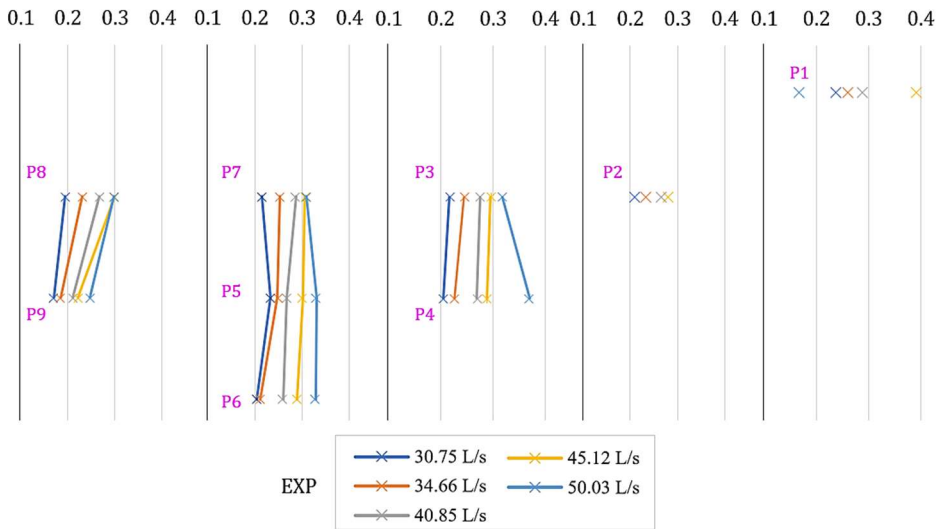


**Fig. 6.2 Velocity in the X-direction for lower flowrates at Section A for the PKWA**

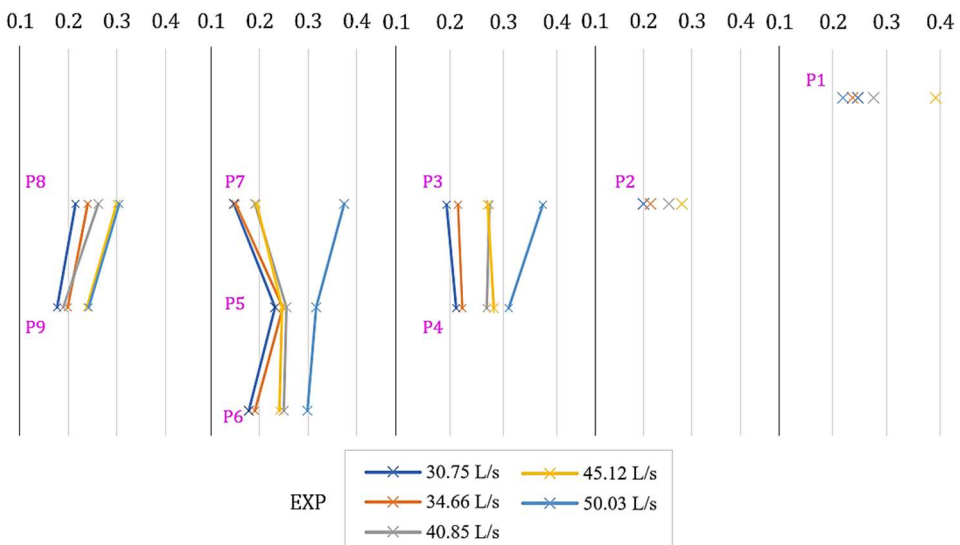


**Fig. 6.3 Velocity in the X-direction for lower flowrates at Section B for the PKWA**

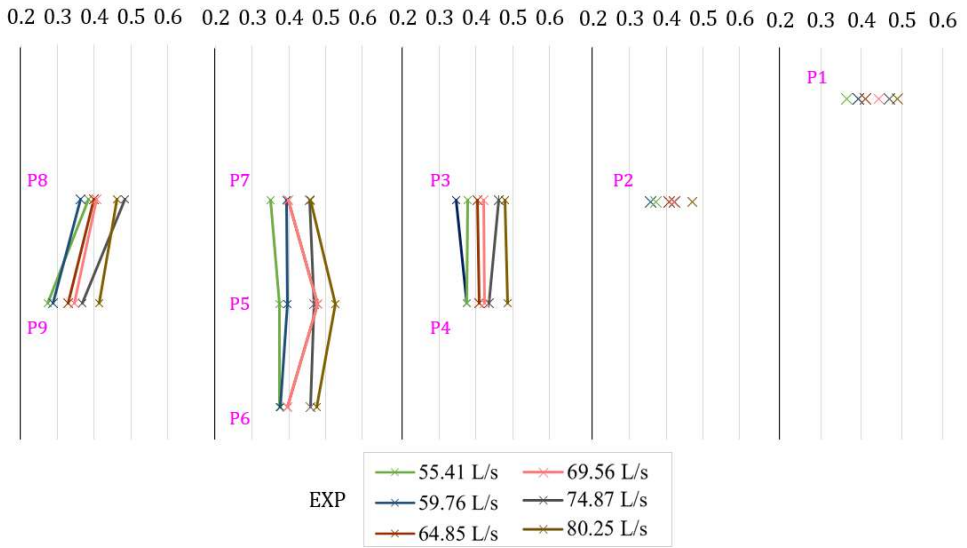


**Fig. 6.4 Velocity in the X-direction for higher flowrates at Section A for the PKWA**

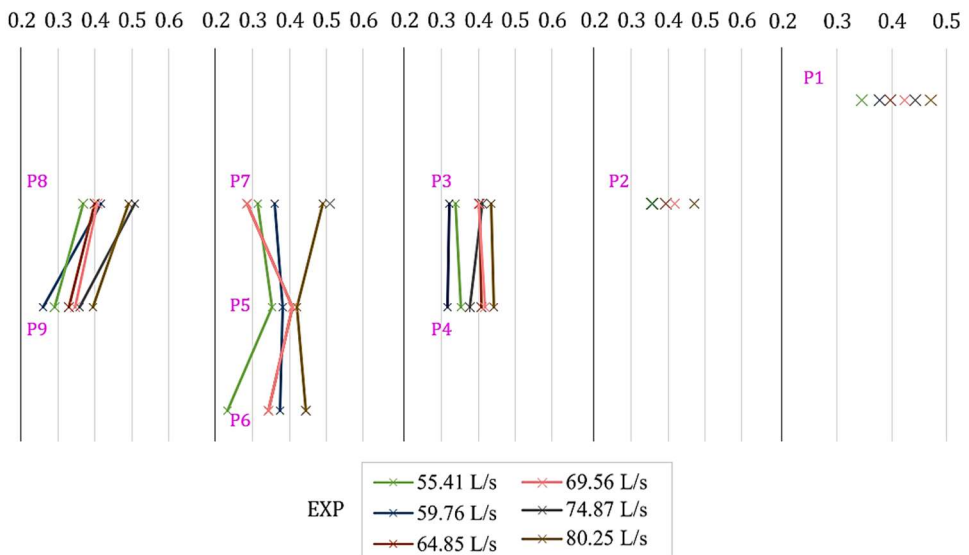


**Fig. 6.5 Velocity in the X-direction for higher flowrates at Section B for the PKWA**

## 6.2 CFD Simulation Results of PKW<sub>A</sub>, PKW<sub>A\_reverse</sub> and PKW<sub>B</sub> with ANSYS® Fluent™ Code.

### 6.2.1 Comparison between PKW<sub>A</sub> and PKW<sub>A\_reverse</sub> and CFD model validation

The discharge coefficient,  $C_{PKW}$ , for the numerical analysis has been calculated using Equation 4.8. The water level,  $h$ , and mean velocity,  $\bar{v}$ , have been estimated at a section located 50 cm upstream the PKW upstream crest, obtaining the upstream head,  $H$ , applying Equation 4.9.

The non-dimensional rating curves  $C_{PKW}(H/P)$  of the  $PKW_A$  and  $PKW_{A\_reverse}$ , from the experimental and numerical tests are given in Figure 6.6, with error bars showing the measurement uncertainties.

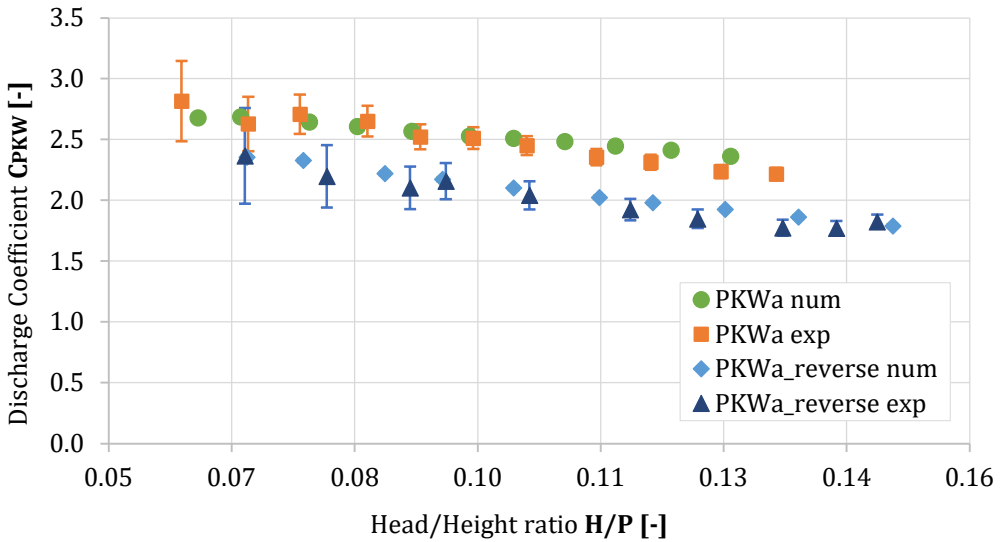


Fig. 6.6 Experimental and Numerical rating curves  $C_{PKW}(H/P)$  for PKW<sub>A</sub> and PKW<sub>A\_reverse</sub>

Results showed a good agreement between the numerical and experimental results for the discharge coefficient in both configurations, with relative errors presented in Table 6.2 for the  $PKW_A$  and  $PKW_{A\_reverse}$ , respectively, calculated as:

$$e_{r_{EXP-NUM}} = \frac{C_{PKWexp} - C_{PKWnum}}{C_{PKWexp}} \quad (6.1)$$

where  $C_{PK_{exp}}$  is the discharge coefficient obtained experimentally [-] and  $C_{PKW_{num}}$  corresponds to the discharge coefficient obtained from the CFD model.

	Q [L s <sup>-1</sup> ]	C <sub>PKW exp</sub> [-]	C <sub>PKW exp</sub> $\bar{U}$ [-]	C <sub>PKW num</sub> [-]	e <sub>r</sub> [%]
<b>PKW<sub>A</sub></b>	30.57	2.82	2.49 – 3.15	2.68	4.88%
	34.66	2.63	2.41 – 2.85	2.69	-2.18%
	40.85	2.71	2.55 – 2.87	2.65	2.29%
	46.93	2.65	2.53 – 2.78	2.61	1.62%
	50.03	2.52	2.42 – 2.63	2.57	-1.81%
	55.41	2.51	2.42 – 2.60	2.53	-0.75%
	59.75	2.45	2.37 – 2.57	2.51	-2.49%
	64.85	2.36	2.29 – 2.42	2.49	-5.52%
	69.56	2.31	2.25 – 2.38	2.45	-5.84%
	74.87	2.24	2.18 – 2.29	2.41	-7.81%
	80.25	2.22	2.17 – 2.27	2.37	-6.69%
<b>PKW<sub>A,reverse</sub></b>	30.91	2.37	1.97 – 2.76	2.36	0.49%
	35.41	2.20	1.94 – 2.46	2.33	-5.97%
	40.85	2.10	1.93 – 2.28	2.22	-5.58%
	45.12	2.16	2.01 – 2.31	2.17	-0.69%
	50.03	2.04	1.93 – 2.16	2.10	-2.96%
	56.01	1.92	1.84 – 2.01	2.03	-5.23%
	59.75	1.85	1.77 – 1.93	1.98	-7.14%
	64.84	1.78	1.71 – 1.84	1.93	-8.53%
	69.56	1.77	1.71 – 1.83	1.86	-5.24%
	75.56	1.83	1.77 – 1.88	1.79	1.93%

**Tab. 6.2 Relative scatters between the numerical and experimental results for the discharge coefficient of the PKW<sub>A</sub> and the PKW<sub>A,reverse</sub>.**

To assess the reduction in efficiency of a wider range of H/P, higher flowrates were simulated. Figure 6.7 shows the comparison of the numerical results for the discharge coefficient for PKW<sub>A</sub> and PKW<sub>A,reverse</sub>. The PKW<sub>A</sub> discharge coefficient was between 12% and 34% higher leading an upstream head between 9.8% and 32% smaller, proving the relevant role of the  $W_i/W_o$  ratio in the discharge efficiency.

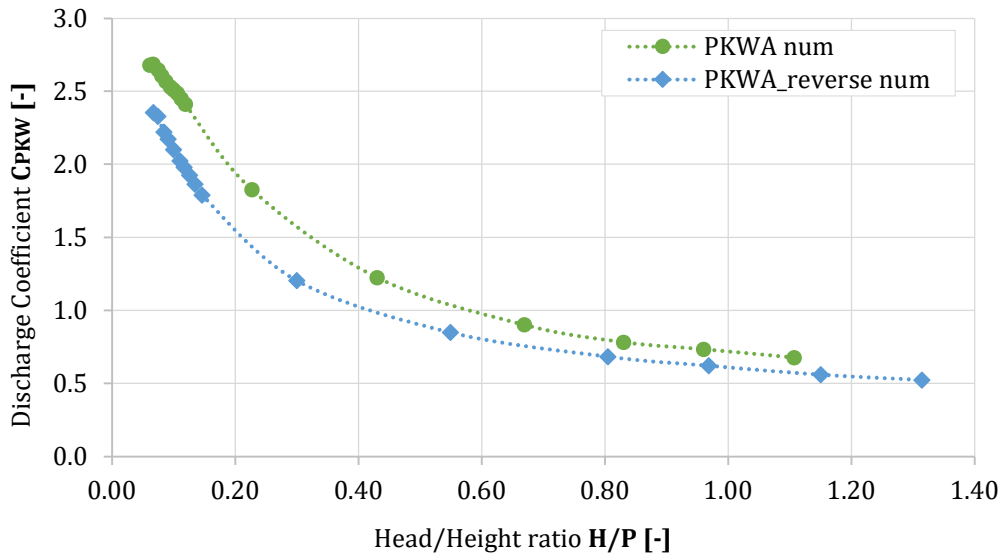


Fig. 6.7 Numerical rating curves  $C_{PKW}(H/P)$  for  $PKW_A$  and  $PKW_{A\_reverse}$

Aiming to validate the numerical results for the wider  $H/P$  range, the discharge coefficient was also computed using the equations from the literature reported in Chapter 2. Nevertheless, some dimensionless ratios from the implemented models were out of range of the limits of appliance for specific equations. Specifically, Machiels et al. (Machiels *et al.*, 2014) method set a  $L/W$  ratio equal to 5 whereas the simulated  $PKW_A$  and  $PKW_{A\_reverse}$   $L/W$  ratios were equal to 6.51. Kabiri-Samani and Javaheri (Kabiri-Samani and Javaheri, 2012) method proposed a suitable range of values for  $W_i/W_o$  from 0.33 to 1.2 which is exceeded by the  $PKW_A$ , settling a value for  $W_i/W_o$  equal to 1.5. Likewise, all methods can be applied just for  $H/P$  values bigger than 0.1, establishing an underneath limit, which was considered for the numerical computed  $C_{PKW}$  values presented in Figures 6.8 and 6.9 for the  $PKW_A$ , and  $PKW_{A\_reverse}$ , respectively.

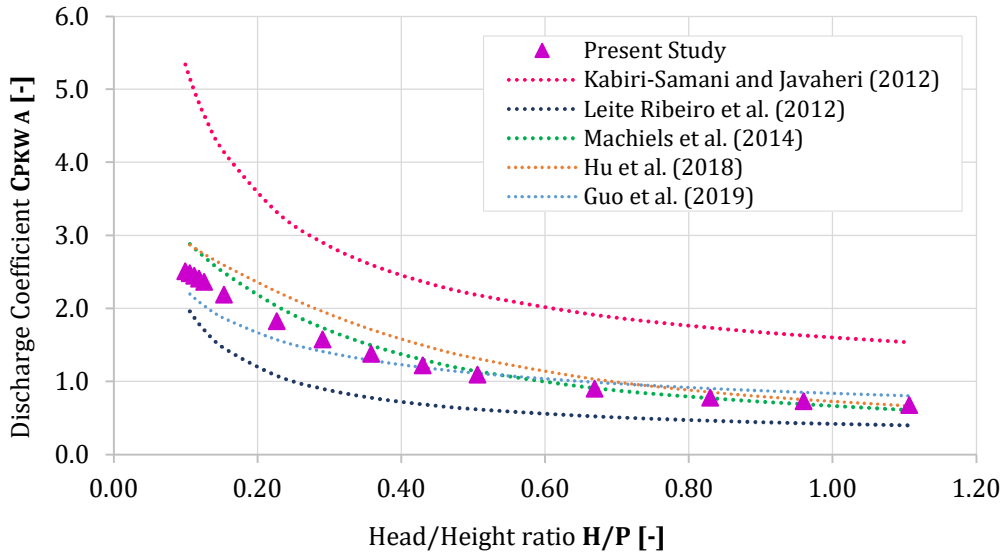


Fig. 6.8 Analytical equations for the discharge coefficient  $C_{PKW}$  ( $H/P$ ) curves for  $PKW_A$ .

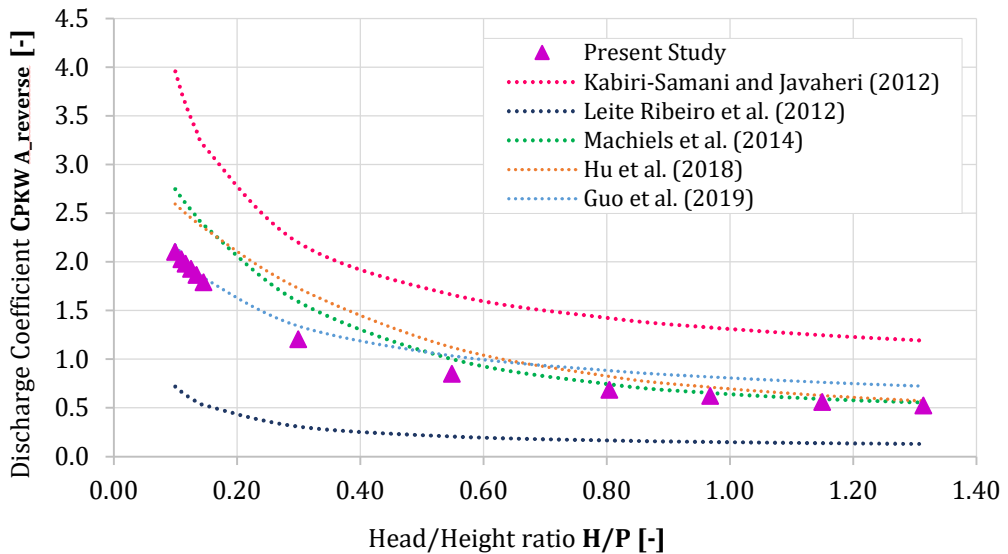


Fig. 6.9 Analytical equations for the discharge coefficient  $C_{PKW}$  ( $H/P$ ) curves for  $PKW_{A\_reverse}$ .

The results showed a good agreement with the equations by Machiels et al. (Machiels *et al.*, 2014), Hu et al. (Hu *et al.*, 2018) and Guo et al. (Guo *et al.*, 2019). Leite Ribeiro et al. (Ribeiro *et al.*, 2012) equation presented higher discrepancy and the equation proposed by Kabiri-Samani e Javaheri (Kabiri-Samani and Javaheri,

2012) showed no general correspondence for either configuration, with  $C_{PKW}$  values much higher than the observed numerical results. The relative error was calculated as:

$$e_r = \frac{C_{PKW_{EQ}} - C_{PKW}}{C_{PKW}} \quad (6.2)$$

where  $C_{PKW_{EQ}}$  is the discharge coefficient obtained using the presented equations [-] and  $C_{PKW}$  is the discharge coefficient obtained from the CFD model. The relative error was computed for each equation and both configurations, and the obtained minimum and maximum relative errors are presented in Table 6.3. An overall better congruity for the  $PKW_A$  results was observed.

Author's equation	$PKW_A$		$PKW_{A,reverse}$	
	$e_{r_{min}}$ [%]	$e_{r_{max}}$ [%]	$e_{r_{min}}$ [%]	$e_{r_{max}}$ [%]
Leite Ribeiro et al. (2012)	17.92	43.96	65.75	75.70
Kabiri-Samani and Javaheri (2012)	81.59	126.54	78.50	127.46
Machiels et al. (2014)	0.78	17.08	5.34	32.97
Hu et al. (2018)	1.82	24.20	9.08	43.51
Guo et al. (2019)	1.46	18.53	1.81	38.094

**Tab. 6.3 Minimum and maximum relative errors between author's equations and numerical results for the  $PKW_A$  and  $PKW_{A,reverse}$**

To validate the CFD model in terms of upstream velocity, a comparison between the experimental and numerical data was computed for the inlet key of the  $PKW_A$  at sections A and B (Figure 4.9). The experimental values were taken using the ADV as mentioned in Section 4. The velocity values, in  $m \cdot s^{-1}$ , obtained for the streamwise (X-direction) in the A section, located in the middle of the inlet key, are shown in 6.10 and 6.11. Higher velocities can be observed in the upper points P1, P2, P3, P7 and P8 for the velocities obtained with the numerical model. Moreover, the numerical obtained velocities increase when moving downstream the PKW, achieving the maximum value in the point located close to the downstream crest, P1. Likewise, the X-direction velocities gathered from the B section are shown in

Figures 6.12 and 6.13. As observed for section A, the numerical velocities are higher when moving up and towards the downstream crest. Although both sections have quite similar velocity values, the middle section of the inlet key (Section A), present slightly greater values. The velocity distribution of the results agree with those presented by Machiels (Machiels, 2012) and Denys and Basson (Denys and Basson, 2020), where the velocity increased in the middle of the inlet key and the closer the measurement point from the downstream crest, the higher the velocity.

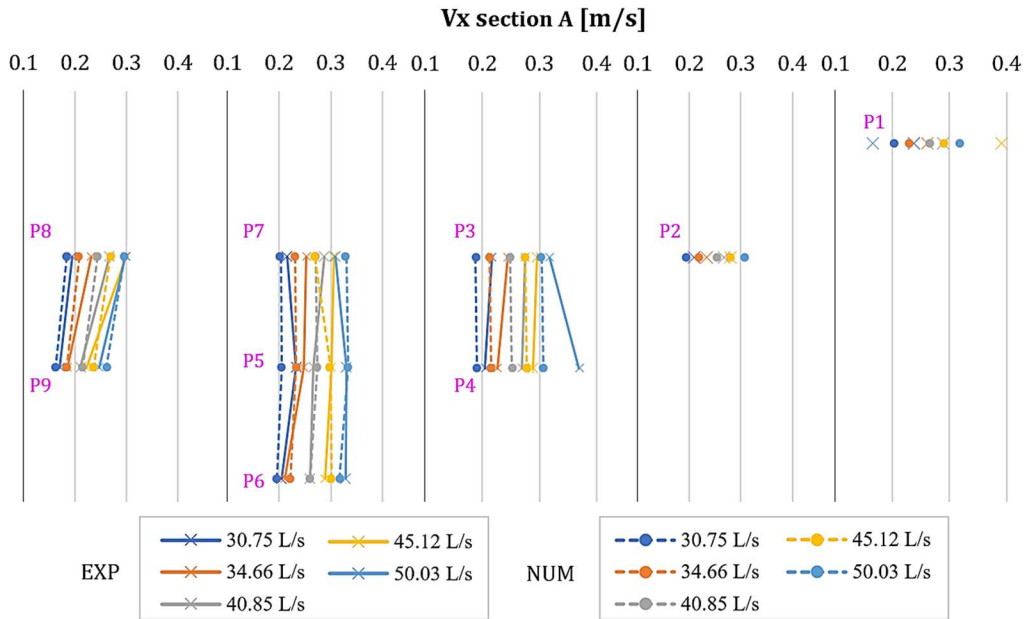


**Fig. 6.10 Comparison of velocities in the X-direction for lower flowrates at Section A for the PKW<sub>A</sub>.**

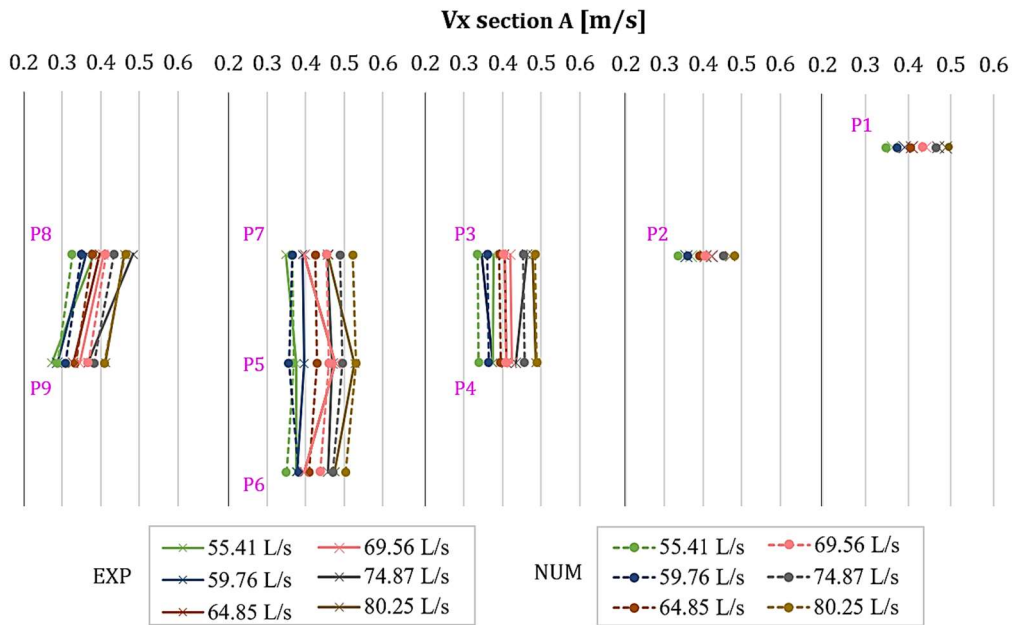


**Fig. 6.11 Comparison of velocities in the X-direction for higher flowrates at Section A for the PKWA.**

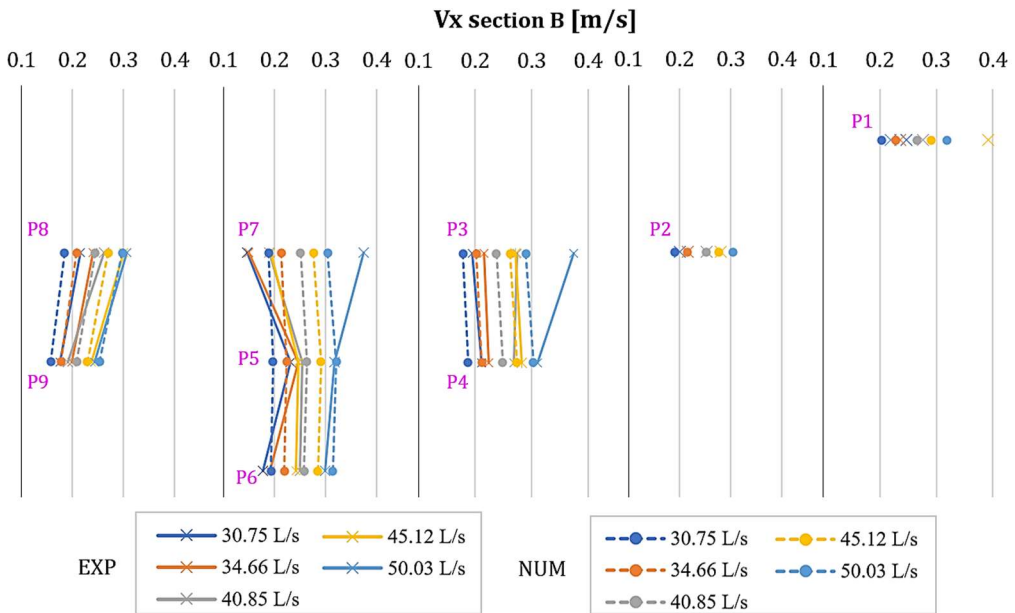


**Fig. 6.12 Comparison of velocities in the X-direction for lower flowrates at Section B for the PKWA.**

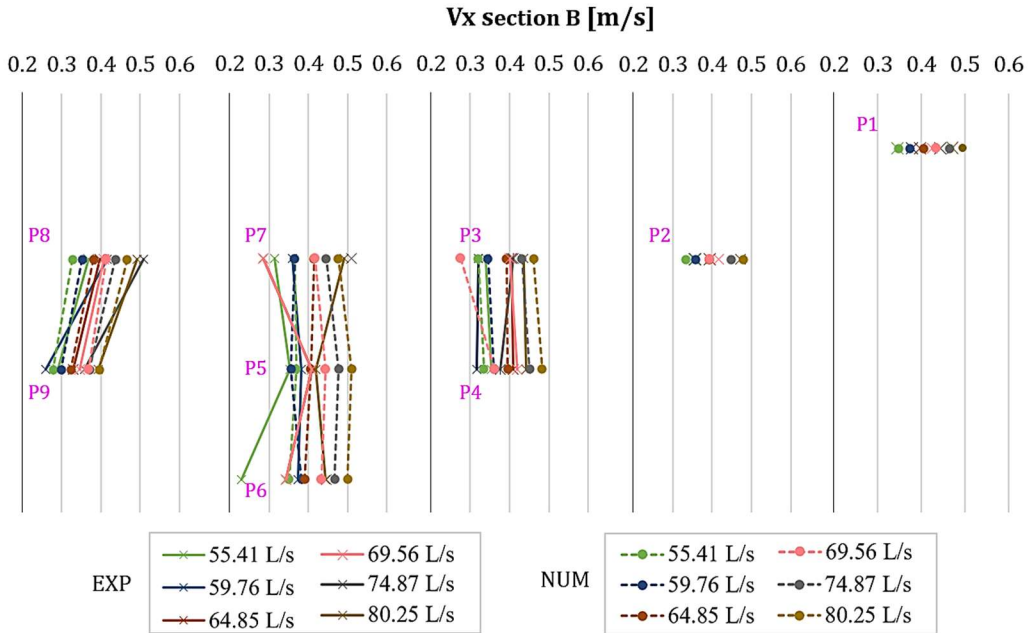


**Fig. 6.13 Comparison of velocities in the X-direction for higher flowrates at Section B for the PKW<sub>A</sub>.**

The minimum, maximum and average relative errors between experimental and numerical data are presented in Table 6.4 for each measurement point. Results shows a good agreement, especially for section A, with most of the average relative errors below 7%. Section B shows higher discrepancies in points P3, P6 and P7. These discrepancies can be explained for the experimental measurements due to the closer location of the ADV to the lateral wall and the random error committed while taking and post-processing the gathered data.

		1	2	3	4	5	6	7	8	9
<b>Section A</b>	$e_{r,min}$ [%]	0.7	0.5	1.3	0.5	0.0	0.2	0.1	0.6	0.7
	$e_{r,max}$ [%]	92.8	7.7	18.1	17.1	12.2	10.9	14.6	14.7	16.1
	$\bar{e}_r$ [%]	15.1	4.3	6.8	5.4	4.2	3.8	7.0	7.0	5.0
<b>Section B</b>	$e_{r,min}$ [%]	0.6	0.1	0.4	0.1	0.3	3.2	2.2	1.6	0.7
	$e_{r,max}$ [%]	45.1	77.4	56.5	19.7	18.1	51.0	45.7	21.1	10.7
	$\bar{e}_r$ [%]	10.1	11.3	14.4	6.8	8.5	21.5	27.0	8.9	5.8

**Tab. 6.4 Minimum, maximum and average relative errors of velocity experimental and numerical results for the PKW<sub>A</sub> at sections A and B**

After assessing the discharge coefficient and the velocity field for the  $PKW_A$  and  $PKW_{A\_reverse}$ , it was observed that the numerical model was able to reproduce the experimental model with an average relative error of 4.08% and 9.6% in terms of the discharge coefficient and velocity values, respectively.

### 6.2.2 Comparison between $PKW_A$ and $PKW_B$ models

The discharge coefficient of the  $PKW_B$  for several flowrates were computed, resulting in the rating curve  $C_{PKW}(H/P)$  presented in Figure 6.14, along with the discharge coefficient computed for the  $PKW_A$ . The discharge coefficient varied from 2.68 to 0.68 for a range of  $H/P$  from 0.06 to 1.11 for the  $PKW_A$  and 2.86 to 0.63 for a range of  $H/P$  from 0.08 to 1.16 for the  $PKW_B$ . This means that for lower head,  $PKW_B$  is more efficient than  $PKW_A$ , however, for increasing head,  $PKW_A$  turned to be more efficient. This change in efficiency occurred at  $H/P \approx 0.3$ , when  $PKW_B$  discharge coefficient decreases more rapidly than the corresponding discharge coefficient from  $PKW_A$ . Therefore, for  $0 \lesssim H/P \lesssim 0.3$ ,  $C_{PKW\_B} \geq C_{PKW\_A}$ , and for  $H/P \gtrsim 0.3$ ,  $C_{PKW\_A} \geq C_{PKW\_B}$ . These results follow those presented by Machiels et al. (Olivier Machiels *et al.*, 2014), which showed that for higher head, type B started to be less efficient than type A.

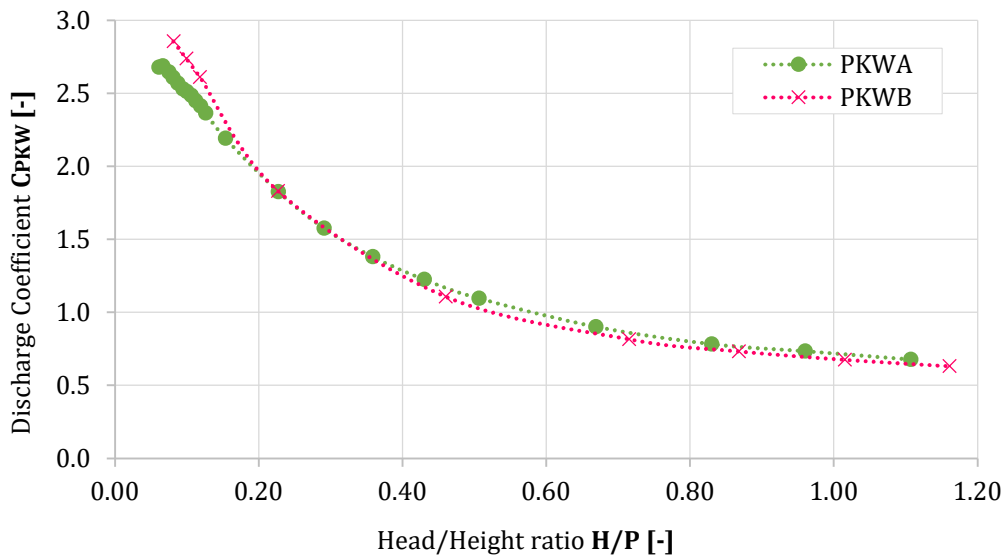


**Fig. 6.14 Numerical rating curves  $C_{PKW}$  (H/P) for  $PKW_A$  and  $PKW_B$** 

Table 6.5 presents the obtained results for the upstream head and the discharge coefficient for each flowrate tested. The difference of these hydraulic parameters is expressed using Equation 6.3:

$$\Delta_{A-B} = \frac{x_{PKW_A} - x_{PKW_B}}{x_{PKW_A}} \quad (6.3)$$

where  $x_{PKW_A}$  correspond to the obtained value for the  $PKW_A$  and  $x_{PKW_B}$  represents the corresponding value for the  $PKW_B$ . Results showed that the discharge coefficient of the  $PKW_B$  is up to  $\sim 11.2\%$  higher for lower head and up to  $\sim 9.5\%$  when the head increase. This variation in efficiency results in a greater upstream head up to  $\sim 6.8\%$  for the  $PKW_A$  at lower head and up to  $\sim 6.93\%$  for the  $PKW_B$  at higher head.

Flowrate [L s <sup>-1</sup> ]	H [cm]		$\Delta_{A-B}$ [%]	$C_{PKW}$ [-]		$\Delta_{A-B}$ [%]
	$PKW_A$	$PKW_B$		$PKW_A$	$PKW_B$	
50.03	4.54	4.23	6.80	2.57	2.86	-11.16
64.85	5.51	5.17	6.20	2.49	2.74	-10.09
80.25	6.57	6.15	6.38	2.37	2.61	-10.41
150	11.84	11.83	0.12	1.83	1.83	-0.20
262.5	26.41	23.99	-6.93	1.23	1.11	9.54
375	34.91	37.32	-6.92	0.90	0.82	9.54
450	43.32	45.28	-4.53	0.78	0.73	6.41
525	50.09	52.97	-5.75	0.73	0.68	8.02

**Tab. 6.5 Upstream head and discharge coefficient comparison between the  $PKW_A$  and the  $PKW_B$ .**

The discharge coefficient was also computed for the  $PKW_B$  using the equations from the literature and results are presented in Figure 6.15. In terms of limits of appliance, the L/W ratio of the  $PKW_B$  is equal to 6.51 and Bi/Bo ratio equal to 0, whereas Machiels et al. (Machiels *et al.*, 2014) limits L/W=5. Likewise, Leite Ribeiro et al. (Ribeiro *et al.*, 2012) limits the Bi/Bo ratio from 0.2 to 0.4. The Wi/Wo ratio is equal to 1.5 for the  $PKW_B$ , which exceeds the Wi/Wo range of Kabiri-Samani and Javaheri (Kabiri-Samani and Javaheri, 2012) from 0.33 to 1.2.

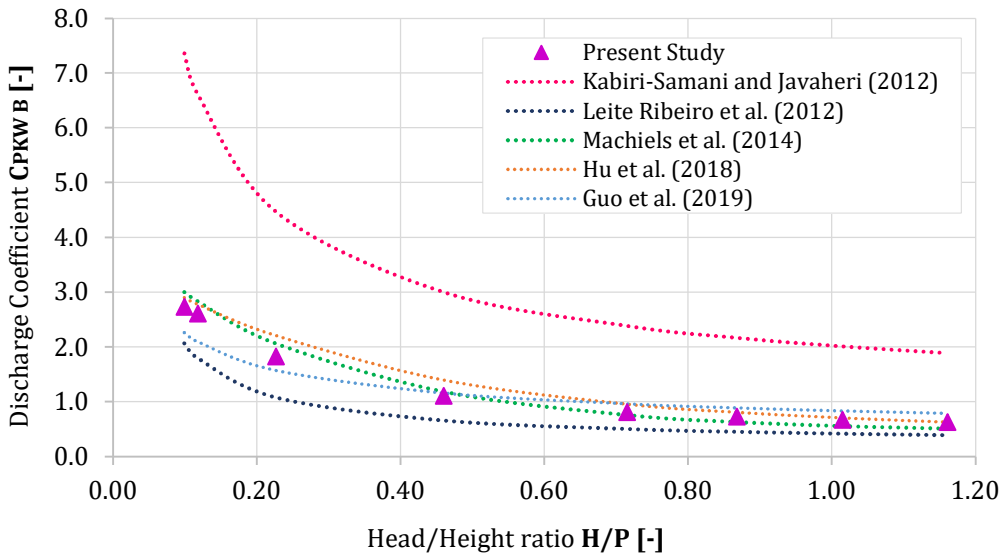


Fig. 6.15 Analytical equations for the discharge coefficient  $C_{PKW}$  ( $H/P$ ) curves for  $PKW_B$ .

Similar to  $PKW_A$  and  $PKW_{A\_reverse}$ , results showed a fairly good agreement with the equations by Machiels et al. (Machiels *et al.*, 2014), Hu et al. (Hu *et al.*, 2018) and Guo et al. (Guo *et al.*, 2019). Equation proposed by Leite Ribeiro et al. (Ribeiro *et al.*, 2012) showed less correspondence, whereas Kabiri-Samani e Javaheri (Kabiri-Samani and Javaheri, 2012) showed no general agreement, with much greater  $C_{PKW}$ . The relative error was calculated as Equation 6.2 and the minimum and maximum values are presented in Table 6.6.

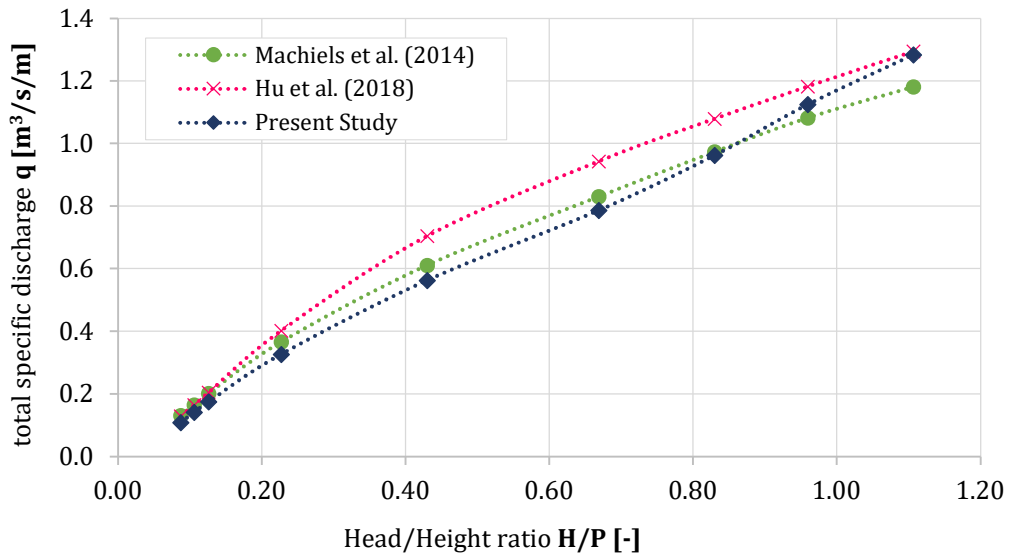
Author's equation	$PKW_B$	
	$e_{r\_min}$ [%]	$e_{r\_max}$ [%]
Leite Ribeiro et al. (2012)	24.52	41.10
Kabiri-Samani and Javaheri (2012)	144.16	199.10
Machiels et al. (2014)	6.85	19.24
Hu et al. (2018)	0.51	25.95
Guo et al. (2019)	4.55	24.86

Tab. 6.6 Minimum and maximum relative errors between author's equations and numerical results

### 6.2.3 Comparison between numerical results and Machiels et al. (2014) and Hu et al. (2018) equations

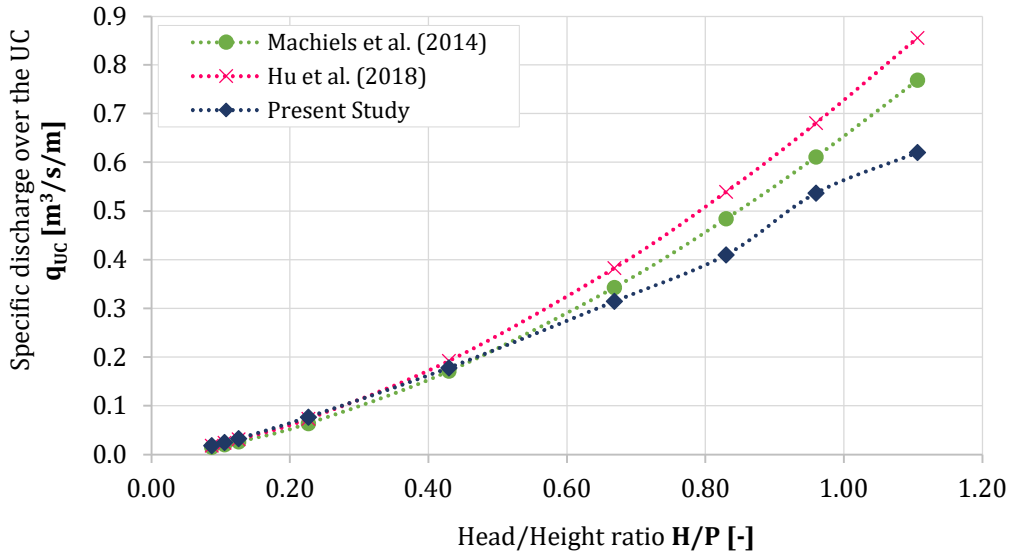
As aforementioned in Sections 6.2.1 and 6.2.2, the obtained numerical results for the discharge coefficient were close with the values obtained from Machiels et al. (Machiels *et al.*, 2014) and Hu et al. (Hu *et al.*, 2018). Indeed, the minimum and maximum relative errors for the  $PKW_A$  were 0.78% and 17.08% for Machiels et al. (Machiels *et al.*, 2014) and 1.82% and 24.20% for Hu et al. (Hu *et al.*, 2018), whereas for the  $PKW_B$  were 6.85% and 19.24% for Machiels et al. (Machiels *et al.*, 2014) and 0.51% and 25.95% for Hu et al. (Hu *et al.*, 2018). Furthermore, as seen in Section 2.2.3, Machiels et al. (Machiels *et al.*, 2014) and Hu et al. (Hu *et al.*, 2018) equations allow to calculate the total specific discharge,  $q$ , which is employed to determine the discharge coefficient of PKWs. Both equations divide the total specific discharge in the specific discharge over the upstream, downstream, and lateral crests. Herein, a comparison of these specific discharges between the results obtained from the CFD model and those from the equations is carried out.

Figure 6.16 presents the comparison for the total specific discharge for the  $PKW_A$ . results show that Machiels et al. (Machiels *et al.*, 2014) and Hu et al. (Hu *et al.*, 2018) equations present the same tendency, while for the numerical results, there is a steeper slope for  $H/P \geq 0.8$ . Likewise, numerical results are closer to those from Machiels et al. (Machiels *et al.*, 2014) with a mean absolute percentage error, MAPE, of 10.16%, while for and Hu et al. (Hu *et al.*, 2018), the MAPE is 15.28%.



**Fig. 6.16 Comparison of the  $PKW_A$  total specific discharge between numerical results and those obtained by Machiels et al. (2014) and Hu et al. (2018)**

Moreover, Figures 6.17, 6.18 and 6.19 presents the comparison for the specific discharges over the upstream, downstream and lateral crests for the  $PKW_A$ , respectively. Regarding the upstream crest, the numerical results are smaller for the entire  $H/P$  range, and better corresponding to those obtained with Machiels et al. (Machiels *et al.*, 2014) equation. Numerical results for the downstream crest follow similar trend to Machiels et al. (Machiels *et al.*, 2014) but values are closer to those from Hu et al. (Hu *et al.*, 2018) equation. The major difference in tendency is showed for the lateral crests. For  $H/P \leq 0.7$ , the specific discharge increases, however, for  $H/P \geq 0.7$ , while the values from the CFD model keep growing, the values obtained from Hu et al. (Hu *et al.*, 2018) equation remained primarily constant and those from Machiels et al. (Machiels *et al.*, 2014) starts decreasing.



**Fig. 6.17** Comparison of the PKW<sub>A</sub> specific discharge over the upstream crest between numerical results and those obtained by Machiels et al. (2014) and Hu et al. (2018)

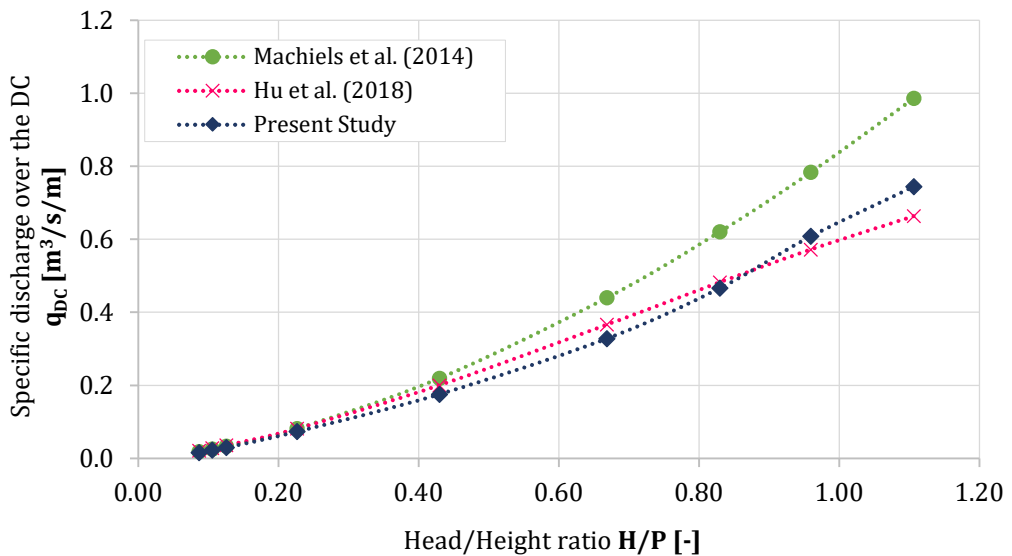


**Fig. 6.18** Comparison of the PKW<sub>A</sub> specific discharge over the downstream crest between numerical results and those obtained by Machiels et al. (2014) and Hu et al. (2018)

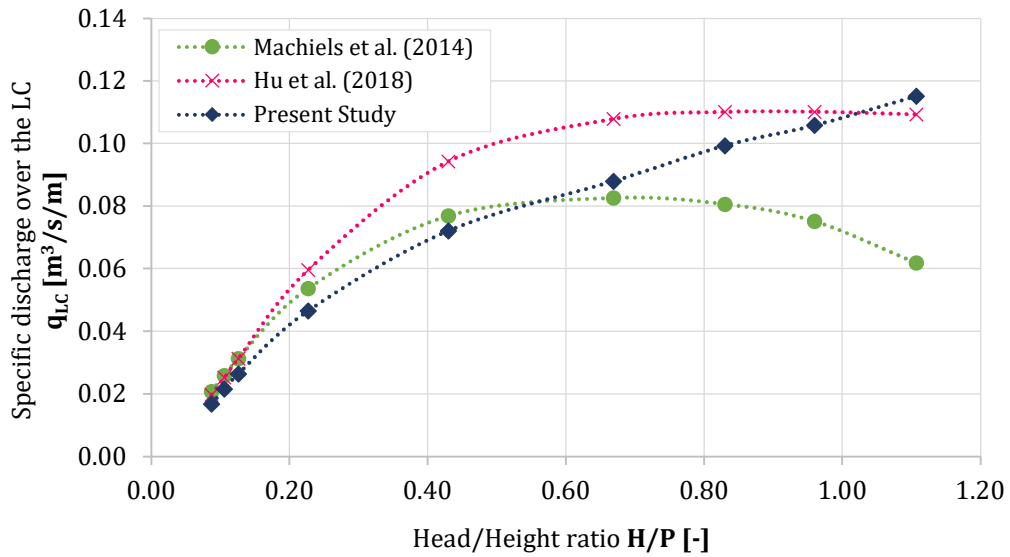


Fig. 6.19 Comparison of the PKW<sub>A</sub> specific discharge over the lateral crest between numerical results and those obtained by Machiels et al. (2014) and Hu et al. (2018)

Q [L s <sup>-1</sup> ]	H/P [-]	e <sub>q</sub> [%]	e <sub>q<sub>UC</sub></sub> [%]	e <sub>q<sub>DC</sub></sub> [%]	e <sub>q<sub>LC</sub></sub> [%]
50.03	0.087	-20.48	18.33	-16.02	-23.86
64.85	0.106	-16.8	19.90	-12.50	-20.29
80.25	0.126	-15.13	19.97	-11.83	-18.48
150	0.227	-12.03	16.98	-11.43	-15.39
262.5	0.430	-8.56	3.96	-24.84	-6.62
375	0.669	-5.56	-9.13	-34.03	6.11
450	0.830	-1.15	-18.04	-33.06	18.83
525	0.960	3.79	-13.87	-28.86	28.96
600	1.107	7.98	-23.94	-32.41	46.23
<b>MAPE [%]</b>		10.16	16.01	22.78	20.53

Tab. 6.7 Relative errors and MAPE of the PKW<sub>A</sub> specific discharges between numerical results and those obtained by Machiels et al. (2014)

Q [L s <sup>-1</sup> ]	H/P [-]	$e_q$ [%]	$e_{q_{UC}}$ [%]	$e_{q_{DC}}$ [%]	$e_{q_{LC}}$ [%]
50.03	0.087	-18.15	-1.22	-31.38	-18.08
64.85	0.106	-16.37	2.82	-23.82	-17.09
80.25	0.126	-16.84	4.49	-20.21	-18.25
150	0.227	-23.07	4.67	-11.2	-28.10
262.5	0.430	-25.12	-7.91	-14.02	-30.77
375	0.669	-19.92	-21.78	-11.62	-22.62
450	0.830	-12.12	-31.51	-3.44	-10.83
525	0.960	-5.12	-26.79	5.92	-4.13
600	1.107	-0.84	-37.96	10.86	5.03
<b>MAPE [%]</b>		15.28	15.46	14.72	17.21

**Tab. 6.8** Relative errors and MAPE of the  $PKW_A$  specific discharges between numerical results and those obtained Hu et al. (2018)

Regarding the  $PKW_B$ , Figure 6.20 shows the results of the total specific discharge. It can be observed a similar trend as for the  $PKW_A$ . Numerical results are comparable to those from Machiels et al. (Machiels *et al.*, 2014) for  $H/P \leq 0.8$ , while for  $H/P \geq 0.8$ , numerical results are closer to those obtained with Hu et al. (Hu *et al.*, 2018) equation, as seen also in the results gathered in Tables 6.9 and 6.10.

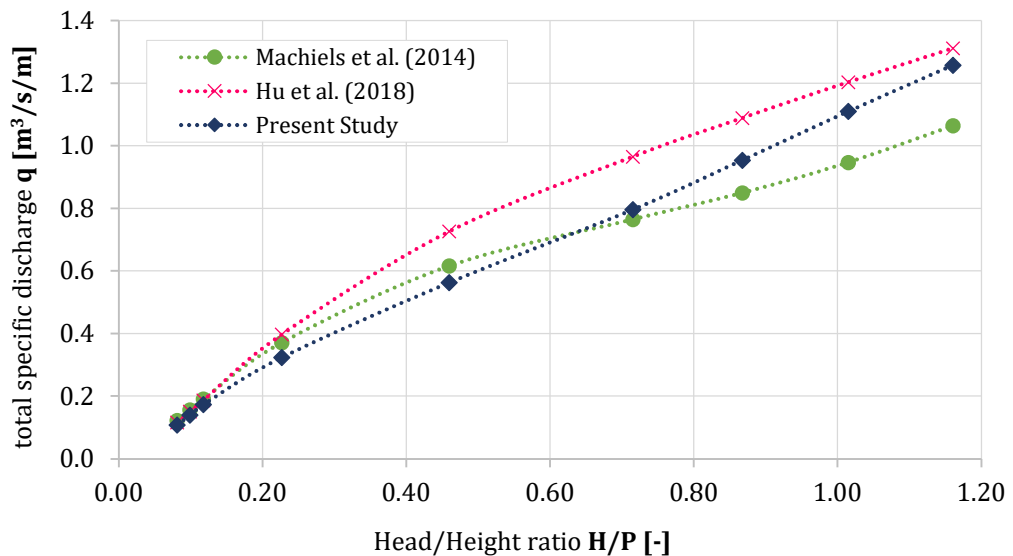


**Fig. 6.20** Comparison of the  $PKW_B$  total specific discharge between numerical results and those obtained by Machiels et al. (2014) and Hu et al. (2018)

Figures 6.21, 6.22 and 6.23 show the comparison for the specific discharges over the upstream, downstream, and lateral crests for the  $PKW_B$ , respectively. The tendency of the specific discharge for the upstream and downstream crests better correspond to the results obtained with Hu et al. (Hu *et al.*, 2018) equation. In terms of the lateral crest, results are also similar to those obtained for the  $PKW_A$ . For  $H/P \leq 0.45$ , the specific discharge from all models increases, whereas for  $H/P \geq 0.45$  the values from the present study increase, the values obtained from Hu et al. (Hu *et al.*, 2018) equation remained predominantly constant and in those from Machiels et al. (Machiels *et al.*, 2014), the decrease is more pronounced than in the  $PKW_A$  case.

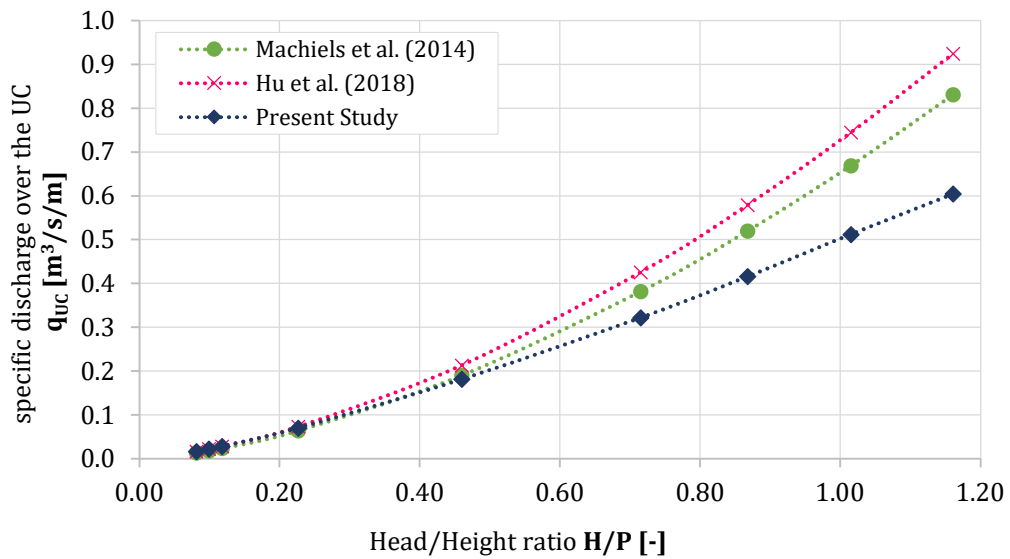


Fig. 6.21 Comparison of the  $PKW_B$  specific discharge over the UC between numerical results and those obtained by Machiels et al. (2014) and Hu et al. (2018)

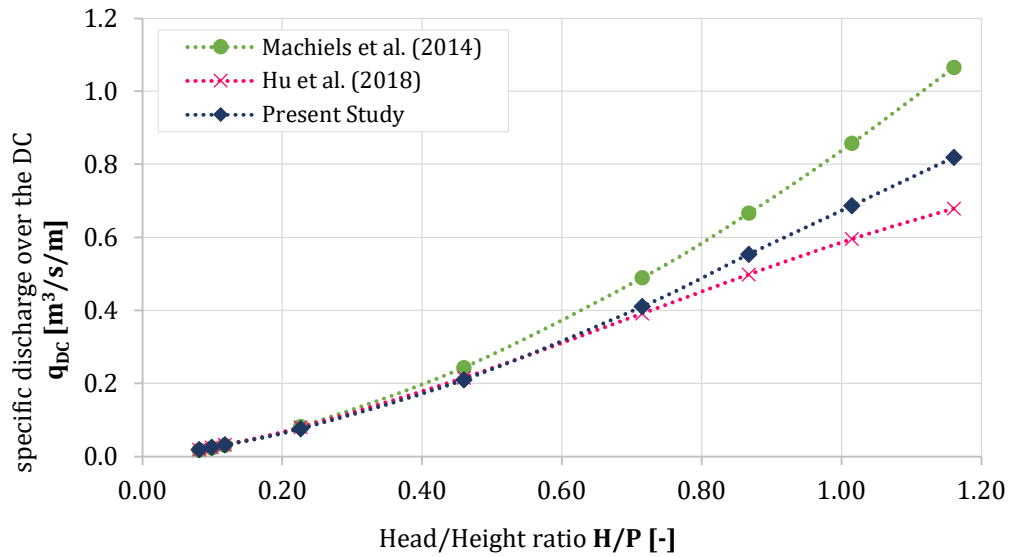


Fig. 6.22 Comparison of the PKW<sub>B</sub> specific discharge over the DC between numerical results and those obtained by Machiels et al. (2014) and Hu et al. (2018)

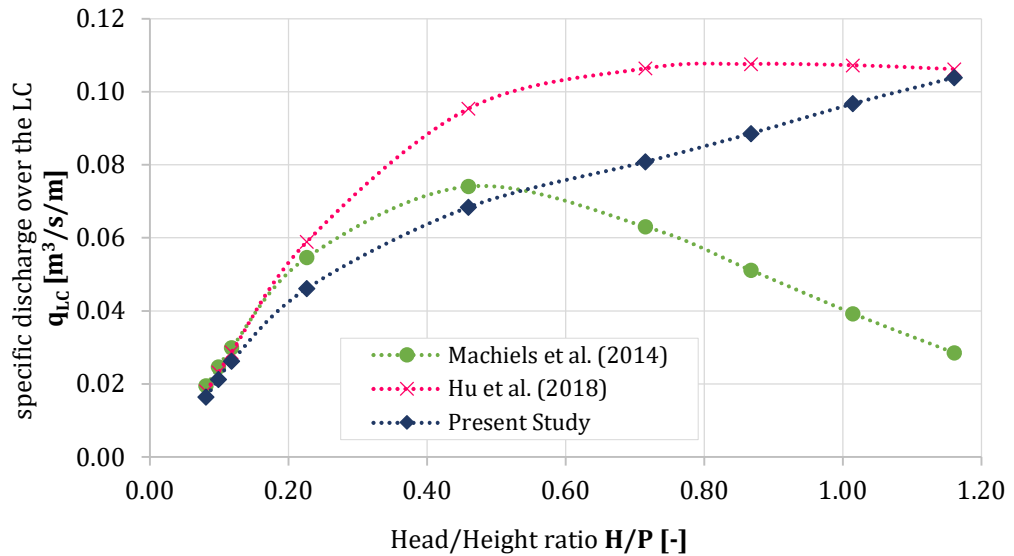


Fig. 6.23 Comparison of the PKW<sub>B</sub> specific discharge over the LC between numerical results and those obtained by Machiels et al. (2014) and Hu et al. (2018)

$Q$ [ $L s^{-1}$ ]	$H/P$ [-]	$e_q$ [%]	$e_{q_{UC}}$ [%]	$e_{q_{DC}}$ [%]	$e_{q_{LC}}$ [%]
50.03	0.087	-13.27%	18.16%	9.68%	-18.18%
64.85	0.106	-11.46%	18.19%	7.67%	-15.94%
80.25	0.126	-10.14%	16.67%	4.97%	-14.02%
150	0.227	-14.64%	9.04%	-7.28%	-18.33%
262.5	0.430	-9.46%	-4.75%	-15.91%	-8.29%
375	0.669	3.92%	-18.52%	-19.20%	21.94%
450	0.830	10.96%	-24.96%	-20.36%	42.29%
525	0.960	14.66%	-30.57%	-24.87%	59.41%
600	1.107	15.36%	-37.44%	-29.96%	72.53%
<b>MAPE [%]</b>		11.54	19.81	15.54	30.10

**Tab. 6.9** Relative errors of the  $PKW_B$  specific discharges between numerical results and those obtained by Machiels et al. (2014)

$Q$ [ $L s^{-1}$ ]	$H/P$ [-]	$e_q$ [%]	$e_{q_{UC}}$ [%]	$e_{q_{DC}}$ [%]	$e_{q_{LC}}$ [%]
50.03	0.087	-8.24%	-2.32%	-1.26%	-9.49%
64.85	0.106	-7.67%	0.10%	-0.43%	-9.12%
80.25	0.126	-8.05%	-0.03%	-0.91%	-9.54%
150	0.227	-22.79%	-4.44%	-4.92%	-27.71%
262.5	0.430	-29.05%	-17.53%	-2.50%	-39.44%
375	0.669	-21.25%	-32.18%	4.60%	-31.66%
450	0.830	-14.13%	-39.19%	9.95%	-21.46%
525	0.960	-8.44%	-45.36%	13.28%	-10.86%
600	1.107	-4.29%	-52.99%	17.08%	-2.23%
<b>MAPE [%]</b>		13.77	21.57	6.10	17.95

**Tab. 6.10** Relative errors of the  $PKW_B$  specific discharges between numerical results and those obtained Hu et al. (2018)

### 6.3 Discussion on the Discharge Coefficient of $PKW_A$ and $PKW_B$ .

For the purpose of assessing the variation in efficiency, the discharge for  $PKW_A$  and  $PKW_B$  over each single crest was computed. Figures 6.24 and 6.25 present the total discharge and the discharge ratio  $Q_B/Q_A$  for every crest. Results show that for  $H/P \lesssim 0.3$ , the upstream (UC), downstream (DC) and lateral crests (LC) of  $PKW_B$  are able to discharge more water than those from  $PKW_A$ . For  $0.3 \lesssim H/P \lesssim 0.8$ , the lateral and upstream crests of  $PKW_A$  discharge more water, while the discharge over the

downstream crest of  $PKW_B$  is higher. For all  $H/P$  values, lateral crests discharge majority of the flow, thus for a specific head value, the overall discharge mainly depends on the lateral crest discharge.

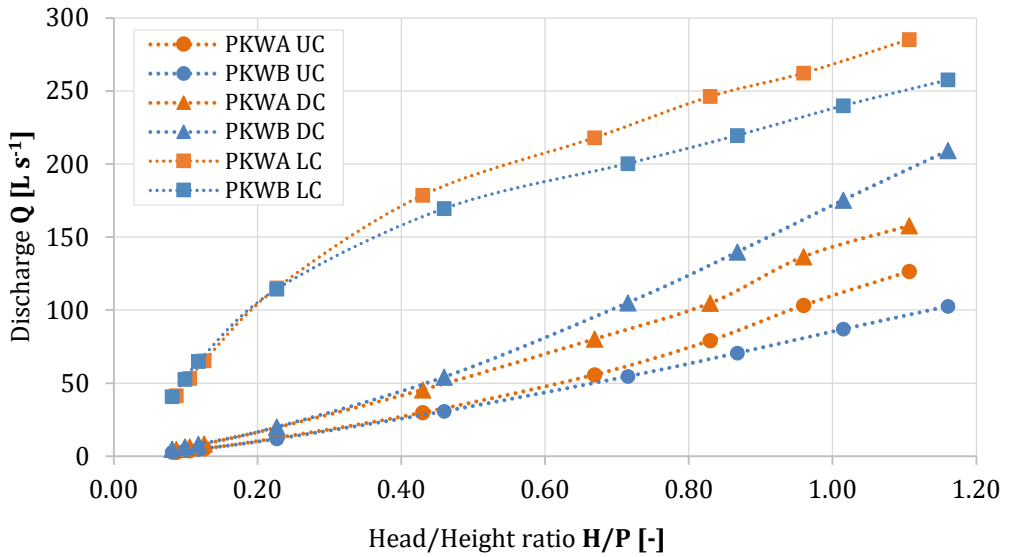


Fig. 6.24 Discharge over the upstream (UC), downstream (DC) and lateral crests (LC) of the  $PKW_A$  and  $PKW_B$

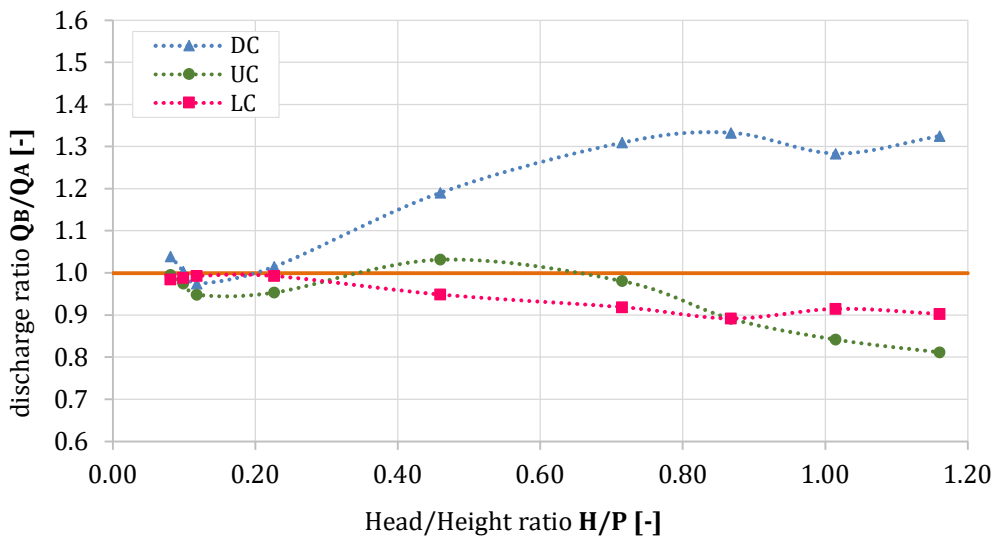


Fig. 6.25 Discharge ratio of the upstream (UC), downstream (DC) and lateral crests (LC) of the  $PKW_A$  and  $PKW_B$

In order to also assess the head distribution, the values of the water level and the kinetic term for the upstream, downstream and lateral crests have been estimated for both configurations and are presented in Figures 6.26, 6.27 and 6.28, respectively.

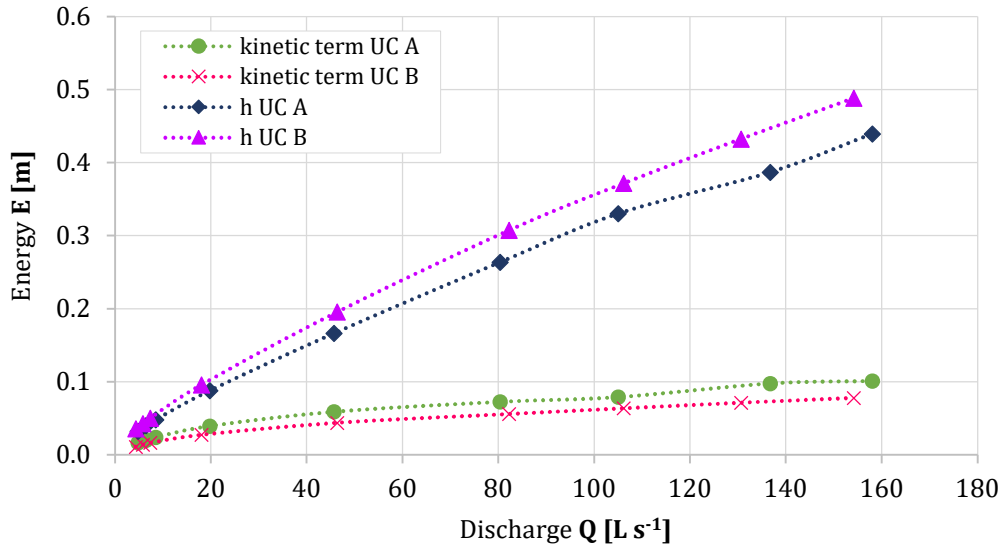


Fig. 6.26 Energy vs Discharge curves of the PKW<sub>A</sub> and PKW<sub>B</sub> from the upstream crest

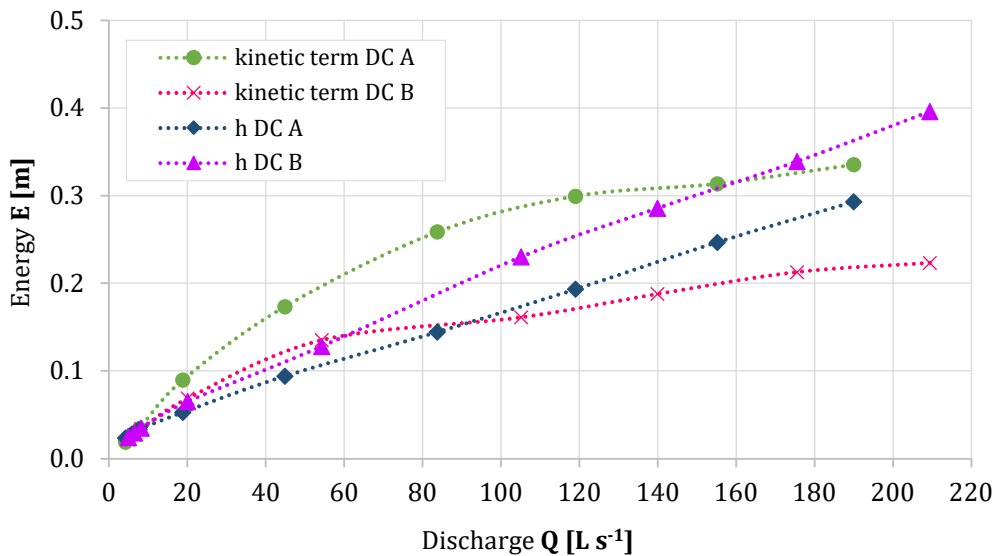
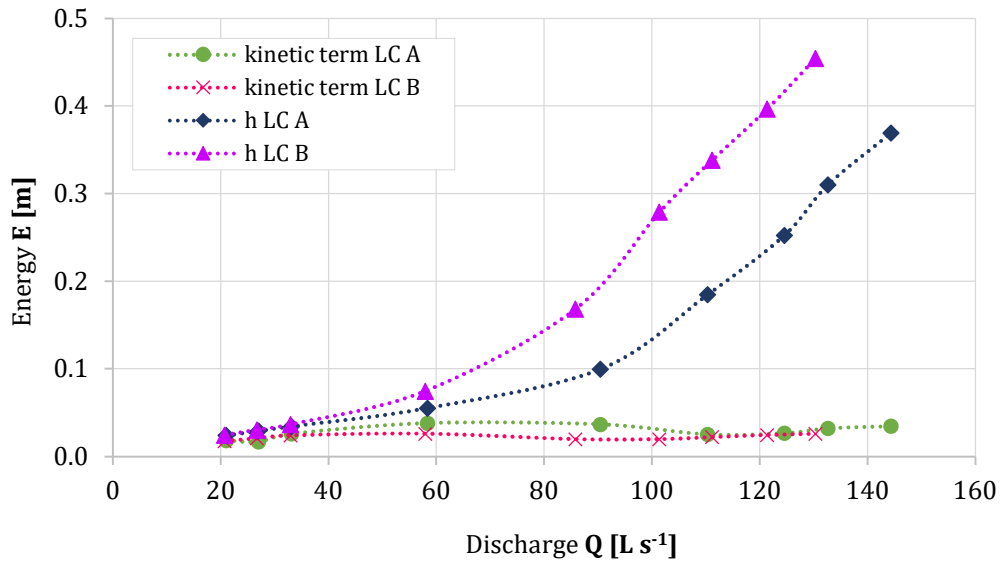


Fig. 6.27 Energy vs Discharge curves of the PKW<sub>A</sub> and PKW<sub>B</sub> from the downstream crest



**Fig. 6.28** Energy vs Discharge curves of the  $PKW_A$  and  $PKW_B$  from the lateral crests

The results show that for all the crests, the kinetic term of  $PKW_A$  is higher than the  $PKW_B$  one, while the water depth is higher on the  $PKW_B$ . The comparison of the total head between both configurations is shown in Figure 6.29 pointing out that the upstream head is very close in both configurations. Nevertheless, the downstream and lateral crests head values from the  $PKW_A$  are greater than the  $PKW_B$  ones.

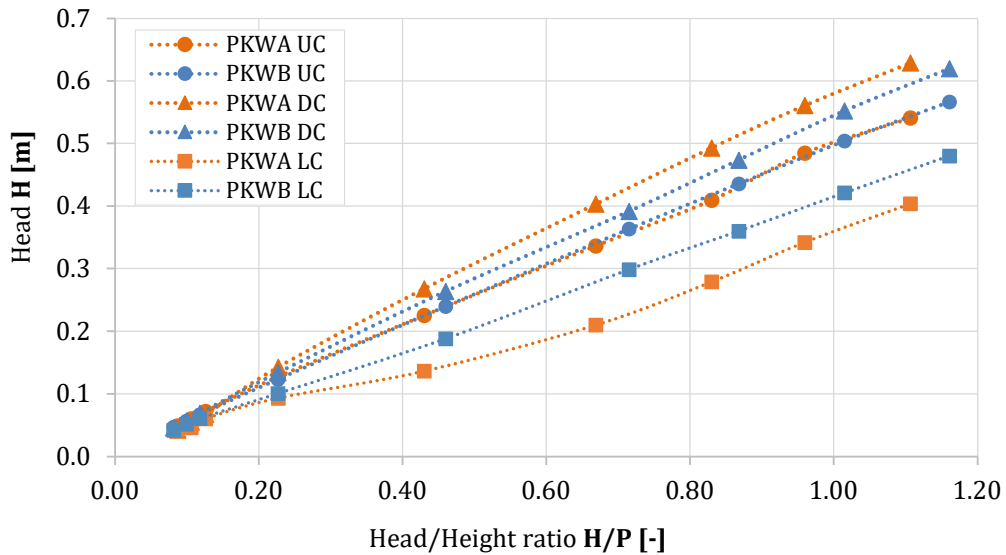
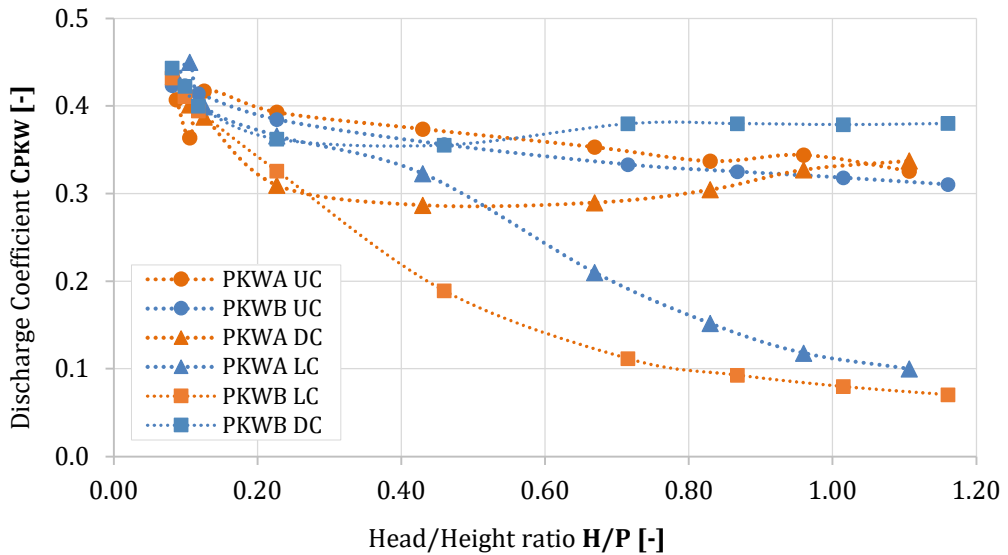


Fig. 6.29 Head over the upstream, downstream and lateral crests of the  $PKW_A$  and  $PKW_B$

The head and discharge influence the discharge coefficient,  $C_{PKW}$ , of the upstream, downstream and lateral crests of the  $PKW_A$  and  $PKW_B$ . The discharge coefficient for each crest and model has been computed. Figure 6.30 presents the rating curves of the upstream, downstream and lateral crests for both  $PKW_A$  and  $PKW_B$ . The upstream crest of  $PKW_A$  is more efficient for  $H/P > 0.15$ , because the upstream head for both models is very similar, but the upstream crest of  $PKW_A$  discharges more water, leading to a higher discharge coefficient. Regarding the downstream crest, the combination of higher head of  $PKW_A$  and higher discharge of  $PKW_B$ , result in a higher  $PKW_B$  discharge coefficient. Furthermore, the lateral crest of  $PKW_A$  is more efficient due to the higher discharge and lower head values. Lastly, it can be observed that the discharge coefficients corresponding to the upstream and downstream crest of both configurations vary narrowly whereas the lateral crest discharge coefficient decreases remarkably and more rapidly for the  $PKW_B$ .



**Fig. 6.30** Discharge Coefficient of the upstream, downstream and lateral crests of the  $PKW_A$  and  $PKW_B$

The difference in terms of head between  $PKW_A$  and  $PKW_B$  is conditioned by the kinetic term and water level, thus, the water velocity and the water surface profile, which ultimately depends on the hydraulic behaviour of the inlet and outlet keys. Therefore, an evaluation of the velocity distribution and water level inside the inlet and outlet keys has been performed. Figures 6.31 and 6.32 display the velocities and the water surface profiles, respectively, for both  $PKW_A$  and  $PKW_B$ . For a certain discharge value, the inlet section of the  $PKW_A$  is more vertically constraint, which causes the acceleration of the flow in the inlet key in comparison with the  $PKW_B$ . Indeed, Figure 6.31 shows increasing velocity values once entering the inlet key section of  $PKW_A$ . This acceleration provokes a reduction of the water level, which for the  $PKW_A$  means the transition between a flat free surface along the inlet key for lower heads ( $H/P \approx 0.12$ ) to a rippled one for higher heads ( $H/P \approx 0.43$ ), ultimately causing a lower water level over the downstream crest. Likewise, the increasing velocities induce to the raise of the kinetic term. On the contrary, the larger inlet section of the  $PKW_B$  provokes a flatter water surface profile (Figure 6.32) and

smaller velocities, therefore, leading to a higher water level in comparison with  $PKW_A$ .

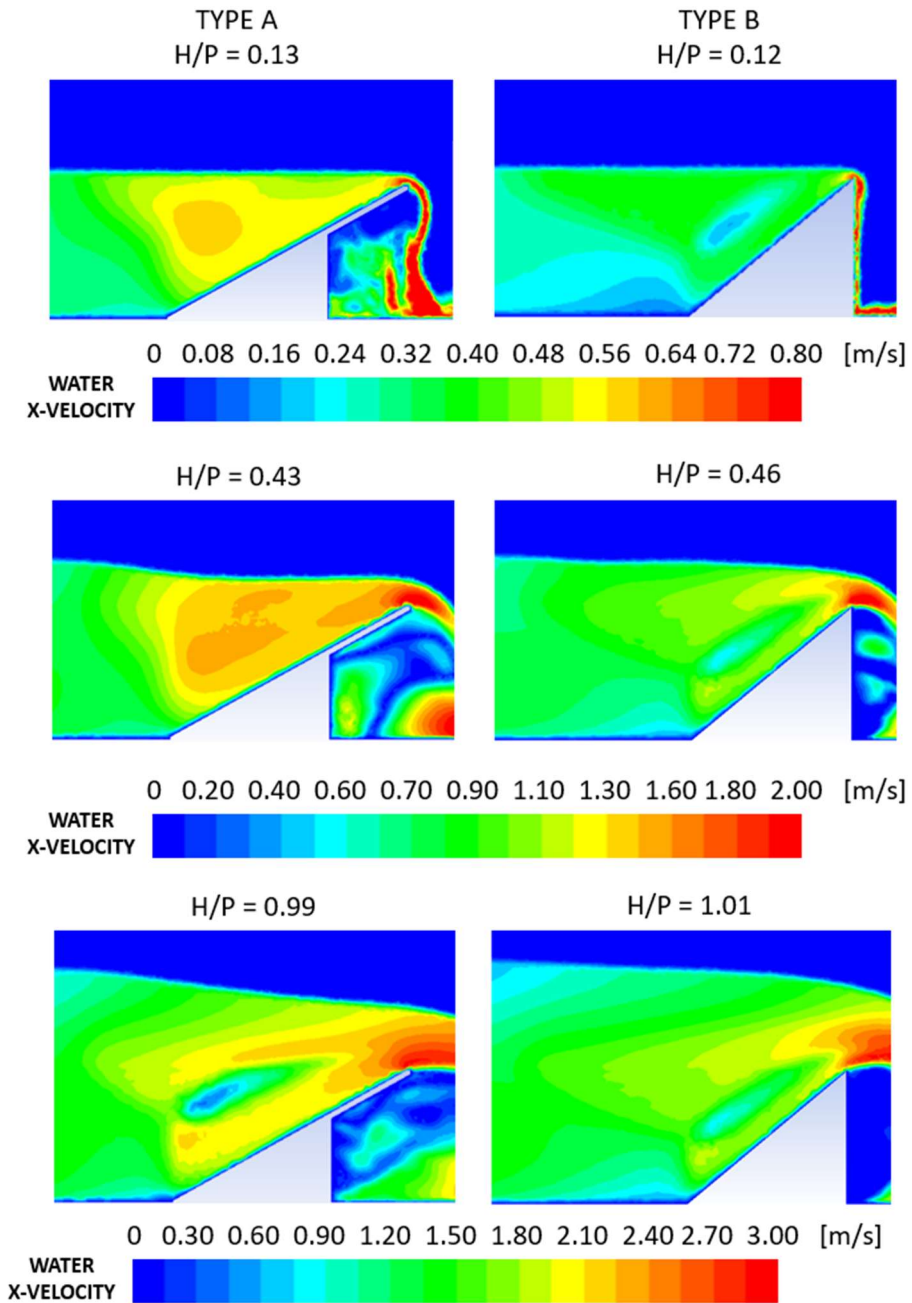
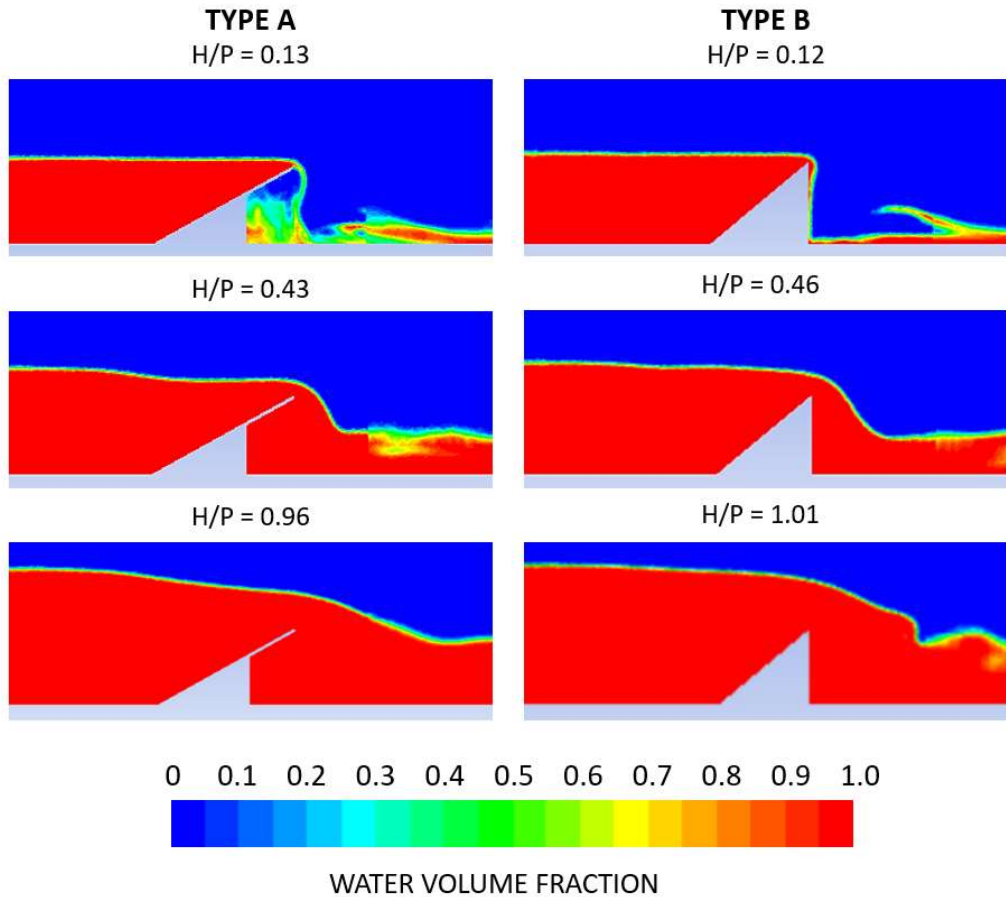


Fig. 6.31 Velocity distribution in the main flow direction on the inlet key for the PKW<sub>A</sub> and PKW<sub>B</sub>



**Fig. 6.32** Water volume fraction on the inlet key for the  $PKW_A$  and  $PKW_B$

Regarding the outlet key, the hydraulic efficiency will depend on the submergence of the upstream and lateral crests, which appears as soon as the free surface elevation in the outlet key becomes higher than the lateral crest one. Figure 6.34 presents the water surface profiles on the downstream section of the outlet key (Figure 6.33) of both  $PKW_A$  and  $PKW_B$ . It can be observed that the filling of the outlet key of  $PKW_B$ , thus the submergence of the upstream and lateral crests, occurs at lower head, as a consequence of both the smaller outlet key slope, which reduces the distance from the outlet key bottom to the lateral crest, and the amount of flow overpassing the lateral crest, which is completely discharged over the outlet key. On the contrary, the  $PKW_A$  is characterized by a higher outlet slope and part of the

lateral crest discharge is directly released to the downstream part of the weir, causing a later filling of the outlet key and submergence of the lateral crests.

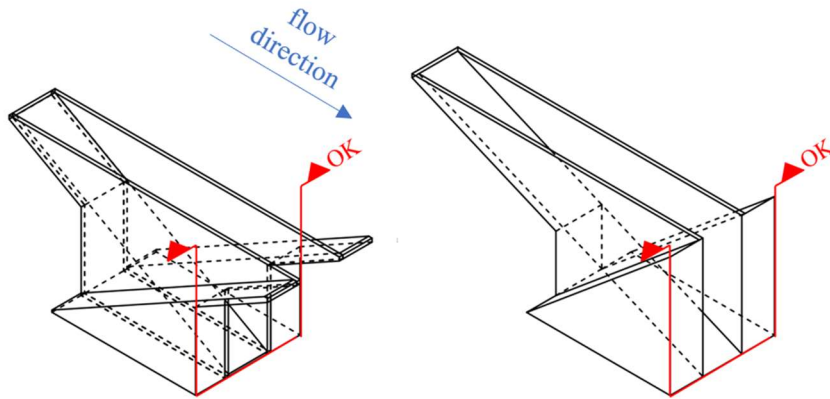


**Fig. 6.33 Outlet key location for PKW<sub>A</sub> and PKW<sub>B</sub>**

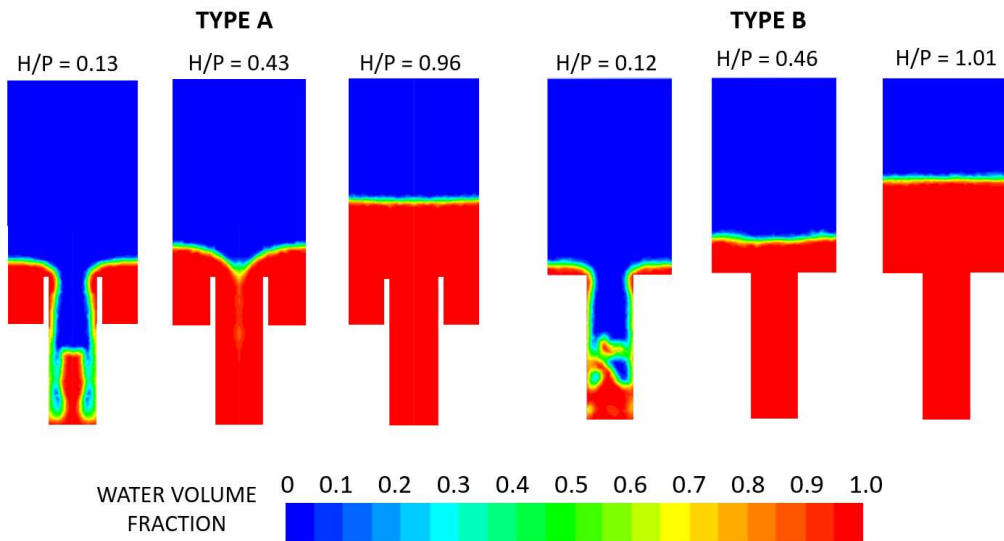


**Fig. 6.34 Water volume fraction on the outlet key for the PKW<sub>A</sub> and PKW<sub>B</sub>**

## References

- Denys, F. J. M., & Basson, G. R. (2020). Unsteady Hydrodynamic Behavior at Piano Key Weirs. *Journal of Hydraulic Engineering*. [https://doi.org/10.1061/\(ASCE\)HY.1943-7900.0001729](https://doi.org/10.1061/(ASCE)HY.1943-7900.0001729)
- Guo, X., Liu, Z., Wang, T., Fu, H., Li, J., Xia, Q., & Guo, Y. (2019). Discharge capacity evaluation and hydraulic design of a piano key weir. *Water Science and Technology: Water Supply*. <https://doi.org/10.2166/ws.2018.134>
- Hu, H., Qian, Z., Yang, W., Hou, D., & Du, L. (2018). Numerical study of characteristics and discharge capacity of piano key weirs. *Flow Measurement and Instrumentation*. <https://doi.org/10.1016/j.flowmeasinst.2018.05.004>
- Kabiri-Samani, A., & Javaheri, A. (2012). Discharge coefficients for free and submerged flow over Piano Key weirs. *Journal of Hydraulic Research*. <https://doi.org/10.1080/00221686.2011.647888>
- Machiels, O. (2012). Experimental study of the hydraulic behaviour of Piano Key Weirs. University of Liège - Faculty of Applied Science.
- Machiels, O., Dewals, B., Archambeau, P., Piroton, M., & Erpicum, S. (2014). An analytical approach for piano key weir hydraulic design. *Labyrinth and Piano Key Weirs II, PKW 2013 - Proceedings of the 2nd International Workshop on Labyrinth and Piano Key Weirs 2013*. <https://doi.org/10.1201/b15985-19>
- Machiels, O., Piroton, M., Pierre, A., Dewals, B., & Erpicum, S. (2014). Experimental parametric study and design of Piano Key Weirs. *Journal of Hydraulic Research*. <https://doi.org/10.1080/00221686.2013.875070>
- Ribeiro, M. L., Pfister, M., Schleiss, A. J., & Boillat, J. L. (2012). Hydraulic design of a-type piano key weirs. *Journal of Hydraulic Research*. <https://doi.org/10.1080/00221686.2012.695041>

---

## Chapter 7

# Implementation of a Fish Pass in a type B Piano Key Weir

---

The location of weirs in rivers allows increasing the water level for numerous purposes, such as hydropower exploitation, however, this barrier contributes to increase the risks related to floods and to endanger the proper fish movements and sediments transport. The possibility of installing a PKW could improve the discharge efficiency, which helps to prevent floods caused by overtopping of the banks. Moreover, the velocity component in the Z-direction upstream PKWs contributes to flushing sediments (Sharma and Tiwari, 2014; Nosedá *et al.*, 2019), making PKWs a great option for rivers. Nevertheless, as presented in Chapter 3, the most common pressures on surface water bodies are associated to hydromorphological barriers, endangering fish movements and related ecosystems. Hence, the European Environment Agency established policies to ensure the restoration of fish habitats, including improving river continuity, managing sediments, and restoring minimum ecological flows.

In this Chapter 7, the combination of a PKW structure with a Fish Pass is developed aiming to overcome the aforementioned issues. The new structure could be implemented in cases where an increase of the river water level is required, operating in two distinct conditions:

- Regular Conditions: functioning as a fish pass, ensuring the safe fish passage through the obstacle created by the structure itself, and contributing to provide the minimum ecological water flow.
- Wet Extreme Condition: functioning as a PKW, providing higher discharge capacity than other types of weir and flushing sediments downstream the river.

## 7.1 Denil Fish Pass Design

In order to select the geometric characteristics of a fish pass it is necessary to define the biological operating range, thus, the target species. As mentioned before, the selected structure is a Denil fish pass, which is suitable for trout, cyprinids and salmonids. Within this species range, the fish pass design for Salmon is the one which consents a higher bottom channel slope,  $I = 0.2$ . As the purpose of combining both structures is to allow the fish passage while increasing the discharge capacity of the PKW, choosing the maximum possible steeper slope means increasing the PKW height, which contributes to improve the discharge efficiency. According to the FAO (Food and Agriculture Organization of the United Nations, 2002), the recommended geometric features for salmonids are (Tab. 3.2):

- Channel width,  $b$ , equal to 0.8m.
- Bottom slope,  $I$ , a maximum of 20%.
- Length of the channel,  $l$ , between 10 and 12 m.
- Water discharge,  $Q$ , equal to  $0.53 \text{ m}^3/\text{s}$  for a  $h^*/b_a = 1.5$  ratio.

As far as the baffles located inside the Denil pass channel are concerned, there are some recommended guide values, gathered in Tab 3.3, for the dimensionless of the baffles cutouts and the distance between the baffles, which are related to the channel width. Considering  $b = 0.8 \text{ m}$ , the channel and baffles dimensions are gathered in Table 7.1.

	Parameter	Size [m]
$h_a$	Height of a baffle	1.300

<b><i>b</i></b>	Width of a baffle	0.800
<b><i>b<sub>a</sub></i></b>	Cutout width	0.464
<b><i>c<sub>1</sub></i></b>	Distance from the bottom to vertex of V-section	0.200
<b><i>c<sub>2</sub></i></b>	Distance from the vertex to the upper part of the V-section	0.400
<b><i>s</i></b>	Distance between baffles	0.528

**Tab. 7.1 Baffles dimensions of the fish pass**

The designed baffle is presented in Figure 7.1.

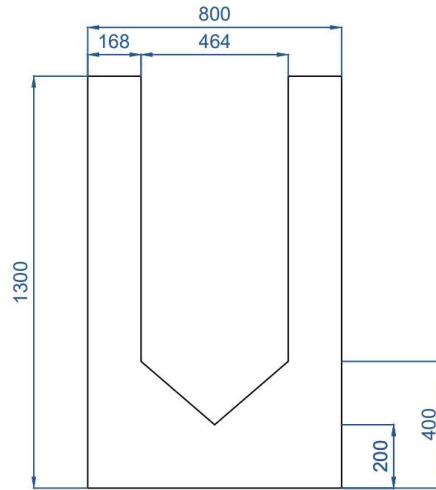


**Fig. 7.1 Implemented Boundary Conditions and Interfaces**

## 7.2 Fish Pass – PKW structure

Considering the designed  $PKW_A$  and  $PKW_B$ , with same dimensionless ratios in terms of height, developed length and inlet and outlet key widths, the  $PKW_B$  is characterized by a smaller outlet key slope ( $S_{oB} = 0.416$ ) in comparison with  $PKW_A$  ( $S_{oA} = 0.555$ ), which turns the  $PKW_B$  more suitable to be combined with a fish pass. Aiming to assess the hydraulic behaviour in terms of discharge capacity of the PKW and suitability for fish to overtake the obstacle itself, the designed Denil fish pass has been scaled and implemented into the tested  $PKW_B$ . The scale process has been computed by adapting the fish pass channel width ( $b=0.80$  m) to the outlet key width of the  $PKW_B$  ( $W_o=0.17$  m), resulting in a scale factor,  $\lambda$ , equal to 0.2125. Nonetheless, the outlet key slope of the designed  $PKW_B$  is 0.42, higher than the recommended value of 0.2 from the FAO (Food and Agriculture Organization of the

United Nations, 2002). Likewise, the lateral walls of the PKW should work as the lateral walls of the channel, thus, a variation of the outlet key geometry has been performed by reducing the height of the upstream crest of the outlet key, resulting in two heights: the PKW crest height,  $P_{crest}$ , and the upstream height of the fish pass,  $P_{UPFP}$ . With the purpose of reducing the slope to achieve the advised value, the outlet key has been extended downstream. Similarly, the upstream crest height (Figure 3.8) was estimated based on the recommended upstream water level,  $h_0$ , which is related to upstream water depth from the V-notch in a Denil pass,  $h^*$ , by the function presented in Figure 7.2.

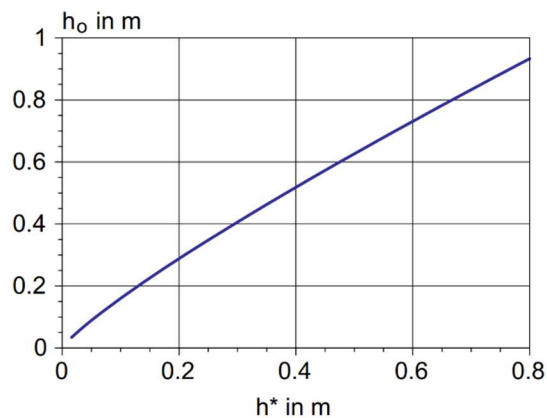


**Fig. 7.2 Relation of  $h^* = f(h_0)$**  (Food and Agriculture Organization of the United Nations, 2002)

Considering the cutout width,  $b_a = 0.464$  m and following the recommended ratio  $h^*/b_a = 1.5$ , the value of  $h^* \approx 0.7$  m, thus, the upstream water level in the fish pass results  $h_0 \approx 0.84$  m. Applying the scaling factor,  $h_0_{model} = 0.179$ , establishing an upstream crest height equal to 0.340 m. The developed combined structure,  $PKW_{B-FP}$ , is shown in Figure 7.3.

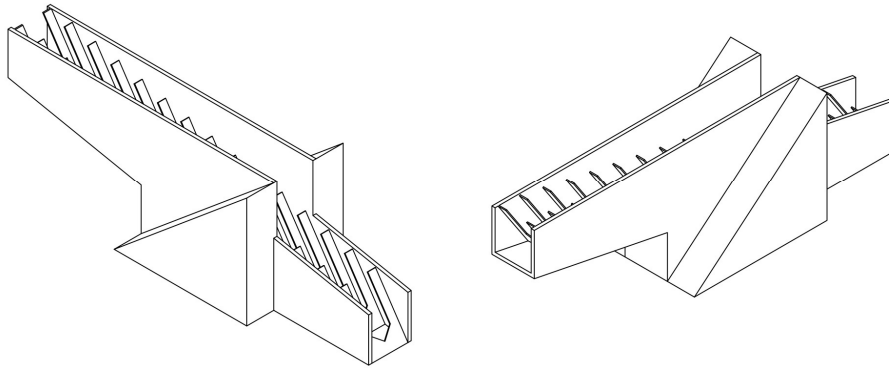


Fig. 7.3 Isometric views of the combined PKW and fish pass structure,  $PKW_{B-FP}$ .

Hence, the fish pass scaled, and the modified  $PKW_{B-FP}$  dimensions are collected in Table 7.2 and Figure 7.4:

Parameter	Size [m]	Parameter	Size [m]
$h_a$	0.276	$B$	1.254
$b$	0.170	$B_o$	0.628
$b_a$	0.099	$B_i$	0
$c_1$	0.043	$B_b$	0.626
$c_2$	0.085	$W_i$	0.255
$s$	0.112	$W_o$	0.170
$l$	1.736	$W_u$	0.455
$P_{PKW\ crest}$	0.522	$L_u$	2.963
$P_{UPFP}$	0.340	$T_s$	0.150

Tab. 7.2 Dimensions of the combined structure  $PKW_{B-FP}$ .

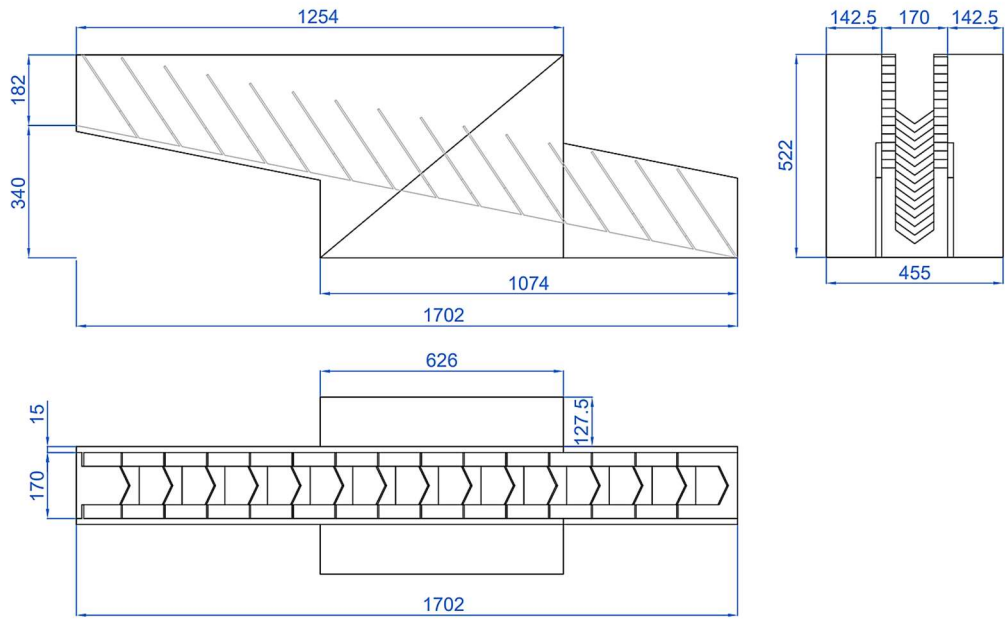


Fig. 7.4 Cross, lateral and plain view of the  $PKW_{B-FP}$ .

Likewise, the combined PKW – Fish Pass structure dimensions in real scale are collected in Table 7.3 and shown in Figure 7.5.

Parameter	[m]	Parameter	[m]
$h_a$	1.300	$B$	5.901
$b$	0.800	$B_o$	2.955
$b_a$	0.464	$B_i$	0
$c_1$	0.200	$B_b$	2.946
$c_2$	0.400	$W_i$	1.200
$s$	0.528	$W_o$	0.800
$l$	8.169	$W_u$	2.141
$P_{PKW\ crest}$	2.456	$L_u$	13.944
$P_{UP\ FP}$	1.602	$T_s$	0.71

Tab. 7.3 Dimensions of the combined structure  $PKW_{B-FP}$ .

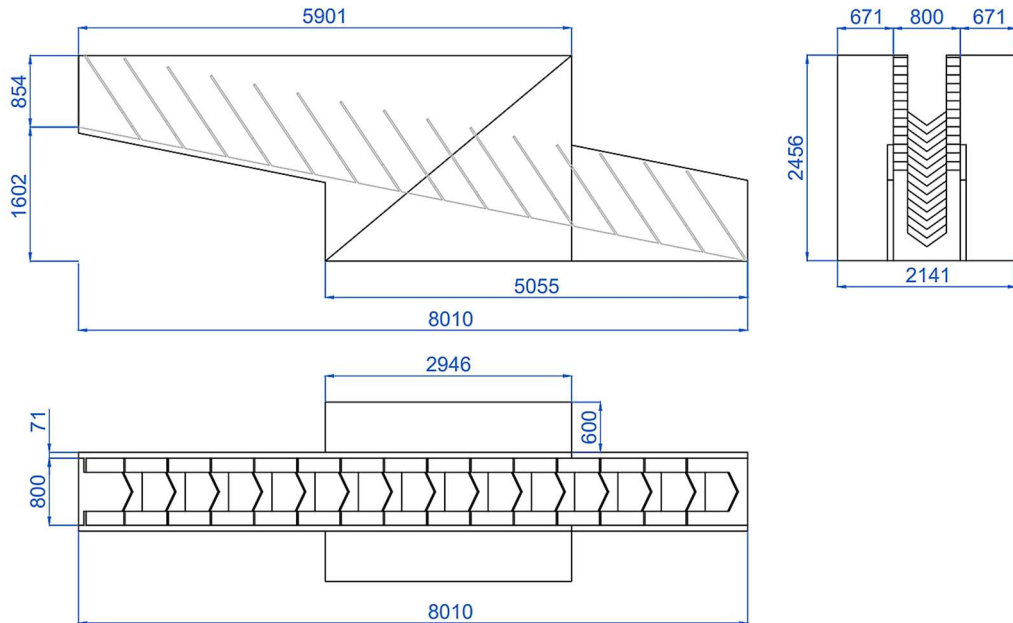


Fig. 7.5 Cross, lateral and plain view of the  $PKW_{B-FP}$  at real scale.

### 7.3 Velocity assessment of $PKW_{B-FP}$ working as a fish pass

The design procedure for the Denil fish pass following the recommended guidelines from the FAO (Food and Agriculture Organization of the United Nations, 2002) presented before should ensure the correct functioning of the  $PKW_{B-FP}$  as a fish pass. This design would work within the recommended range for a water level upstream equal to the crest height of the PKW height,  $P_{PKW_{crest}}$ , allowing a discharge through the fish pass equal to  $Q = 0.53 \text{ m}^3\text{s}^{-1}$  (Table 3.1).

Aiming at verifying the velocity field inside the outlet key, where the fish pass is located, a CFD model analysis has been carried out. The scaled  $PKW_{B-FP}$  has been implemented in Ansys Fluent (*ANSYS Fluent 12.0 User's Guide*, 2019) following the same criteria as the previous studied. The design flowrate,  $Q = 0.53 \text{ m}^3\text{s}^{-1}$ , has been also scaled considering  $\lambda = 0.2125$ , resulting in  $Q = 0.01103 \text{ m}^3\text{s}^{-1}$ .

The velocity field obtained in the middle of the fish pass has been scaled to reality and it is presented in Figure 7.6. Results showed that the maximum advisable velocity of  $2 \text{ m s}^{-1}$  is exceeded throughout the majority of the fish pass.

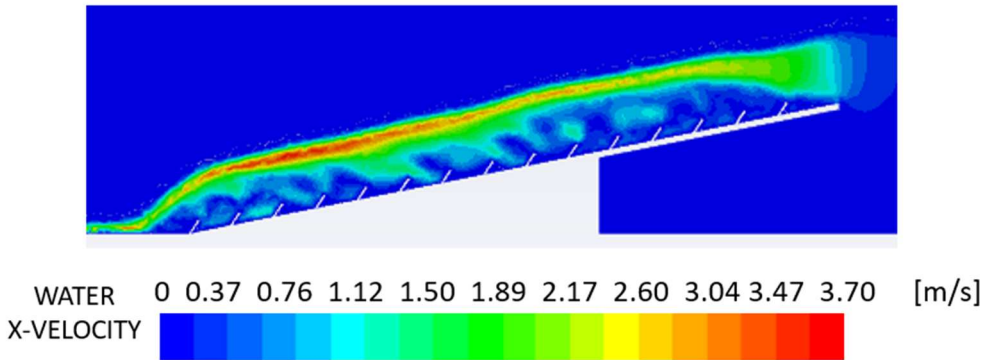


**Fig. 7.6** Water velocity distribution in real scale in the middle of the fish pass of the  $PKW_{B-FP}$ .

Furthermore, an analysis has been made of the velocity field at some of the baffles inside the fish pass. Specifically, the baffles considered (Figure 7.7) are the most upstream (B15) and most downstream baffles (B1), and two located intermediate (B5 and B10). Results of the velocity fields are gathered in Figure 7.8, and it can be observed that the upper part of the baffles are characterized by velocities over  $2 \text{ m s}^{-1}$ , in exception of B15, where most of the velocity values are smaller than  $2 \text{ m s}^{-1}$ .

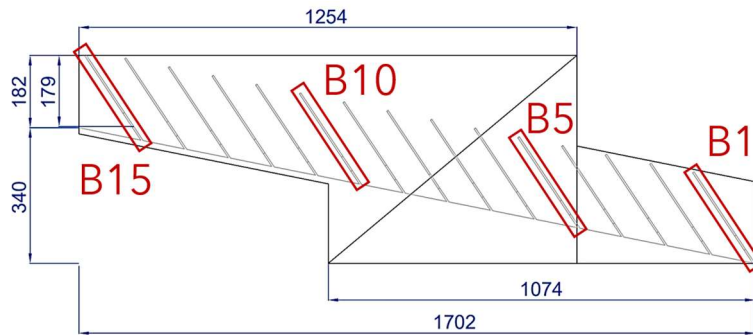


**Fig. 7.7** Baffle location at the  $PKW_{B-FP}$

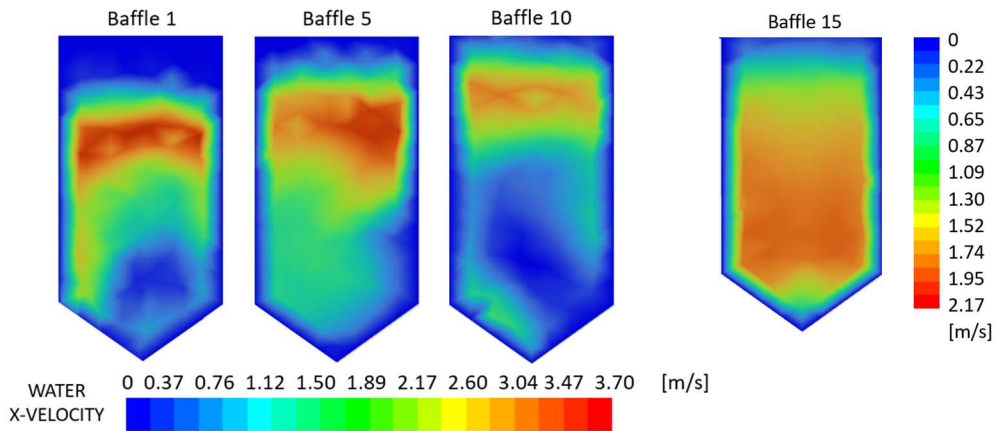


Fig. 7.8 Velocity distribution at the baffles 1, 5, 10 and 15 of the  $PKW_{B-FP}$

These results show that the only suitable area for fishes to surpass the fish pass is the bottom part of the baffles, however, this may be insufficient, leading to the necessity to properly assess the velocity field of diverse baffles geometries.

#### 7.4 Discharge efficiency assessment of $PKW_{B-FP}$ working as a weir

The discharge coefficient,  $C_{PKW}$ , for the combined structure has been calculated as presented in Chapter 6, with the water level,  $h$ , and mean velocity,  $\bar{v}$ , obtained at a section located 50 cm upstream the  $PKW_{B-FP}$  upstream crest, obtaining the upstream head,  $H$ , applying Equation 4.9.

The non-dimensional rating curves of the discharge coefficient  $C_{PKW}(H/P)$  of the  $PKW_B$  and  $PKW_{B-FP}$  are given in Figure 7.9.

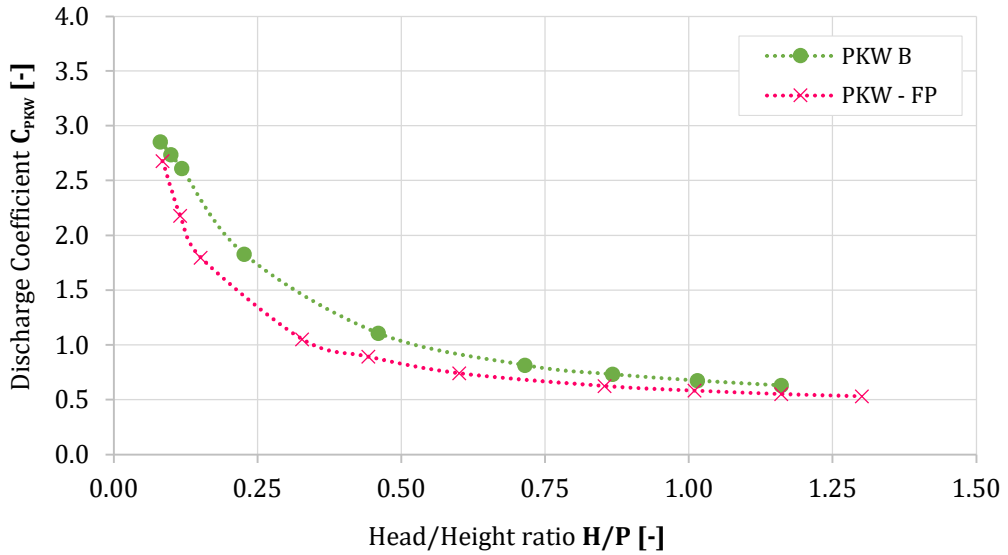


Fig. 7.9 Numerical rating curves  $C_{PKW}$  (H/P) for  $PKW_B$  and  $PKW_{B-FP}$

Table 7.4 presents the obtained results for the upstream water level, velocity and head, and the discharge coefficient for each flowrate tested. The difference of these hydraulic parameters is expressed using Equation 7.1:

$$\Delta = \frac{x_{PKW_B} - x_{PKW_{B-FP}}}{x_{PKW_B}} \quad (7.1)$$

where  $x_{PKW_B}$  correspond to the obtained value for the  $PKW_B$  and  $x_{PKW_{B-FP}}$  represents the corresponding value for the  $PKW_{B-FP}$ . Results showed that the discharge coefficient of the tested  $PKW_{B-FP}$  geometry is up to ~42.4% smaller, which results in an increase of the upstream water level up to ~51.8 %.

Flowrate [L s <sup>-1</sup> ]	h [cm]		$\Delta$ [%]	$\bar{v}$ [m s <sup>-1</sup> ]		$\Delta$ [%]
	$PKW_B$	$PKW_{B-FP}$		$PKW_B$	$PKW_{B-FP}$	
50.03	4.03	4.22	-4.6	0.196	0.194	0.9%
64.85	4.85	5.70	-17.6	0.250	0.248	0.8%
80.25	5.68	7.43	-31.0	0.305	0.297	2.4%
150	10.41	15.80	-51.8	0.527	0.503	4.7%
262.5	20.70	27.87	-34.6	0.804	0.827	-2.9%
375	32.07	39.97	-24.7	1.016	0.947	6.8%
450	38.45	46.51	-21.0	1.157	1.102	4.8%
525	44.29	52.24	-17.9	1.305	1.281	1.9%

Flowrate [L s <sup>-1</sup> ]	H [cm]		$\Delta$ [%]	$C_{PKW}$ [-]		$\Delta$ [%]
	$PKW_B$	$PKW_{B-FP}$		$PKW_B$	$PKW_{B-FP}$	
50.03	4.23	4.41	-4.3	2.86	2.68	-6.2
64.85	5.17	6.02	-16.4	2.74	2.18	-20.4
80.25	6.15	7.89	-28.2	2.61	1.80	-31.1
150	11.83	17.09	-44.5	1.83	1.05	-42.4
262.5	23.99	31.36	-30.7	1.11	0.74	-33.1
375	37.32	44.55	-19.3	0.82	0.63	-23.3
450	45.28	52.71	-16.4	0.73	0.58	-20.4
525	52.97	60.60	-14.4	0.68	0.55	-18.3

Tab. 7.4 Water level, upstream velocity, head and discharge coefficient comparison between the  $PKW_B$  and the  $PKW_{B-FP}$ .

### 7.4.1 Upstream, downstream and lateral crests analysis

The discharge for  $PKW_B$  and  $PKW_{B-FP}$  over each single crest was computed. The height of the upstream crest considered is indicated in Figure 7.10. Results presented in Figure 6.11 show that the upstream crest of the  $PKW_{B-FP}$  discharges more water because it is located at lower height, which increments the flow area for a certain water level. Regarding the downstream crest, the  $PKW_B$  discharges slightly more water, while the lateral crests of the  $PKW_B$  are highly more efficient.

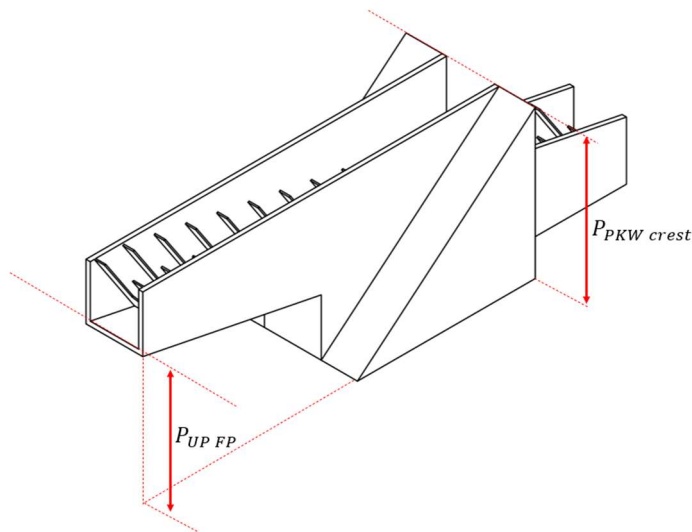
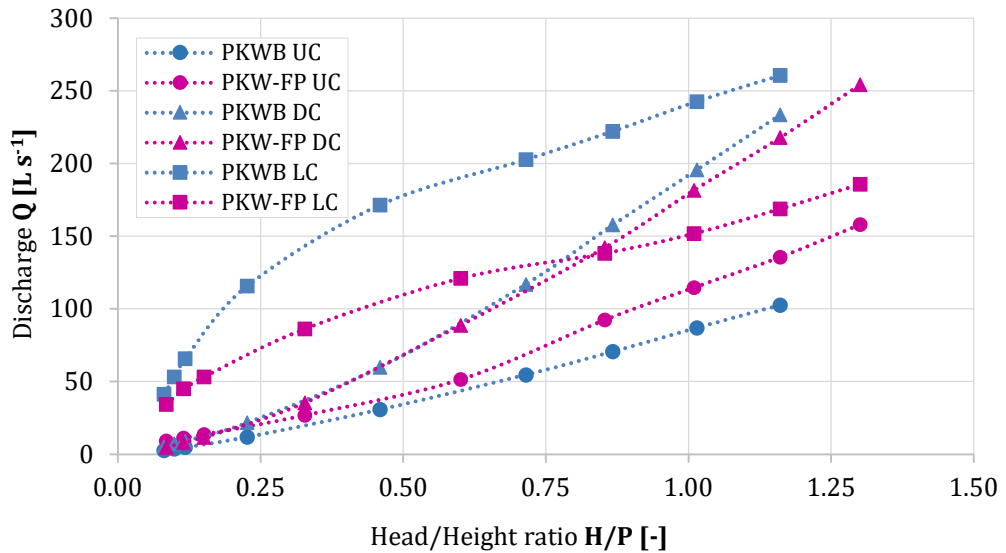
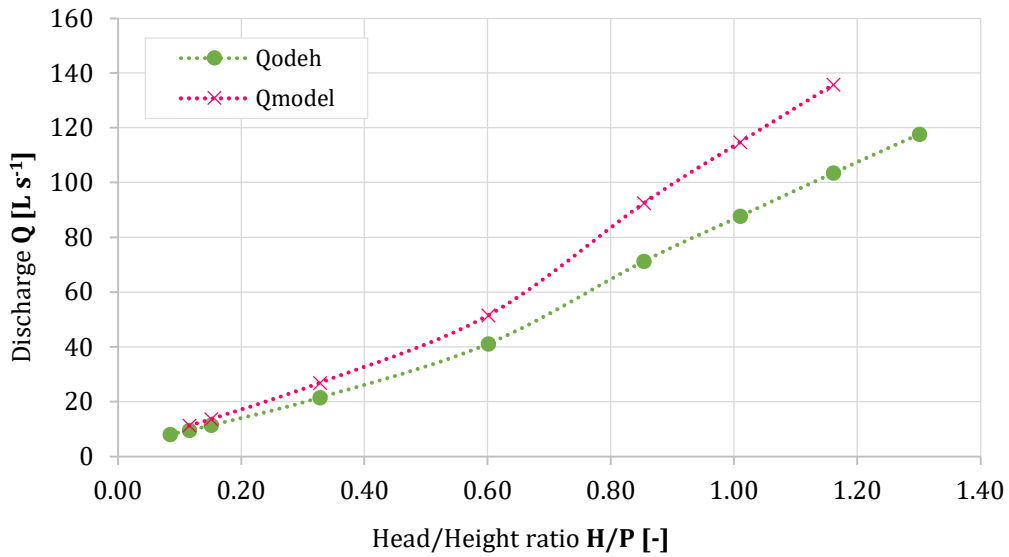


Fig. 7.10 Scheme of the total height and height of the upstream crest of the  $PKW_{B-FP}$



**Fig. 7.11 Discharge over the upstream (UC), downstream (DC) and lateral crests (LC) of the PKW<sub>B</sub> and PKW<sub>B-FP</sub>**

Likewise, the flowrates passing the upstream crest section obtained from the performed simulations were compared with those obtained applying Odeh's (Odeh, 2003) equation (Equation 3.3) and results are presented in Figure 7.12. The average value of the calculated scatters is ~26.76%, with minimum and maximum values of 15.31% and 34.24%, respectively.



**Fig. 7.12** Discharge comparison between the results obtained from Odeh's equation (Odeh, 2003) and from the CFD model for the upstream crest.

Furthermore, Figure 7.13 represents the head distribution for the upstream crest of both configurations. It can be observed that the water level over the upstream crest of the  $PKW_{B-FP}$  is higher ( $h_{PKW-FP UC}$ ), which is expected as it is located at a lower height ( $P=P_{UC FP}$ ). Nevertheless, considering the PKW crest, at a height equal to  $P_{PKW crest} = 0.522$  m, it can be observed that the water level for the  $PKW_{B-FP}$  is still greater ( $h_{PKW-FP}$ ), with a steeper tendency in comparison with  $PKW_B$ . In regard to the kinetic term, the  $PKW_B$  provided bigger values, meaning higher velocities.

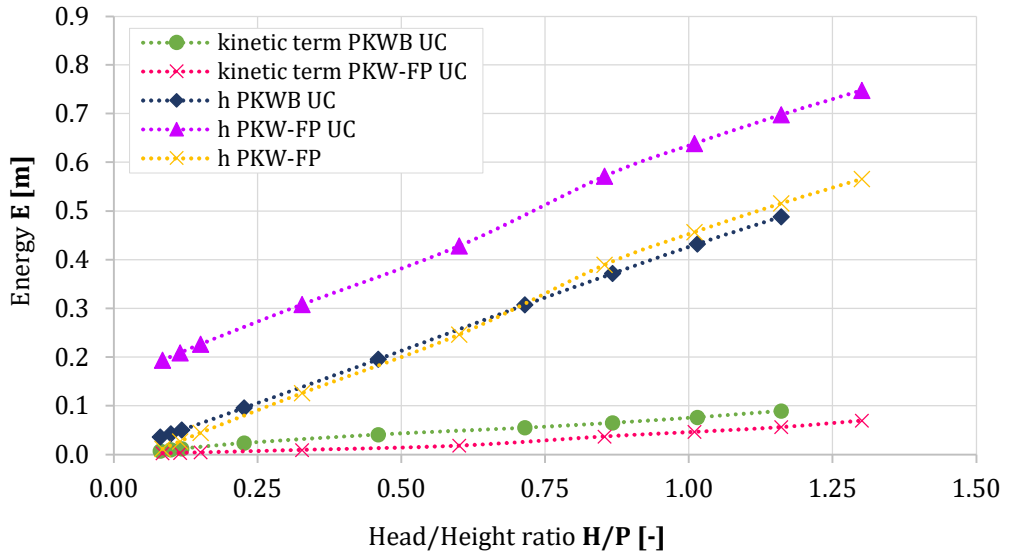


**Fig. 7.13 Energy vs Discharge curves of the PKW<sub>B</sub> and PKW<sub>B-FP</sub> from the upstream crest**

The rating curves of the water head for each crest are presented in Figure 7.14. As shown in the Figure, the head values over the crests of the PKW<sub>B-FP</sub> are greater, however, the upstream crest presents a higher discrepancy due to the difference in the water level.

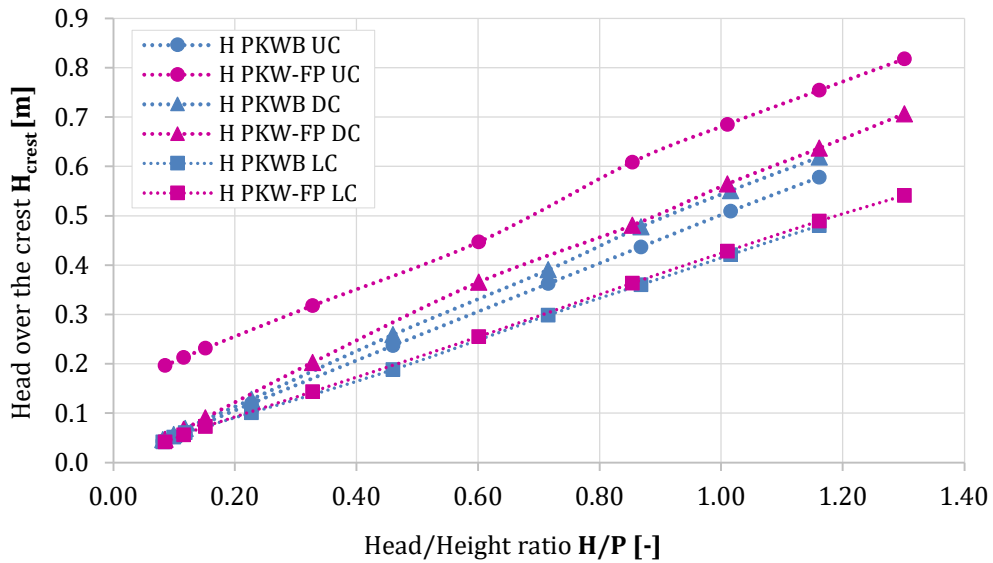


**Fig. 7.14** Head over the upstream, downstream and lateral crests of the  $PKW_B$  and  $PKW_{B-FP}$

The combination of a much higher head of the upstream crest and the lower discharge, for the tested  $H/P$  range, makes the upstream crest of the  $PKW_{B-FP}$  much less efficient. In terms of the downstream crest discharge and head values for both configurations are very similar, turning the difference in efficiency negligible. Lastly, the lateral crests of  $PKW_B$  are able to discharge much more water at similar head values, leading to a higher discharge efficiency for the  $PKW_B$ . Indeed, Figure 7.15 presents the discharge coefficient for each crest of both  $PKW_B$  and  $PKW_{B-FP}$ . Results showed the higher discharge coefficient for the upstream and lateral crests on the  $PKW_B$  at the expense of the similar discharge coefficients of the downstream crest.

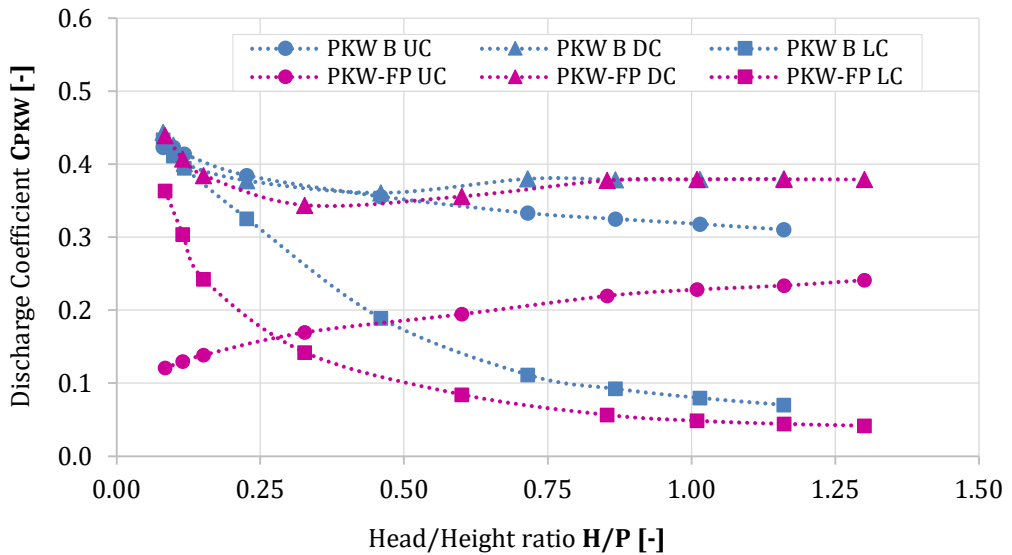


**Fig. 7.15 Discharge Coefficient of the upstream, downstream and lateral crests of the  $PKW_B$  and  $PKW_{B-FP}$**

Furthermore, an analysis of the lateral crests has been performed by analysing the submergence of the lateral crests. Figure 7.16 presents the water profiles on the outlet key for the  $PKW_B$  and the  $PKW_{B-FP}$ . It can be observed that the submergence of the lateral crest of  $PKW_{B-FP}$  occurs at lower head, probably because of the smaller outlet key slope, which reduces the distance from the outlet key bottom to the lateral crest, and the baffles installed across the outlet key, which difficult the flow passage.

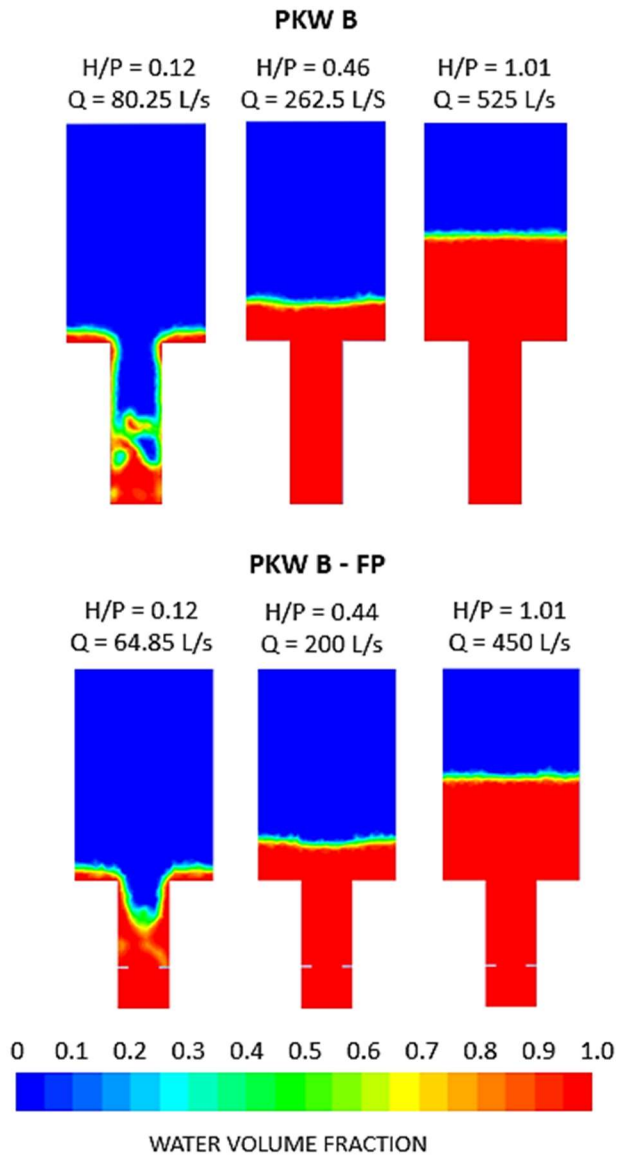


Fig. 7.16 Water volume fraction on the outlet key for the PKW<sub>B</sub> and PKW<sub>B-FP</sub>

## References

- ANSYS Fluent 12.0 User's Guide (2019)
- Food and Agriculture Organization of the United Nations, D.V. für W. und K. e. V. (DVWK) (2002) Fish passes - Design, dimensions and monitoring.
- Nosedá, M. et al. (2019) "Upstream Erosion and Sediment Passage at Piano Key Weirs," *Journal of Hydraulic Engineering*, 145(8).
- Odeh, M. (2003) "Discharge Rating Equation and Hydraulic Characteristics of Standard Denil Fishways," *Journal of Hydraulic Engineering*, 129(5), pp. 341–348. doi:10.1061/(asce)0733-9429(2003)129:5(341).
- Sharma, N. and Tiwari, H. (2014) "Experimental study on vertical velocity and submergence depth near Piano Key weir," in *Labyrinth and Piano Key Weirs II - PKW 2013*, pp. 93–100.



---

## Chapter 8

### Synthesis and Conclusions

---

#### 8.1 On the Discharge Efficiency of type A and type B PKWs

##### 8.1.1 Conclusions

An assessment was performed to evaluate the discharge efficiency of three PKW geometries: a symmetric type A,  $PKW_A$ , with  $Wi/Wo=1.5$ , the same model rotated  $180^\circ$ , resulting in a type A  $Wi/Wo=0.67$ ,  $PKW_{A\_reverse}$ , and a type B model,  $PKW_B$ , with the main geometric features than  $PKW_A$  ( $L, P, Wi, Wo, Bb, Bh$ ). The  $PKW_A$  and the  $PKW_{A\_reverse}$  were experimentally and numerically tested while the  $PKW_B$  was only studied numerically. The comparison between numerical and experimental results proved the effectiveness of using numerical testing. Specifically, a mesh size of  $\sim 9.6\%$  P can predict the discharge coefficient and velocity distribution with reasonable accuracy in PKWs, providing GCIs equal to 0.53% and 2.46%, respectively. Therefore, coupling both approaches allowed assessing the velocity distribution and discharge coefficient for a wider range of upstream head.

Additionally, the analytical equations for the estimation of the discharge coefficient were compared with the numerical data obtained for the  $PKW_A$ ,  $PKW_{A\_reverse}$  and  $PKW_B$  for all the tested H/P values. Results showed that the analytical equations from Machiels et al. (Machiels *et al.*, 2014), Hu et al. (Hu *et al.*, 2018) and Guo et al. (Guo *et al.*, 2019) for the estimation of the discharge coefficient were able to predict with reasonable scatters the discharge coefficient for the tested geometries, although the limits of applicability. Indeed, the minimum and maximum

relative errors for the  $PKW_A$  were 0.78% and 17.08% for Machiels et al. (Machiels et al., 2014), 1.82% and 24.20% for Hu et al. (Hu et al., 2018) and 1.46% and 24.2% for Guo et al. (Guo et al., 2019), whereas for the  $PKW_{A\_rev}$  were 5.34% and 32.97% for Machiels et al. (Machiels et al., 2014), 9.08% and 43.51% for Hu et al. (Hu et al., 2018) and 1.81% and 38.09% for Guo et al. (Guo et al., 2019). Lastly, for the  $PKW_B$  were 6.85% and 19.24% for Machiels et al. (Machiels et al., 2014), 0.51% and 25.95% for Hu et al. (Hu et al., 2018) and 4.55% and 24.86% for Guo et al. (Guo et al., 2019). This comparison further demonstrated the reliability of the numerical model for estimating the discharge coefficient.

Furthermore, Machiels et al. (Machiels et al., 2014) and Hu et al. (Hu et al., 2018) equations follow the same structure, which allows to calculate the total specific discharge,  $q$ , and it is employed to determine the discharge coefficient of PKWs, thus, an analysis of these equations has been carried out for the values obtained for the  $PKW_A$  and  $PKW_B$ . In terms of the total specific discharge, both equations present the same trend, and for the  $PKW_A$ , numerical results are closer to those from Machiels et al. (Machiels et al., 2014) equation, whereas, for the  $PKW_B$ , the results are similar to those from Machiels (Machiels et al., 2014) for  $H/P \lesssim 0.8$ , but closer to those obtained with Hu et al. (Hu et al., 2018) equation for  $H/P \gtrsim 0.8$ . In terms of the upstream crest,  $PKW_A$  results are better correlated to those from Machiels (Machiels et al., 2014), while results for the  $PKW_B$  to those from Hu et al. (Hu et al., 2018). Regarding the downstream crests, both configurations' results are closer to those obtained with Hu et al. (Hu et al., 2018) equation. The foremost difference in tendency is showed for the lateral crests: the specific discharge increases, however, for  $H/P \gtrsim 0.7$  for the  $PKW_A$  and  $H/P \gtrsim 0.45$  for the  $PKW_B$ , the values from the CFD model keep growing, the values obtained from Hu et al. (Hu et al., 2018) equation remained primarily constant and those from Machiels et al. (Machiels et al., 2014) starts decreasing.

In regard to the discharge coefficient, the obtained results showed that the  $PKW_A$  discharge coefficient is up to ~34% higher than the  $PKW_{A\_reverse}$ , resulting in an increase of the upstream head for the  $PKW_{A\_reverse}$ , up to ~32% for  $H = 0.665$ ,

remarking the relevance of the  $W_i/W_o$  ratio in the discharge efficiency of PKWs. Conversely, the tested  $PKW_B$  resulted more efficient for lower head ( $H/P \lesssim 0.35$ ) than the  $PKW_A$ , however, when increasing the upstream head, the  $PKW_A$  model proved to be more efficient. This change in efficiency can be explained because of the hydraulic behaviour of both geometries. The lateral crests of the  $PKW_B$  are submerged faster by the outlet key flow, provoke the filling of outlet key of  $PKW_B$  at lower  $H/P$  values ( $H/P \simeq 0.35$ ) than those of the  $PKW_A$  ( $H/P \simeq 0.50$ ).

Moreover, the inlet key of  $PKW_A$  is less efficient due to the acceleration of the flow caused by the constraint inlet section area, that reduces the water level but increases the velocities, thus, giving higher kinetic term and thus total head. In addition, the flow discharged over the downstream crest of  $PKW_A$  was smaller, leading to a smaller discharge coefficient of the outlet key. Consequently, the discharge coefficient of the tested  $PKW_B$  was higher for  $H/P \lesssim 0.35$ , whereas once the outlet key was filled at higher head, the tested  $PKW_A$  proves to be more efficient. These results also explain the conclusion of former studies carried out by Machiels et al. (Machiels, 2012) who specified that for higher head values, type B efficiency is reduced, meaning that type A results the most efficient.

### 8.1.2 Research Novelty and Contributions

Concerning the developed study, with respect to the research available in the literature, the experimental and numerical analysis was focused on complementing the investigated fields, in terms of the studied geometries and the combination of experimental and numerical approaches (Table 8.1).

Author	L/W	Wi/Wo	Bi/Bo	P/W	B/P	Model
Noui and Ouamane (2011)	4.00 – 8.00	0.67 – 1.54	0 – 1	0.90 – 1.21	0.24 – 0.61	EXP
Leite Ribeiro et al. (2011)	3.00 – 7.00	0.80 – 2.00	1	0.59 – 2.21	1.52 – 4.60	EXP
Laugier et al. (2011)	6.00	1.00	1	0.83	3.00	NUM

Anderson and Tullis (2011)	5.27	0.67 – 1.50	1	0.21	2.48	EXP
Kabiri-Samani and Javaheri (2012)	2.50 – 8.50	0.33 – 1.67	0 – 0.26	0.38 – 0.75	1.00 – 3.30	EXP
Lefebvre et al. (2013)	5.98	0.60 – 4.80	1	0.42 – 1.67	1.50 – 6.00	NUM
Pralong et al. (2014)	5.98	1.00	1	1.66	3.00	NUM
Machiels et al. (2014)	5.00	0.46 – 2.18	0 – inf	0.13 – 0.80	1.00 – 6.00	EXP
Bremer and Oertel (2017)	5.87	1.29	1	0.83	2.40	NUM
Present Study	6.51	0.67- 1	0-1	1.15	2.40	EXP/ NUM

**Tab. 8.1 Range of dimensionless parameters ratios tested on literature.**

Specifically, this research contributed to the assessment of a type B PKW, including the comparison with the corresponding type A model. The analysis performed contributed to explain the observed variation of the discharge coefficient, as a function of the velocity distribution, water depth and discharge over the upstream, downstream and lateral crests. This specific investigation on type B was significantly new because very few considerations were performed in the literature on the type B PKW in terms on the studied hydraulic parameters. The hydraulic behaviour of the inlet and outlet keys is determined by the inlet and outlet cross section, thus the PKW height, slopes and up- and downstream overhangs length, and by the upstream head. Therefore, the accomplished research proved that the discharge coefficient is strongly dependant on the specific geometry, hence, it is not possible to generalize about the efficiency of the different PKW types.

---

## 8.2 On the Implementation of a Denil Fish Pass in a type B PKW

### 8.2.1 Conclusions

After analysing several fish passes, the Denil fish pass was selected to be implemented in the outlet key of the tested  $PKW_B$ . The procedure selected to design of the Denil pass was based on the FAO (Food and Agriculture Organization of the United Nations, 2002) recommendations presented in Chapter 3. Once geometric features were calculated, the fish pass was scaled based on a scale factor that relates the outlet key width with the fish pass channel width. Furthermore, the outlet key of the  $PKW_B$  was modified to foster the Denil pass by lowering the upstream crest and elongating the outlet key to reduce the slope.

This design procedure following the recommended guidelines should ensure the correct functioning of the  $PKW_{B-FP}$  as a fish pass, with a discharge passing through the fish pass equal to  $Q = 0.53 \text{ m}^3\text{s}^{-1}$ , corresponding to an upstream water level equal to the crest height of the PKW height,  $P_{PKW \text{ crest}}$ .

Once the combined structure,  $PKW_{B-FP}$ , was developed, a numerical assessment was performed aiming to evaluate the discharge efficiency of the  $PKW_{B-FP}$  in comparison with the  $PKW_B$ , and to verify the correct functioning of the structure as a fish pass under the recommended range of hydraulic parameters.

The design flowrate,  $Q = 0.53 \text{ m}^3 \text{ s}^{-1}$  was scaled, resulting in  $Q = 0.01103 \text{ m}^3 \text{ s}^{-1}$ . Results showed that the velocity field obtained in the middle of the fish pass exceeded the maximum advisable velocity of  $2 \text{ m s}^{-1}$  throughout the majority of the fish pass. Furthermore, an analysis of the velocity of 4 baffles was carried out: one located upstream, one downstream and two intermediate. It was observed that the upper part of baffles is characterized by velocities over  $2 \text{ m s}^{-1}$ , in exception of the most upstream baffle, where most of the velocity values are smaller than  $2 \text{ m s}^{-1}$ . These results show that the only suitable area for fishes to surpass the fish pass is the bottom part of the baffles, however, this may be insufficient, requiring a further assessment the velocity field of diverse baffle geometries.

Concerning the discharge efficiency, the results showed that the  $PKW_{B-FP}$  discharge coefficient is up to  $\sim 42.4\%$  smaller than the  $PKW_B$ , resulting in an increase of the upstream head up to  $\sim 51.8\%$ . This difference in efficiency was more pronounced between  $H/P \simeq 0.2$  and  $H/P \simeq 0.5$ , however, when increasing the upstream head, this difference was reduced. This reduction in efficiency can be explained because of the superior performance of the outlet key of the  $PKW_B$ . Results from the  $PKW_B$  showed smaller upstream crest head with higher discharge values, leading to a higher discharge coefficient. The numerical results for the discharge through the upstream crest area were also compared with those obtained applying Odeh's equation, predicting the discharge with an average value of the calculated scatters of  $\sim 26.76\%$ , with minimum and maximum values of  $15.31\%$  and  $34.24\%$ , respectively. Regarding the downstream crest, results showed that the difference in discharge efficiency between both configurations is negligible.

Moreover, the reduced slope of the outlet key of the  $PKW_{B-FP}$  in compliance with the installed baffles increase the difficulty of the flow passing through the outlet key, ultimately leading to the filling of outlet key of  $PKW_{B-FP}$  at lower  $H/P$  ratios. This phenomenon triggers the submergence of the lateral crests, which appear at lower  $H/P$  ratios at the  $PKW_{B-FP}$ , meaning reduced discharge over the lateral crests, reducing the discharge coefficient.

These results proved the possibility of effectively combine a fish pass with a PKW, resulting in a new structure that works as a fish pass at regular conditions and as a PKW at flood conditions. The main advantage of this structure may be the rehabilitation of existing linear weirs in river. This would allow either to increase the upstream water level, thus, the head on a powerplant, while maintaining inundation risks comparable to the previous ones due to the increased discharge capacity or to decrease upstream inundation risk if the weir crest level is maintained constant. Furthermore, the installed fish pass in the outlet key would contribute to restore continuity in the river for fish movements.

## 8.2.2 Research Novelty and Contributions

The development of a structure which combines a PKW with a fish pass is pristine and there are no examples of the design of such structures in literature. This study has assessed the discharge efficiency and the fish passage efficacy of this combined structure, by assessing numerically the discharge coefficient, water level and velocity field. This new structure may be seen as an opportunity to easily implement a fish passage while increasing the efficiency, thus, the safety, of the weir structure. Likewise, the combined structure is a great option for locations with limited lateral sections and can be installed to increase and maintain the water level on rivers with the purpose of installing hydropower plants or irrigation while allowing the fish passage and the discharge of a minimum ecological flow.

## 8.3 Future Improvements of the Research

From results reached with this Ph.D. work, following improvements could be considered for the next developments of the research:

- Concerning the type B PKW analysis, the implementation of several type B PKWs in the numerical model, varying one geometric feature at a time would contribute to further assess the variation of the discharge efficiency. This analysis will contribute to determine the hydraulic and the geometric ranges and conditions in which the PKW type B is the most efficient amongst all PKW types and should be preferred instead of a type A PKW.
- In reference to the developed combined PKW – Fish Pass structure, an analysis may be performed about the advantages and disadvantages in terms of economical and building aspects of installing the combined structure instead of both structures independently.
- The main future improvement is to make the PKW – Fish Pass structure suitable for a wider range of fish species while avoiding excessive reduction on the discharge efficiency. This would include the variation of the baffles' geometry located inside the outlet key of the PKW. The main PKW related geometric features that influence the fish pass design are the height,  $P$ , the

outlet key width,  $W_o$ , and the lateral length,  $B_h$ . Likewise, these parameters strongly influence the discharge efficiency of the weir, thus, further research is required to find the most optimal structure in terms of biological range that allows the highest discharge efficiency under the studied conditions.